Investigation of Tropospheric Turbulence Using the Adelaide VHF Radar

K. L. Mu
B. Sc. (Hons.)

A Thesis
Submitted for the Degree of
Master of Science
at
The University of Adelaide
(Department of Physics & Mathematical Physics)

November 6, 1991

Abstract

Turbulence is an important aspect of the whole makeup of atmospheric motions. It is the product of other atmospheric events such as atmospheric gravity waves and wind shear induced Kelvin Helmholtz instability, etc. To understand the morphology of turbulence, it is necessary to calculate certain parameters associated with it, and this involves determining the refractive index structure constant $\overline{C_n{}^2}$ and the average kinetic energy dissipation rate $\bar{\epsilon}$, which is a measure of the severity of turbulence.

Measurements of $\bar{\epsilon}$ can be made in several ways, and these are briefly described in the second chapter of this report. The method to be used for this experiment will be based on a statistical model proposed by VANZANDT *et. al.* (1978) and involves making measurements of the refractive index structure function $\overline{C_n{}^2}$ using radar observations during both clear as well as cloudy air conditions, from which the energy dissipation rate may be derived. This method is heavily dependent on the statistical analysis of wind shears, and the calculated values may be in error by as much as an order of magnitude. The studies include a careful analysis of biases and systematic errors which may be introduced by the radar measurements.

Preface

This thesis contains no material which has been accepted for the award of any other degree or diploma in any University, and to the best of the author's knowledge and belief, it contains no material previously published or written by any other person, except when due reference is made in the text. I consent to this thesis being made available for photocopying and loan by the librarian of the University of Adelaide upon acceptance of the degree.

K. L. Mu

Acknowledgements

Firstly, as this work was made in conjuction with the *Adelaide Meteorological Bureau*, the author would like to thank all the staff at the *'airport'* and *'Kent–Town'* for their helpful assistance and friendliness shown to him during the time he was working there.

Secondly, I am very grateful for the assistance given to me by one of my supervisors, *Dr. W. K. Hocking*, who helped greatly with the final format and contents of the thesis. In addition, I would like to acknowledge the *radio physics* group for their help in the initial part of the project work and also to *Trevor Harris* for the use of his image_cont procedure.

Finally, I would like to thank all the members of the *atmospheric physics* and *theoretical physics* group, especially for the friendships made over the years.

Contents

List of Figures

List of Tables

Chapter 1

Background

1.1 Introduction

From its simple perspective, the concept of turbulence may not be too difficult to fathom — one may describe it simply in terms of such adjectives as disturbed, tumultous, disorderly, chaotic, etc.; however, for atmospheric and fluid dynamicists, the study of turbulent motion can become very complex. This is compounded, in the case of the atmosphere, by its sheer size; for here, we are dealing with an incredibly large laboratory, impossible to control and still very little understood.

The aim of this chapter is to introduce readers to some of the historical works which culminate in the study presented in this thesis. In addition, relevant topics on the subject matter will also be given. Section 1.2 will briefly summarise observations of Clear Air Turbulence (CAT) as detected by atmospheric radars, Section 1.3 will describe vertical structure of the earth's atmosphere, Section 1.4 will deal with the different mechanisms responsible for the types of turbulent structures observed, and the known causes of turbulent motions will be discussed in Section 1.5. In Section 1.6, a review of some of the most recent measurements of $C_n{}^2$ will be given, and some of the more promising applications of the work considered thus far are described in Section 1.7.

1.2 Historical Review

During the early part of the 1960's, a new term called *Dot Angel echoes*[1] was used in the field of radiophysics. These echoes were so named because there was uncertainty about

[1]See Appendix A for a brief discussion on Dot Angel echoes.

the nature and cause of these *mysterious* targets. It is certain, however, that they were not due to either aircraft or precipitation. A review article on *clear air* radar echoes was published by HARDY and KATZ (1969). Their findings on target types, in association with the received radar echoes, suggested the following classes of echoes: type–I targets known as *dot* or *point*, and type–II targets which were called *extended*. Type–I echoes have been shown to be caused by discrete targets such as insects and birds (GLOVER and HARDY, 1966a), while type–II echoes are mainly due to inhomogeneities in the refractive index gradient, or under certain conditions specular reflection from layered structures in the refractive index field. It is the type–II targets which are of most interest to atmospheric scientists for the study of atmospheric turbulence in the clear atmosphere.

Other important discoveries made during this decade included the detection of *stable layers* by LANE and MEADOWS (1963); the detection of identifiable echoes due to the *tropopause* by ATLAS *et. al.* (1966); and observations of turbulence in the form of a layer having the appearance of a braided rope (HICKS and ANGELL, 1968). It is worth noting that all of the above observations were made using *pulsed non–doppler* radars. The more sensitive *pulsed doppler* radars and high resolution FM–CW radars only came into operation around 1970. These were quickly put to good use, with most of the pulsed doppler radars being developed as static sounders capable of obtaining continuous wind profiles throughout the troposphere. Futhermore, observations made with the FM–CW radars were capable of revealing boundary layer wave motions with displacement amplitudes as small as a few metres (OTTERSTEN *et. al.*, 1973).

Most of the early research of the atmosphere were done using centimetre wavelength radars. As a result, most of the experimental work was carried out in the tropospheric region, thus allowing for simultaneous measurements of atmospheric parameters using airborne instrumentations[2].

As the world's technology improved, so too did radar technology, giving rise to more powerful radars operating at different frequencies which were capable of detecting targets at a much greater range than previously possible (WOODMAN and GUILLEN, 1974). In addition, there was a much greater analytical capability, because of faster and more

[2]Such as aircraft or balloon borne instruments.

powerful computers being used in data analysis. As a result of all this, research into the characteristics of the earth's atmosphere was extended into the stratospheric region, below the 30 km height range. Observations made during this period included the detection of turbulent scattering from thin stable layers in the lower stratosphere (CRANE, 1970), and many observations were made mainly to explore the occurence and motion of turbulence in this region, such as wind profile measurements, short–period gravity wave perturbations of the wind profile, and the anisotropy of turbulence in stably stratified regions.

With recent concerns about the transport of Chloro–Fluoro–Carbons (CFC's) and other ozone–destructive chemicals into the atmosphere, there has been a greater interest in the study of tropospheric–stratospheric exchange processes. Radars are invaluable tools in this area of research, because they allow us to observe the flow field of air masses in the region of interest, using radio wave scatterers (possibly generated by turbulence) as a tracer of air motion. In particular, the determination of the refractive index structure constant, the energy dissipation rate, and the relations between the turbulent regions where mixing takes place, are important quantities to evaluate.

1.3 Vertical Structure of the Atmosphere

The atmosphere which envelops this planet of ours, sustaining its myriad of life–forms, is considered to be that region which extends from the ground (or ocean surface) to that part of the highest region which is rotating together with the earth, whose height ranges from 20,000 km to 40,000 km. Of course, existing radars are limited in the range at which they operate, with most available radars operating below the 1000 km height range. In addition the lowest observable height for a radar is limited by other factors, such as the speed required to switch between transmission and reception, ground clutter echoes, etc.

Considering only the lower 1000 km region of the atmosphere, there exist certain characteristics in its vertical structure which makes it possible to 'break it up into sections'; the major sections are characterised by the following distinct features (refer to Figure 1.1):

- Troposphere — a constant decrease in temperature with height as a result of absorption of solar radiation at the earth's surface and re–radiation. A typical lapse rate

would be 6–7 K/km. At around 10–15 km the temperature ceases to decrease with altitude; this region is known as the *tropopause*. The tropopause height generally decreases with latitude.

- Stratosphere — an increase in temperature with height due to the absorption of solar ultraviolet radiation by ozone, which are prevalent at this height range. The increase in temperature with height produces stable stratification of the atmosphere, hence the term *strato*sphere. The upper limit of the stratosphere is where its temperture is a maximum[3], after which it ceases to increase with height; this region of only a few kilometre extent is called the *stratopause*.

- Mesosphere — a decrease in temperture with height as determined by the heat balance of radiative heating of molecular oxygen and infrared radiative cooling of carbon dioxode. Its upper limit is determined by the *mesopause*, where a minimum temperture of 180–190 K is reached.

- Thermosphere[4] — a monotonically increasing temperature with height to the limit of 1000–2000 K. Its main heat source is that from radiative heating of atomic elements.

At the present time, the region of interest for our study is limited to the troposphere. This is because of the low transmitter power used, and the fact that the radar was operating with its polar diagram in the off–vertical mode[5].

1.4 Classifying Clear Air Turbulence

During the first half of the nineteenth century, turbulence was studied by only a few members of the Western scientific community; most notably TAYLOR, REYNOLDS and RICHARDSON. In Eastern Europe, the initial progress on turbulence theory was largely made by two Soviet scientists, KOLMOGOROV and OBUKHOV, who in 1941 established the laws which characterise the basic properties of the microstructure of turbulent flow at very large Reynolds numbers. Two decades later, another Soviet scientist, TATARSKI

[3]This occurs at the stratopause height of $\approx$ 50 km.

[4]Due to a significant concentration of ions above 100 km altitude and of neutrals below this height, this region is also termed the *ionosphere*.

[5]This is explained in Appendix A when we consider the aspect sensitivity of the received echoes.

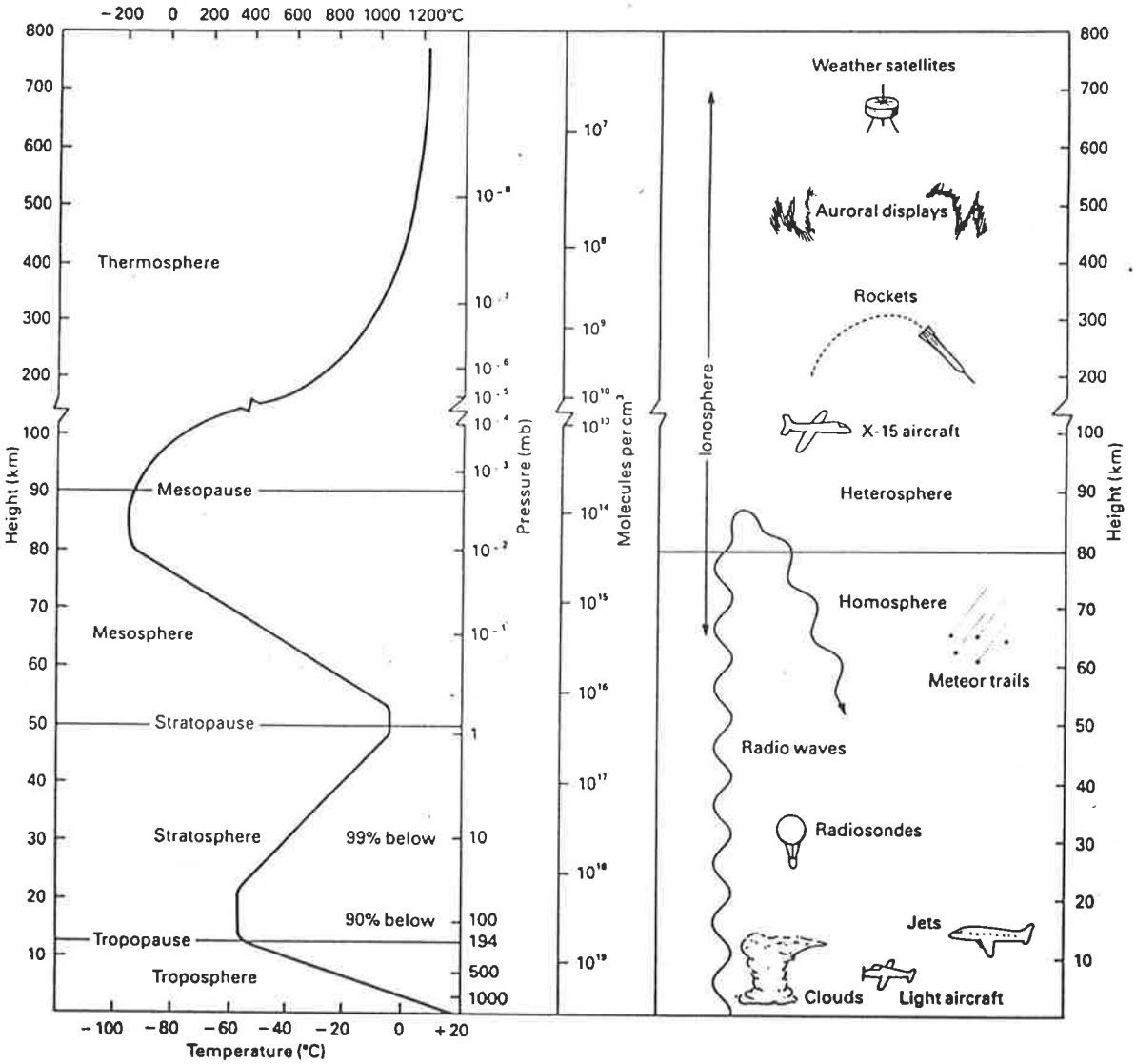

Figure 1.1: The Earth's atmosphere below 800 km altitude is shown here with the different layers (as determined by the temperature profile and composition of the atmosphere) and some additional information which may be of interest to readers. (After Eagleman, 1985.)

(1961, 1971) developed a relationship between the refractive index fluctuations produced by clear air turbulence and the structure and intensity of the turbulence. This was seen as the first step towards parameterising the turbulent scatter from the clear atmosphere. To date, there exist several models proposed to estimate the refractive index structure constant C_n^2 by radar, from which the kinetic energy dissipation rate ϵ may be calculated, enabling us to determine the severity of the turbulence (see, for example, VANZANDT *et. al.*, 1978; GAGE *et. al.*, 1980b; VANZANDT *et. al.*, 1981). Preliminary estimate of the intensity of turbulence have been reported by CRANE (1977), which showed that radar observations together with simultaneous measurements of temperature, humidity and pressure obtained from radiosonde soundings are useful for the estimation of C_n^2.

From our present understanding of the atmosphere, the returned echoes produced by radar probings of the clear air may be classified as being due to one (or more) of the following:

- Turbulent Scatter[6]
  - Scattering from *Isotropic Turbulence*
  - Scattering from *Anisotropic Turbulence*
- Partial Reflection[7]
- Fresnel Scattering
- Thermal Scatter[8]

Thermal scattering is scattering from free electrons and is therefore only important when considering height ranges of greater than about 50 km, that is, above the stratopause. The main mechanism below stratospheric heights, which is presumed to play the major role in the analysis presented in this report, is that of *turbulent scatter.* This type of mechanism is thought to be the primary cause of scattering from clear air observed at radar wavelengths around 10 cm and from off–vertical probings using VHF and HF radars.

[6]The term *Bragg scatter* is sometimes used.
[7]Also called *Fresnel reflection* .
[8]An alternative name for this type of scatter is *Incoherent scatter* .

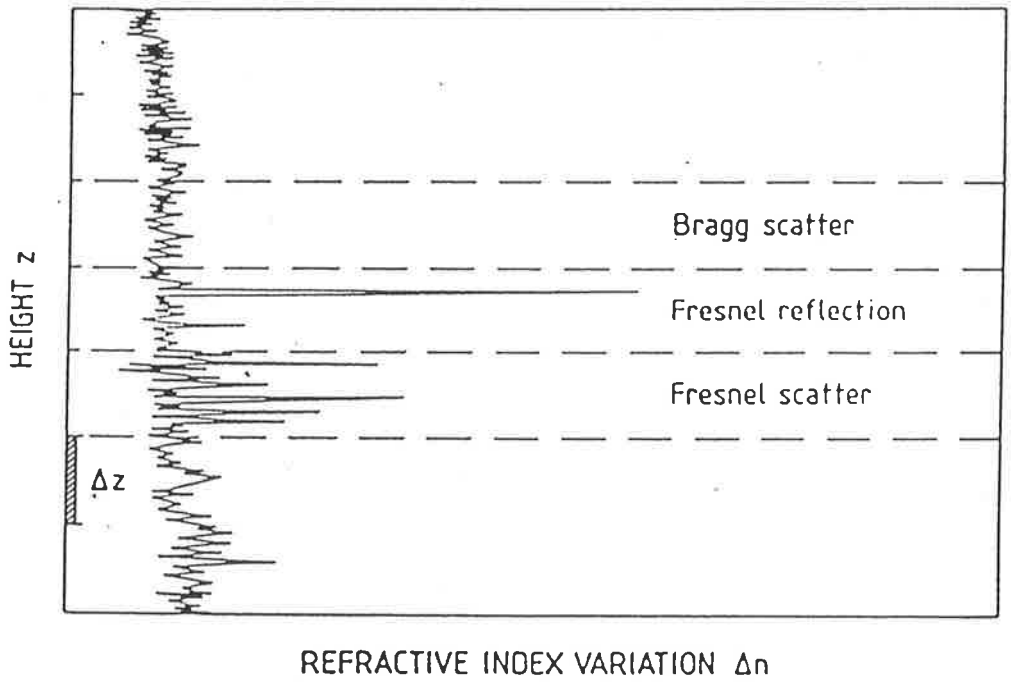

Figure 1.2: For the observed variations in the refractive index of air Δn with height, and depending on the structure of n within the range gate Δz, one would observe either of the three known processes indicated on the diagram. (After Röttger and Larsen, 1989.)

To distinguish between the different forms of processes of scattering and partial reflection, it will be necessary to investigate certain inherent features of the radar echoes which may help us to discriminate one from the other. Such features may include its aspect sensitivity[9], temporal and spatial coherency and spectral shape. A schematic representation of the refractive index variations[10] which may cause the different types of scattering and reflection processes is given in Figure 1.2. It is also to be noted that the types of mechanisms already discussed are very much dependent on the frequency of the radar used, due to the differing characteristics of the spatial variations in the refractive index corresponding to the Bragg scale and Fresnel zones. One such example is that given by BALSLEY and PETERSON (1981): while using the 1290 MHz ($\lambda = 24\ cm$) Chatanika radar (Alaska), they have shown that no specular echo was observed at this particular wavelength.

As a prelude to a discussion on the different types of processes contributing to echoes

[9]See Appendix A.
[10]Within the range gate Δz.

received with atmospheric radars, we will firstly introduce some statistical concepts. To characterise the statistical properties of a randomly varying function $f = f(t)$, both the mean $\bar{f}$ and the *correlation function* Q_f may be used: the correlation function for complex amplitudes is defined as follows

$$Q_f(t_1, t_2) = < [f(t_1) - \overline{f(t_1)}][f^*(t_2) - \overline{f^*(t_2)}] > \quad (1.1)$$

$$= < f'(t_1) f^{*\prime}(t_2) > \quad (1.2)$$

where $f = f' + \bar{f}$ and $f^* = f^{*\prime} + \bar{f}^*$; the asterix represents complex conjugates, t_1 and t_2 are time variables and the angle brackets denotes an ensemble average. From this, we can see that given $t_1 = t_2$ we have the obvious result $Q_f = 1$.

Let us define a *stationary random function* as one having a constant mean and a correlation function which is wholly dependent on the time interval $\tau = t_1 - t_2$. Using the stochastic Fourier–Stieltjes integral to represent a stationary random function $f(t)$, TATARSKI (1961, pp. 4-5) showed that it's *auto*correlation function is given by

$$Q_f(\tau) = \int_{-\infty}^{+\infty} \exp(i\omega\tau) W(\omega) d\omega \quad (1.3)$$

where $W(\omega)$ represents the average spectral density of the fluctuations (in the frequency domain).

The *structure function* $D^2(\vec{r})$ was introduced by KOLMOGOROV (1947) for *spatial* correlations. For a homogeneous case, we have that

$$D^2_\zeta(\vec{r}) =< |\zeta(\vec{x}) - \zeta(\vec{x} + \vec{r})|^2 > \quad (1.4)$$

where $\vec{r}$ is the displacement vector, $\vec{x}$ is the position vector, the *bra* and *ket* represents an ensemble average over space and time, and ζ represents any passive tracer[11], which in our case will be replaced by the refractive index variable n. By expanding out Equation 1.4, we can relate $D^2(\vec{r})$ to the correlation function $Q(\vec{r})$, that is, $D^2(\vec{r}) = 2(Q(0) - Q(\vec{r}))$.

[11] A parcel of air may be characterised by such quantities as temperature, humidity, etc. A quantity is then said to be *conservative* if the value stays constant when the parcel shifts its position, and it is said to be *passive* when it does not affect the dynamical regime of the turbulence.

1.4.1 Turbulent Scatter

From the previous section we have seen that turbulent scatter may be classified as either *isotropic* or *anisotropic*, depending on the scales of the turbulent structure which we are considering; for example, for scales within the *inertial subrange* (see Figure 2.1) it is assumed that the scatterers are isotropic; that is, there is homogeneous mixing of the turbulent medium producing a statistically uniform structure in all directions. If larger scales are considered, such as those within the *buoyancy subrange*, then it is very unlikely that the structure will be uniform in three dimensions[12], and in this case the scatterer is said to be anisotropic. Apart from its aspect sensitivity, there are other notable similarities between isotropic and anisotropic scatter, *viz.* temporal variations and an approximate Gaussian doppler spectrum. The development of the various theories to explain the mechanism for scattering of radio waves from randomly distributed turbulent irregularities will now be considered.

One of the first papers devoted to the problem was by BOOKER and GORDON (1950), who explained the *over–the–horizon tropospheric radio propagation phenomena* as a direct result of turbulent scatter from atmospheric inhomogeneities. The theory starts off with the arbitrary assumption that the refractive index inhomogeneities has a correlation function of the form:

$$Q_n(\rho) = \overline{n'^2} \exp\left(-|\rho/r_0|\right) \tag{1.5}$$

where n' $(= n - \bar{n})$ is the deviation of the refractive index n from its mean value $\bar{n}$ (≈ 1), ρ $(= r_1 - r_2)$ is the correlation distance and r_0 is the outer scale of the inhomogeneities.

The effective scattering cross section into the solid angle $d\sigma$ in the direction of the unit vector $\vec{m}$ is shown by TATARSKI (1961, pp. 68) to be proportional to the "intensity" of the inhomogeneities with sizes satisfying the Bragg condition. Now, if we were to obtain an expression for the effective cross section for scattering σ, using the results of TATARSKI (1961, pp. 71), we would find that the Booker–Gordon theory gives the effective cross section as a function of the single parameter n'^2/r_0, where r_0 is commonly taken to be a constant ($\approx$ 60 metres); as a result, the Booker–Gordon theory, and other papers based

[12] In other words, it is aspect sensitive.

on it, seemed to have overlooked some important factors:

- n'^2 and r_0 characterises large scale inhomogeneities.
- the largest scales are always inhomogeneous and anisotropic with scale size ranging from some tens of centimetres to some tens of metres.
- the spectrum of the refractive index gradient is a function of a range of scales, not necessarily related to 60 metres.

Different forms of the correlation function for the refractive index were used to improve on the Booker–Gordon theory, but there is still no agreement on which (if any!) can be considered to serve the purpose at all times. Consequently, it is now widely accepted that there is no single spectral function describing spatial refractive–index variations which is universally applicable!

It wasn't until 1961 that some new lead to explain the scattering of electromagnetic waves from turbulent flow was made. Let us now consider the model of TATARSKI (1961) which attributes the refractive index fluctuations to turbulent mixing. In this model both the potential temperature and specific humidity are assumed to be conservative and passive. To describe the statistical properties of the turbulence, TATARSKI (1961) made use of the structure function defined in the previous section (Equation 1.4). Then, for isotropic inertial range turbulence, we have that $r = |\vec{r}|$, from which the refractive index structure function can be shown to be given by the following relationship (*e.g.,* TATARSKI, 1961, pp. 46)

$$D_n(r) = {C_n}^2 r^{2/3} \tag{1.6}$$

where ${C_n}^2$ is the refractive index structure constant, which depends on the intensity of turbulent motions, and $l_0 \ll r \ll L_0$; that is, r is bounded by the inner scale l_0 and outer scale L_0 of the turbulence. In conditions of hydrostatic stability, the quantity ${C_n}^2$ can be calculated from the following equation, which expresses ${C_n}^2$ in terms of quantities characterising the average profiles of the wind, temperature and humidity, i.e.,

$${C_n}^2 = a^2 L_0^{4/3} M^2 \tag{1.7}$$

where M is the gradient of the generalised potential index. For radar wavelengths M is given by OTTERSTEN (1969), as

$$M = -77.6 \times 10^{-6} \frac{P}{T} \left(\frac{\partial ln\theta}{\partial z} \right) \left[1 + \frac{15600q}{T} \left(1 - \frac{1}{2} \frac{\partial lnq/\partial z}{\partial ln\theta/\partial z} \right) \right] \quad (1.8)$$

where P (mb) is the atmospheric pressure, T (K) is the absolute temperature, $\theta \equiv T(P_0/P)^{2/7}$ is the potential temperature, P_0 is a reference pressure — normally taken to be $1000\,mb$, z (km) is the range height and q (g/kg) is the specific humidity. ${C_n}^2$ therefore characterises the intensity of the small scale refractive index inhomogeneities. The subject of the refractive index structure constant will be further dealt with later in the next chapter. Equation 1.7 has since been improved (see, for example, GAGE and BALSLEY, 1978).

1.4.2 Partial Reflection

It was not until the late 1950's, when doubts were placed on the concept of turbulent scattering as the only main mechanism responsible for the observed *troposcatter radio phenomena* (FRIEND, 1940), that *partial reflection* from layered structures in the refractive index field was proposed as an alternative mechanism which can contribute significantly to clear air refractivity in some circumstances (SAXTON *et. al.,* 1964; GAGE and GREEN, 1978; RÖTTGER, 1980; TSUDA *et. al.,* 1986). The work of SAXTON *et. al.* (1964) clearly showed the layer–type radar echoes (using the SHF band) to be correlated with steep gradients in the refractive index. In addition, their investigation showed the observed radar echoes as having an association with identifiable features in the refractive–index–height record, but that the reverse is not always true. This they interpreted as being due to the relative significance of scattering and partial reflection in the troposphere. DU CASTEL *et. al.* (1962) and DU CASTEL (1966) have developed a partial reflection theory for rough surfaces and have concluded that the tropospheric radio propagation phenomena can be explained by the combined influence of *specular reflections* from smooth layers, *diffuse reflection* from roughened layers, and *scattering* from turbulence.

At this point it is necessary to distinguish between Partial reflection and Fresnel

scatter. Both mechanisms involve echoing from an ordered collection of refractivity fluctuations, with spatial coherency transverse to the radar beam, and with scale sizes from a few wavelengths to greater than a Fresnel zone[13]. The existence of these structures are generally found during stable conditions, where regions of the atmosphere are horizontally stratified. The distinguishing feature is found parallel to the radar beam. In this sense the structure can be seen to vary from strictly ordered (in the limit, a single thin layer) to randomly distributed (for multiple layers with vertical dimensions large compared to the transmitted pulse width). From this simplified discussion, Fresnel reflection refers to echoing processes due to a parallel ordered structure, and the echoes associated with parallel random structure are considered as Fresnel scattering.

RÖTTGER and LIU (1978b) made some calculations on the relative importance of the power from partially reflected signals to that of turbulence scattered signals. Their calculations indicated that under certain conditions partial reflections from regularly stratified layers may contribute significantly to the received echo power of a VHF radar at *vertical incidence*. However, they were unable to determine which of the two mechanisms was the major contributor to the received power. It was suggested by GAGE and BALSLEY (1980a) that the mechanisms responsible for *Fresnel scattering* and *anisotropic turbulence* may be indistinguishable in their nearest limits. This is inconclusive, and further research is needed in order to resolve this ambiguity. Recent experiments tended to favor the Fresnel scattering mechanisms in relation to partial reflections to explain the specular echoes observed on VHF radars (GAGE and GREEN, 1978; RÖTTGER and VINCENT, 1978a).

A common occurence with observations made of the atmosphere with a radar beam which is vertically incident is the relatively strong signals received in this mode of operation (call this S_v). This is often interpreted to be caused by partial reflection from a sharp gradient of refractive index. A single–layer partial reflection model was used by SAXTON *et. al.* (1964), GAGE and GREEN (1978) and RÖTTGER and LIU (1978). The form of the reflection coefficient derived was expressed as

$$|\rho|^2 = \frac{(\delta n)^2 \lambda^2}{(8\pi)^2 L^2} \tag{1.9}$$

[13]A Fresnel zone equals $\sqrt{\lambda z}$, where λ is the operating frequency and z is the height of scatter.

where δn is the the variation of the radio index of refraction n across a layer in excess of the normal lapse and L is the thickness of the layer. However, this model was not without its problems. In the first instance, GREEN and GAGE (1980) have shown that good correlation exists between S_v and the radio refractive index for a dry atmosphere M_d, which is given by TATARSKI (1971) as

$$M_d = -77.6 \times 10^{-6} \frac{P}{T} \frac{\partial ln\theta}{\partial z} \tag{1.10}$$

where P is the ambient air pressure in millibars, T is the absolute temperature in degrees Kelvin, θ is the potential temperture in degrees Kelvin, and the altitude z is in metres. Thus M_d can be related to the hydrostatic atmospheric stability ${\omega_B}^2$, where ω_B is the Brunt Väisälä frequency[14].

In addition, the authors have shown a dependence of S_v on the range resolution Δr. Neither of these observations can be interpreted on the basis of partial reflection theory and the use of Equation 1.9.

1.4.3 Fresnel Scatter

The term "Fresnel Scatter" in connection with the concept of transverse coherence in the fine structure of the radio refractive index within a region of finite vertical extent was used to take into account the considerations discussed above. Such a model was shown by GAGE *et. al.* (1981) to be more consistent with observations made using the Sunset VHF radar in Colorado. To obtain an expression relating the magnitude of Fresnel scattering to the radar range resolution, we will follow closely the original work of GAGE *et. al.* (1981). Let us begin with the assumption that the refractive index n varies only with height z, *i.e.*, $n = n(z)$. Then, the power reflection coefficient ρ for a single layer is given by (see, for example, WAIT, 1962)

$$\begin{aligned} \mid \rho \mid^2 &= \rho\rho^* \\ &= \frac{1}{4}\left(\int_{-\frac{t}{2}}^{+\frac{t}{2}} \frac{dn}{dz} \exp(-2kiz)dz\right)^2 \end{aligned} \tag{1.11}$$

where t is the layer thickness, $i = \sqrt{-1}$ and $k = 2\pi/\lambda$. It should be noted here that the above formulation is only an approximation. A more realistic approach would involve a

[14] ${\omega_B}^2 = g\partial ln\theta/\partial z$.

convolution between ρ and ρ^* (HOCKING and RÖTTGER, 1983a).

As first considered by ALLEN and WEINER (1963), who obtained $\mid \rho \mid^2$ from consideration only of the Bragg scatter scale ($\lambda/2$) from acoustic pulses in a Radio–Acoustic Sounding System (RASS), GAGE *et. al.* (1981) used a hypothetical layer of finite thickness L to represent the case for Fresnel scatter, which was arbitrarily expressed as

$$n = [\delta n]_{\lambda/2} \sin(2kz) \tag{1.12}$$

where $[\delta n]_{\lambda/2}$ is the amplitude of the Fourier component of the vertical structure with vertical wavelength equal to $\lambda/2$. From Equation 1.11 we note the fact that when $L < \Delta r$, the limits of integration are replaced with $L/2$, and it follows that there is no dependence on Δr. However, for the case when $L > \Delta r$, we have that

$$\begin{aligned} \mid \rho \mid^2 &= \frac{1}{4}\left(\int_{-\frac{\Delta r}{2}}^{+\frac{\Delta r}{2}} \frac{d}{dz}\left[[\delta n]_{\lambda/2}\sin(2kz)\right]\exp(-2kiz)dz\right)^2 \\ &= ([\delta n]_{\lambda/2})^2\frac{N^2\pi^2}{4} \\ &= ([\delta n]_{\lambda/2})^2(\Delta r/\lambda)^2\pi^2 \end{aligned} \tag{1.13}$$

where N is the number of half wavelengths contained within the range Δr. This result clearly shows a dependence on $(\Delta r)^2$.

In a paper by HOCKING and RÖTTGER (1983a), the authors questioned the $(\Delta r)^2$ dependence for the voltage reflection coefficient as given by Equation 1.13. Their argument against this can be summarised as follows: the analysis of the received signal strengths due to backscatter from the Fourier scales can be considered as a random–walk type problem. In this case, it can be shown that the mean square received power is proportional to the pulse width, and not to the square of the pulse width as derived by GAGE *et. al.* (1981). In fact, the square of the pulse width dependence is a special case where the reflection coefficient profile is purely a sinusoidal variation of $\lambda/2$, which is the case considered by GAGE *et. al.* (1981). In practice, the existence of such a profile is considered extremely remote: a more realistic profile would be random in both its vertical spatial variations and its amplitudes. A revised model with an assumed random distribution of the layered structure was given by GAGE *et. al.* (1985). This paper was a culmination of contributions

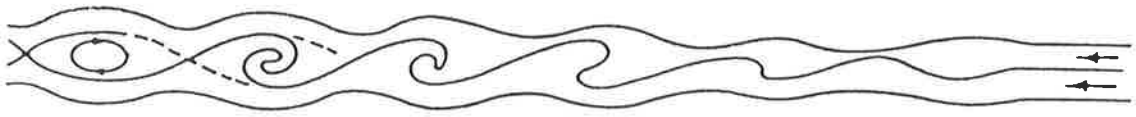

Figure 1.3: The production of billows, through the interaction of wind shear in an initially stably stratified atmosphere.

to the original model for Fresnel scatter from such authors as HOCKING and RÖTTGER (1983a), FARLEY (1983), LIU (1983) and DOVIAK and ZRNIC (1984).

1.5 Sources of Atmospheric Turbulence

Let us now consider the possible generation mechanisms wich can lead to clear air turbulence. Common sources of energy for turbulent velocity fluctuations are shear in the mean wind and breaking/overturning of short period gravity waves. Other sources (with less frequent occurrence) are jet streams and convection during the passage of a cold front or thunderstorm. Turbulent flows are therefore generally shear flows. An indicator for shear–induced turbulent flow is the gradient Richardson number Ri. For an initially stably stratified atmosphere, the existence of a wind shear would induce *billows*, as depicted in Figure 1.3, resulting in turbulence from the overturning of the wave. Wind shears, in the vicinity of a stable gravity wave, produces Kelvin–Helmholtz Instability (KHI), which also leads to clear–air turbulence through wave–breaking.

Sources of gravity waves found in the lower atmosphere are commonly attributed to mountain lee waves[15] (see, for example, BROWNING, 1978), wind shear and convection[16]. The detection of gravity waves in the lowest kilometre of the earth's atmosphere has been widely documented. GOSSARD *et. al.* (1970) have made several observations in

[15]Such as the flow of wind over mountanous areas.

[16]In the troposphere, fronts and jet streams are common sources.

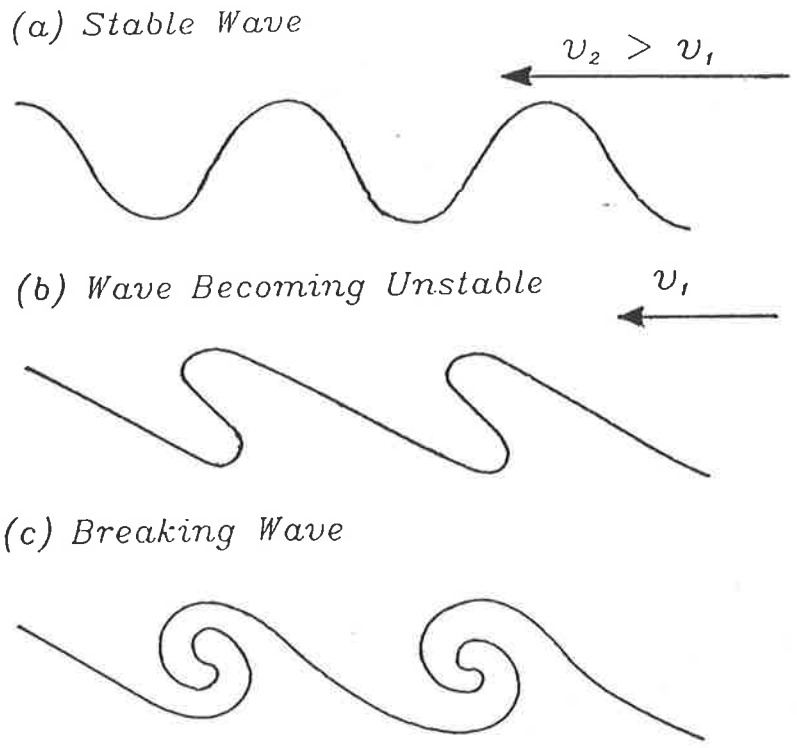

Figure 1.4: Sketch of a vertically propagating gravitational wave embedded within a strong shearing layer: (a) stable wave, (b) wave becoming unstable, and (c) wave breaking and forming vortices.

which they detected several periodically spaced layers, which they attribute to untrapped internal gravity waves. In another paper, GOSSARD and RICHTER (1970), showed an example of a trapped internal gravity wave.

Upward propagating atmospheric gravity waves may either be absorbed or reflected by the background flow. There is total reflection of the wave when its intrinsic frequency equals that of the background flow; the wave is absorbed when it encounters a 'critical layer', that is, where the component of mean flow velocity in the direction of gravity wave propagation equals the phase speed of the propagating wave. At such a level, the wave is said to 'break', resulting in the production of turbulence. Figure 1.4 shows the process leading to the breakdown of a gravity wave in the atmosphere. An interesting study by LILLY *et. al.* (1974) showed a strong preference for greater–than–moderate stratospheric turbulence (about 90%) to occur over mountainous terrain, being induced by high–amplitude *breaking gravity waves*; this is consistent with the work of BRETHERTON (1969).

One other interesting structure often observed in the clear atmosphere by investiga-

tors using radars in the centimetre wavelength range is the so called Kelvin–Helmholtz instability (HARDY and KATZ, 1969; KENNETH and KATZ, 1969; HICKS and ANGELL, 1968). The structure can be described as having the appearance of a 'braided rope', and are seen to persist for at least several minutes. Other important characteristics include a preference for these structures to be aligned in the direction of the wind shear, and to occur in regions of relatively stable lapse rate (or inversions). From these observations, it was concluded that the structure was the result of a breakdown of gravity waves.

1.6 A Review of C_n^2 Measurements

NASTROM *et. al.* (1986) studied the variability of turbulence at Poker Flat and Platteville over a period of one year. The turbulence parameter used is the refractive index structure constant C_n^2, which is a measure of the refractivity turbulence; they used the method discussed by VANZANDT *et. al.* (1978) to obtain values of C_n^2 from radar observations. For heights of 4–20 km, they found that:

1. C_n^2 has a log–normal distribution[17] for all seasons at all heights.

2. Using much shorter time scales (4 minutes), the autocorrelation function $r(\tau)$ of log C_n^2 was shown to be of the form $r(\tau) = ae^{\nu\tau}$, where a represents a random process and ν is the rate of decay of the autoregressive (red noise) process; both a and ν being negative quantities.

3. The power spectrum of log C_n^2 follows a power law relation with frequency, with spectral slopes near $-5/3$ for periods greater that about 2 hours and -1 at periods less than 2 hours.

4. Winter exhibits the largest monthly mean values of log C_n^2, due largely to the increased jet stream and baroclinic storm activity; a secondary summer peak was also observed, this being due to convective activity.

5. There was good correlation between the 3–hour values of C_n^2 with wind speed; however, monthly correlations are seen to be more closely correlated with monthly

[17] That is to say, log C_n^2 being Gaussian.

means of gravity wave activity.

A rather interesting long–term analysis of C_n^2 measurements is one by ANDREAS (1989), this time over the frozen Beaufort Sea using four electromagnetic wavelengths (0.55 μm, 10.6 μm, 890 GHz and the radio regions) to measure the turbulent surface sensible and latent heat fluxes and hence to calculate C_n^2. He showed that a beta distribution fits the frequency distribution better than a log–normal distribution, which tends to underestimate the location of the peak. Concerning seasonal trends, his results showed a primary narrow peak during winter and a broad summer distribution.

In another paper, EATON *et. al.* (1988) did some extensive comparitive work between three different types of C_n^2 measurement techniques. They found that when the radar was operating at very large zenith angle, the results showed good agreement with both the stellar scintillometer and the thermosonde measurements. Regarding the radar measurements, they first calibrated the SOUSY radar and then converted the received signal power to C_n^2 values. Different zenith angle measurements were also taken, to see the effects of zenith angle dependence on specular reflections. Finally, they applied the corrections due to humidity effects. A typical profile is given in Figure 1.5.

Simultaneous measurements of atmospheric turbulence using a SCIDAR and a radar was made by VERNIN *et. al.* (1990) for an approximate period of two months. Their comparisons showed that the radar profiles and SCIDAR profiles agree fairly well above 9 km, below this height it was thought that the optical refractive index (i.e. without humidity effects) was not accurately measured due to the siting of the radiosonde measurements, being located some 150 km from the radar site. Figure 1.6 gives some typical profiles of radar/SCIDAR C_n^2 measurements. These measurements were taken near Toulon, France, and the VHF radar was operating obliquely at 13° from zenith.

CHADWICK and MORAN (1980) made some long–term measurements of C_n^2 in the boundary layer (at 805 m altitude) and showed that they have a log–normal distribution. They also showed that the distribution of C_n^2 has both a diurnal and an annual cycle. The diurnal cycle exhibits maximum values at midnight and in the early afternoon.

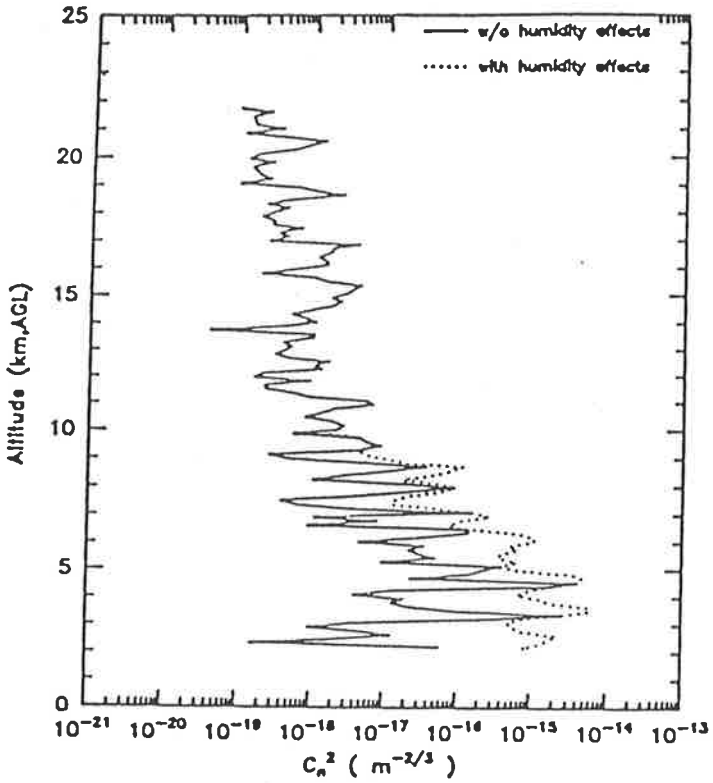

Figure 1.5: Profile of $C_n{}^2$ measured with the SOUSY radar at a zenith angle of 8°. The dashed line is the profile including humidity effects. (After Eaton *et. al.*, 1988.)

1.7 Applications

Promising applications for radar observations of the troposphere under clear air conditions include the following:

1. Measurement of vertical wind profiles,

2. Detection of hazardous low–level wind shears (severe up and down draughts), and

3. Early identification of preferred regions for outbreaks of severe local storms.

With respect to point number three, it is to be noted that low–level convergence which precedes the development of such storms has been detected using a single radar by the direct observation of the increase in the height of the convective boundary layer (JAMES, 1980). In this thesis, we will demonstate another application of these radars, namely, measurement of turbulence.

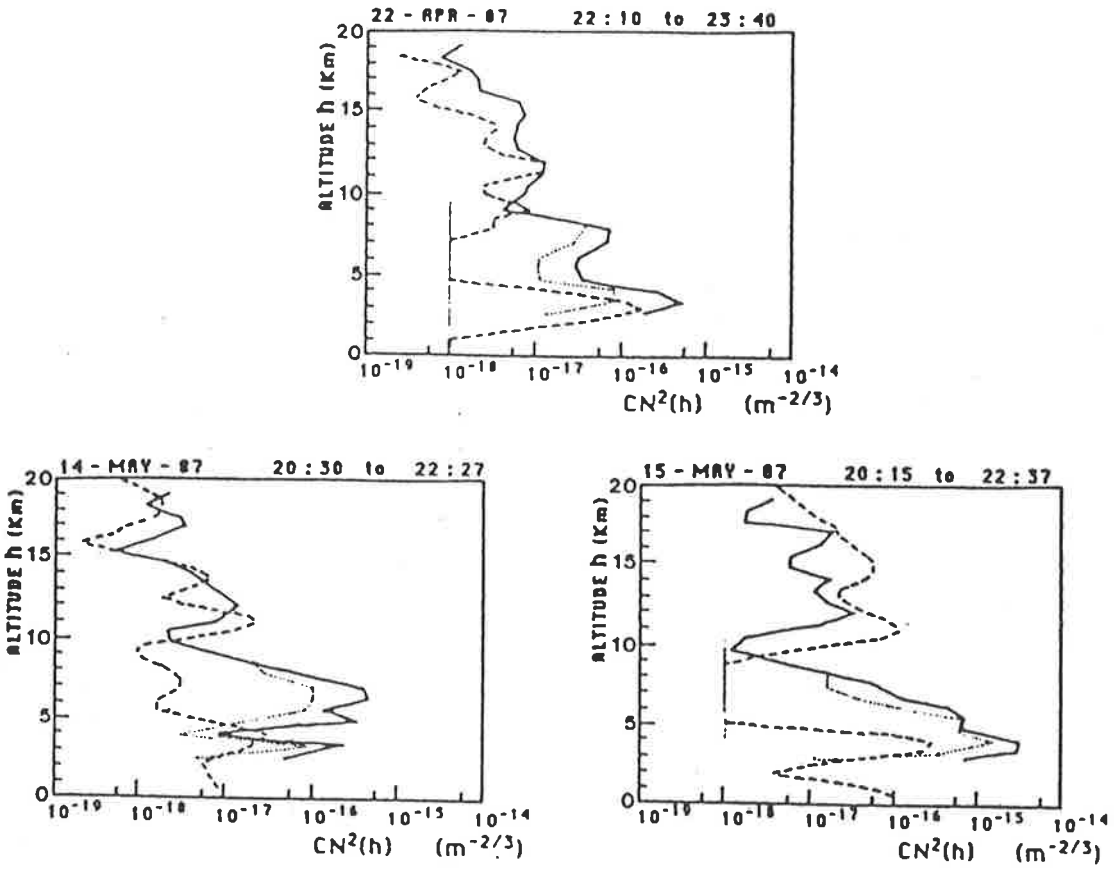

Figure 1.6: Radar (solid lines)/SCIDAR (dashed lines) measured Profiles of $C_n{}^2$: the dotted lines represent the optical $C_n{}^2$. The radar measurements were made at a zenith angle of 13°. (After Vernin *et. al.*, 1990.)

Chapter 2

Theory

2.1 Introduction

There are many helpful books and articles dealing with the subject of turbulence in a much greater scope than what will be presented here (see, for example, BATCHELOR, 1953; HINZE, 1959; HINZE, 1975; LUMLEY and PANOFSKY, 1964; TENNEKES and LUMLEY, 1973). However, it is the aim of this chapter to introduce the reader to the theory of turbulence, with particular emphasis on the work by TATARSKI (1961) and OTTERSTEN (1969a); in addition, a derivation from first principles of the radio refractive index gradient of air will be presented.

As a break–down of the discussion, Section 2.2 will introduce the concept of a turbulence spectrum, and an attempt will be made in Section 2.3 to present a step by step process (from TATARSKI, 1961) leading to the derivation of the refractive index structure constant $C_n{}^2$ and the relationship between it and the energy dissipation rate ϵ. Finally, Section 2.4 will give a concise derivation of the gradient of the radio index of refraction M.

2.2 The Turbulence Spectrum

RICHARDSON (1931) and KOLMOGOROV (1947) suggested that, in fully developed turbulence, the kinetic energy of large–scale anisotropic eddies cascade continually downward to smaller and smaller scale eddies, the motions of which are statistically isotropic. For motions with scale L and a characteristic velocity v, the Reynolds number Re is given by vL/ν_0, where ν_0 is the kinematic viscosity of air. When the Reynolds number becomes

small enough, the cascading process stops and the kinetic energy is dissipated into heat by viscosity. Several scale sizes then characterise the turbulence:

1. The scale of the largest *anisotropic* eddies.

2. The scale where turbulence becomes *isotropic.*

3. The scale where turbulence is strongly damped by molecular *viscosity.*

The regions containing the different scale sizes are called the *buoyancy subrange*, the *inertial subrange*, and the *viscous subrange*, respectively (see Figure 2.1). Theoretical study has concentrated mainly on scales which are somewhere within the inertial subrange; in this family of scales, the turbulence is assumed to be isotropic, that is, the statistical properties of turbulent motions are independent of direction. The limiting microscale of the inertial subrange is of the order of a few millimetres in the planetary boundary layer, increasing to a few centimetres in the upper troposphere. The outer scale, on the other hand, may be as large as several hundred metres in neutral or convective conditions or less than 1 metre within thin statically stable layers (METCALF and ATLAS, 1973). For VHF radars, the spatial scale $L = \lambda/2$ which determines the backscattering from isotropic turbulence will generally fall within the *inertial subrange* up to lower mesospheric heights, particularly if the radar returns originate from regions of violent mixing and intense turbulence (*e.g.,* HOCKING, 1985).

The properties of turbulence in the inertial subrange cannot be determined by the viscosity, because its influence is appreciable only at the finest scales of motion. The characteristic dimension and the velocity of the largest–scale motion likewise cannot affect the properties of turbulence in the inertial subrange. This led KOLMOGOROV to hypothesise a continuous flux of energy from the largest eddies to the smallest, as has already been discussed. In the inertial subrange, energy is tranferred from eddy to eddy without loss, and therefore, the rate of energy transfer from one scale to a smaller one must equal ϵ, the energy dissipation rate. This will become the subject of our next discussion.

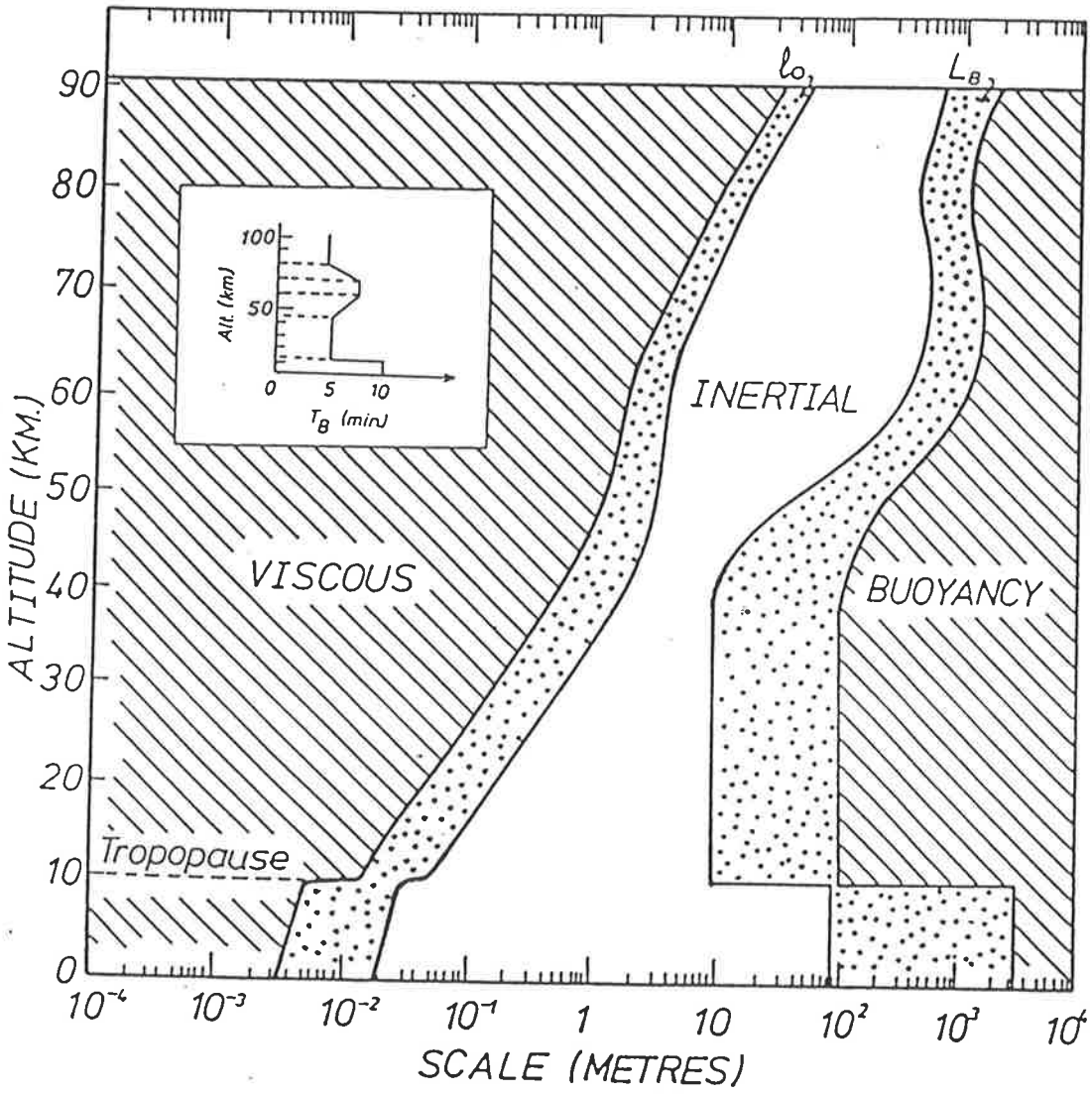

Figure 2.1: Schematic representation of the spectrum of turbulence. (After Hocking, 1985.)

2.3 Turbulence Parameters

The structure constant C_n^2 may serve as a measure of the variability of the refractive index field. Consequently, it may also serve as a measure of the intensity of turbulence, because the more violent the turbulent mixing, the stronger the inhomogeneities in the refractive index field; in addition, it is also known that the humidity contributes to a larger C_n^2. Thus, we have that a strong turbulence and sharp mean gradients and large humidity contribute to high C_n^2 values. However, as pointed out by OTTERSTEN (1969a), such use of C_n^2 values to infer the intensity of clear air turbulence will only be valid when there exists a strong correlation between the vertical gradient of the potential refractive index M and the mean vertical wind shear du/dz, in which case C_n^2 is roughly proportional to $\epsilon^{2/3}$. In the lower troposphere M depends very much on the humidity gradient, which varies considerably, hence it would not be accurate to interpret C_n^2 to be a measure of turbulent intensity.

In the following sections we will present the theory of atmospheric turbulence, in particular as it relates to the refractive index structure constant C_n^2, the kinetic energy dissipation rate ϵ and the gradient of the potential refractive index M.

2.3.1 C_n^2 — The Refractive Index Structure Constant

The treatment of TATARSKI (1961) on the derivation of the refractive index structure constant for isotropic homogeneous turbulence is given here in its abridged version. Starting from the equation for molecular diffusion, i.e.,

$$\frac{Dn}{Dt} + \nabla \cdot (-K_D \nabla n) = 0 \tag{2.1}$$

where $n(= n' + \bar{n})$ is the index of refraction, n' and $\bar{n}$ are its fluctuating and mean components, respectively; K_D is the coefficient of molecular diffusion and Dn/Dt is the rate of change of n "following" the motion, which is given by

$$\frac{Dn}{Dt} = \frac{\partial n}{\partial t} + \nabla \cdot \vec{v}n \tag{2.2}$$

where $\vec{v}$ is the vector of the velocity field.

For an incompressible fluid, we have that

$$\nabla \cdot \vec{v} = 0 \tag{2.3}$$

Assuming that the 'volume integral' of the mean–square value for n' can be taken as a valid measure of the inhomogeneity in the volume V, that is

$$\Theta = \frac{1}{2}\int_V \overline{n'^2} dV \tag{2.4}$$

then, by defining $\Xi(n) = Dn/Dt + \nabla \cdot (-K_D \nabla n)$, and taking the difference of $\Xi(n)$ with $\overline{\Xi(n)}$, and after simplifying, averaging and further simplification, we integrate over the volume V to give us the result[1]

$$\begin{aligned} 0 &= \int_V < \Xi(n) - \overline{\Xi(n)} > dV \\ \Longrightarrow \frac{\partial \Theta}{\partial t} &= \int_V \left[K(\nabla \overline{n})^2 - K_D \overline{(\nabla n')^2} \right] dV \end{aligned} \tag{2.5}$$

where the *bra* and *ket* represents an ensemble average. In deriving Equation 2.5, Tatarski assumed that $-K(\nabla \overline{n}) = \overline{\vec{v}' n}$, where the quantity K is called the coefficient of turbulent diffusion and normally $K \gg K_D$.

Now consider the case for stationarity, where $D\Theta/Dt = 0$, Tatarski came up with the equality between two expressions; one relates to the appearance of the amount of inhomogeneity per unit time, and the other relates to the disappearance of the amount of inhomogeneity per unit time due to molecular diffusion. This is normally expressed by $\overline{N}$, where

$$\overline{N} = K_D \overline{(\nabla n')^2} = K(\nabla \overline{n})^2 \tag{2.6}$$

and this is analogous to the energy dissipation rate ϵ for the special case that n is replaced by $\vec{v}$.

In the case where all inhomogeneities except the smallest is considered (i.e., for $l v_l \gg K_D$), then the amount of inhomogeneity n'_l with characteristic scales l and velocities v_l appearing per unit time is equal to

$$\frac{v_l n'^2_l}{l} \sim \overline{N} \tag{2.7}$$

[1]Tatarski neglected the surface integrals (from the equivalence of the integral of the divergence to a surface integral), because they were small relative to the volume integrals.

Furthermore, using the relation $v_l \sim (\epsilon l)^{1/3}$, we obtain

$$n_l' \sim \frac{\overline{N} l^{2/3}}{\epsilon^{1/3}} \tag{2.8}$$

which has a 'two–thirds' dependence on sizes with characteristic scales l.

Let us consider inhomogeneities for $|\vec{r_1} - \vec{r_2}| \ll L_0$, then the quantity $n(\vec{r_1}) - n(\vec{r_2})$ can be considered statistically isotropic. Thus, $n(\vec{r})$ is a locally isotropic random field. For the range of values $l_0 \ll |\vec{r_1} - \vec{r_2}| \ll L_0$, the structure function

$$D_n(|\vec{r_1} - \vec{r_2}|) = \overline{[n(\vec{r_1}) - n(\vec{r_2})]^2} \tag{2.9}$$

depends solely on the variables $r = |\vec{r_1} - \vec{r_2}|$, $\overline{N}$ and ϵ. Dimensional considerations by OBUKHOV (1949) leads to the commonly termed "two–thirds law", which is given by

$$D_n(r) = \frac{a^2 \overline{N}}{\epsilon^{1/3}} r^{2/3} \tag{2.10}$$

where $r = |\vec{r}|$ and a is a numerical constant. Using the stochastic integral for a locally isotropic random field, we have that

$$D_n(r) = 8\pi \int_0^\infty \left(1 - \frac{\sin(kr)}{kr}\right) \Phi_n(k) k^2 dk \tag{2.11}$$

where $\Phi_n(k)$ is the spectral density in the three–dimensional space of wave numbers k_1, k_2, k_3 of the distribution of the amount of inhomogeneity in a unit volume. From this, we obtain the three–dimensional power density spectrum, *viz.*

$$\Phi_n(k) = 0.033 {C_n}^2 k^{-11/3} \tag{2.12}$$

where

$${C_n}^2 = a^2 \overline{N} / \epsilon^{1/3} \tag{2.13}$$

This important equation will be of particular use later on, where we use it to arrive at a more useful relationship between the refractive index structure constant and the energy dissipation rate.

TATARSKI (1961) also showed that the radar backscatter reflection coefficient[2] η is given by

$$\eta = \frac{\pi^2}{2} k^4 \Phi_n(\vec{k}) \tag{2.14}$$

[2]Compare with the equation derived by Booker (1950).

where $|\vec{k}| = 4\pi/\lambda$. Substituting Equation 2.12 into 2.14, we obtain the well-known expression for reflectivity

$$\eta = 0.38 {C_n}^2 \lambda^{-1/3} \tag{2.15}$$

HOCKING and VINCENT (1982) showed how η could be related to an "effective reflection coefficient" ζ (often a convenient way to parameterize the returned signal) through the relation

$$\zeta^2 = \left(\frac{\theta_{1/2}^2 L}{\ln 2} \right) \eta \tag{2.16}$$

where L is the radar effective pulse-length and $\theta_{1/2}$ is the half-power half-width of the radar polar diagram.

2.3.2 ϵ — The Energy Dissipation Rate

There are several ways in which to estimate the intensity of clear air turbulence. A brief discussion of the various methods will be presented here. For turbulence with scales smaller than the radar resolution volume, an estimate of the turbulence can be made by measuring the half-power half-width of the *broadened* doppler velocity spectra (see, for example, ATLAS, 1964; FRISCH and CLIFFORD, 1974; HOCKING, 1983c; DOVIAK and ZRNIC, 1984b). This method is not as simple as it seems, because other factors contribute to the broadening of the spectra, *e.g.,* shear broadening, beamwidth broadening, contribution of instrumental and signal processing broadening and an allowance for the temporal variation of the mean wind speed within the pulse volume, all of which needs to be taken into account. Thus in order to obtain the spectral variance σ_{turb}^2 due to turbulence alone, these contributions must either be measured or estimated. Having obtained σ_{turb}^2 the next step would be to convert this quantity to a mean square fluctuating velocity $\overline{v'^2}$ by the relation (HOCKING, 1985)

$$\overline{v'^2} = \left(\frac{\lambda}{2} \right)^2 \frac{\sigma_{turb}^2}{2 \ln 2} \tag{2.17}$$

Assuming the above conditions are satisfied, HOCKING (1983c) gave the following relationship between $\overline{v'^2}$ and the energy dissipation rate ϵ:

$$\epsilon \approx c \, \overline{v'^2} \, \omega_B \tag{2.18}$$

where c is a numerical constant of about 0.4 and ω_B is the Brunt Väisälä frequency.

The second technique employs the spectral analysis of a sequence of wind observations, resulting in a $-5/3$ spectral relationship, which is then applied to small scale turbulence (see, for example, LILLY *et. al.*, 1974; KROPFLI, 1971). Such a technique is also being used with acoustic radars. However, there is still some controversy in applying this technique to larger scale atmospheric motions. In addition, there is the disadvantage that very high time resolution data is required in order to obtain good spatial resolution.

Measurements of the energy dissipation rate can also be made from measurements of the refractive index structure constant. A discussion on this third technique will be based chiefly on the work of TATARSKI (1961), with additional reference being made to notes given by HOCKING (Lecture notes, 1990), particularly on the derivation of the relationship between ϵ and the turbulent diffusion coefficient K, which we will now consider.

The outer scale of turbulence L_0 is commonly defined as the height interval over which the mean quantity (such as horizontal velocity u, density ρ, etc.) changes by as much as the degree of fluctuation (TATARSKI, 1971). From this definition, we have that

$$\left(\overline{s'^2}\right)^{1/2} \approx \frac{\partial \overline{s}}{\partial z} L_0 \tag{2.19}$$

where $s\ (= \overline{s} + s')$ is a measure of some atmospheric quantity with mean $\overline{s}$ and fluctuation s'. Let us consider a general case where $s \equiv u(z)$, that is, the horizontal velocity, then

$$\overline{u'^2} \simeq L_0^2 \left(\frac{d\overline{u}}{dz}\right)^2 \tag{2.20}$$

If the velocity fluctuation u' occurs over a distance l, where $l_0 < l < L_0$, it will have a characteristic lifetime given by $\tau \sim l/u'$ and an energy dissipation rate per unit mass of

$$\epsilon \sim \frac{\overline{u'^2}}{\tau} \tag{2.21}$$

Equation 2.21 also applies to the outer scales L_0. Substituting Equation 2.21 into Equation 2.20 and noting that $L_0 \sim u'\tau$, we arrive at an expression relating ϵ to the turbulent diffusion coefficient K, that is,

$$\epsilon \sim K \left(\frac{d\overline{u}}{dz}\right)^2 \tag{2.22}$$

where K is "defined" to be equal to $L_0 u'$ and $\overline{u}$ is assumed to vary chiefly with the height z. It is interesting to note the similarities between the form of Equation 2.22 and Equation 2.6.

From the relation derived earlier for the refractive index structure constant (refer to Equation 2.13), we can write it in the following form after substituting for ϵ from 2.22

$$C_n{}^2 = (a\nabla\overline{n})^2 \left(\frac{d\overline{u}}{dz}\right)^{-2/3} K^{1/3} \tag{2.23}$$

To obtain an expression for the outer scale L_0, Tatarski considered two arbitrary observation points from which he then defined some scale L within the inertial range where the relation

$$C_n{}^2 L^{2/3} = (\nabla\overline{n})^2 L^2 \tag{2.24}$$

holds. He termed the left–hand side of Equation 2.24 the *fluctuational difference* and the right–hand side he termed the *systematic difference*. Substituting Equation 2.23 into 2.24 and simplifying, we obtain

$$L_0^2 = \frac{K}{d\overline{u}/dz} \tag{2.25}$$

where $L_0 = La^{-3/2}$. An alternative form for the energy dissipation rate can be found from Equations 2.25 and 2.22, that is

$$\epsilon = bL_0^2 \left(\frac{d\overline{u}}{dz}\right)^3 \tag{2.26}$$

where b is a constant which is normally taken as unity. Furthermore, if we substitute Equations 2.6, 2.25 and 2.26 into 2.13, a convenient form for $C_n{}^2$ is obtained

$$C_n{}^2 = a^2 L_0^{4/3} (\nabla\overline{n})^2 \tag{2.27}$$

A more correct form for this equation includes a constant α' (see, for example, GAGE *et. al.*, 1980), which is just the inverse of the Prandtl number. From Equations 2.26 and 2.27 and assuming $n = n(z)$, a useful relationship is obtained which relates ϵ to $C_n{}^2$, i.e.,

$$\epsilon = (C_n{}^2)^{3/2} (a^2 \alpha' Ri\, \omega_B^{-2} M^2)^{-3/2} \tag{2.28}$$

where $d\overline{u}/dz = {\omega_B}^2/Ri$, Ri is the gradient Richardson number, $d\overline{n}/dz \equiv M$ and ${C_n}^2 = a^2\alpha' L_0^{4/3}(d\overline{n}/dz)^2$. This is the same relationship which was derived by GAGE *et. al.* (1980) for determining the energy dissipation rates from radar measurements of the refractive index structure constant.

2.4 The Gradient of the Radio Index of Refraction

The variability of the returned signal strengths from the lower atmosphere using VHF radars is due to variations in the radio refractive index. Returned radar signals may be considerably enhanced due to unusual meteorological effects producing layers of enhanced refractive index fluctuation with height. Assumed profiles of the refractive index have been used in model calculations (see, for example, EATON *et. al.*, 1988). In the following paragraphs, the classical equation for the radio refractive index will be considered and an equation for the gradient of the radio index of refraction M derived.

2.4.1 Polarisation and the Dielectric Constant

Let us begin with a brief description of the two main mechanisms which can result in the polarisation of a medium. The first mechanism involves an atom which has no dipole moment. When a field $\mathbf{E}$ is applied the nucleus and the electrons move with respect to one another and the atom acquires a dipole moment $\mathbf{p}$, which is proportional to $\mathbf{E}$, that is $\mathbf{p} = \alpha_0\mathbf{E}$, where α_0 is the polarisability of the atom. This is called *electronic* or *induced polarisation* and it is operative in all dielectric materials.

The second case applies to polar molecules, in which the disposition of the individual atoms within a molecule is such that the molecule itself has a permanent dipole moment. Water (H_2O) is polar because the ions are arranged in a triangle, while carbon dioxide (CO_2) is non–polar because the carbon and oxygen atoms are arranged in a straight line with the carbon in the middle. In zero field the permanent dipoles will be randomly oriented and the system has no net polarisation, but an electric field will tend to align the dipoles and the medium will acquire a net moment. This is called *orientational polarisation.* Due to the randomising effect of the thermal vibrations this type of polarisation is more effective as the temperature is decreased and it gives rise to a dielectric constant

which is temperature dependent.

To derive an expression for the refractive index of air we shall make use of the *general* refractive index expression

$$n = \sqrt{\mu\epsilon} \tag{2.29}$$

where the permeability μ can be assumed to be approximately unity for air. In what follows we will derive an expression for the dielectric constant ϵ for moist air.

When a high–frequency radio field is applied to a liquid polar medium, the polarisation P is given by DEBYE (1957) as

$$\begin{aligned} P(\omega) &= \frac{\epsilon - 1}{\epsilon + 2}\frac{M_w}{\rho} \\ &= \frac{4\pi N_A}{3}\left[\alpha_0 + \frac{\mu^2}{3kT}\frac{1}{1 + i\omega\tau}\right] \end{aligned} \tag{2.30}$$

where M_w is the molecular weight, ρ the density of the medium, N_A is Avogadro's number, α_0 the average polarisability of the molecules in the medium — assuming no interaction between the molecules; μ the permanent dipole moment, k is Boltzmann's constant, T the absolute temperature, τ the relaxation time required for external field–induced orientations of the molecules to return to random distribution after the field is removed, and $\omega = 2\pi f$ where f is the frequency of the external field. Equation 2.30 may be simplified if we consider that for radio field frequencies of $f < 100$ GHz, we have $\omega\tau \ll 1$, *i.e.*,

$$\frac{\epsilon - 1}{\epsilon + 2}\frac{M_w}{\rho} = \frac{4\pi N_A}{3}\left[\alpha_0 + \frac{\mu^2}{3kT}\right] \tag{2.31}$$

The result for non–polar gases is found by using $\mu = 0$ in Equation 2.31, thus simplifying it even further to give us

$$\frac{\epsilon - 1}{\epsilon + 2}\frac{M_w}{\rho} = \frac{4\pi N_A \alpha_0}{3} \tag{2.32}$$

or, for gases at low pressures (i.e., $\epsilon \approx 1$), we have that

$$\epsilon - 1 \approx \frac{\rho}{M_w} 4\pi N_A \alpha_0 \tag{2.33}$$

Next, assuming the perfect gas law (i.e., $P = \rho RT/M_w$), we have that

$$\epsilon - 1 = K_1' \frac{P}{T} \tag{2.34}$$

Similarly, Equation 2.31 may be rewritten, for the case where non–polar gases are concerned, as

$$\epsilon - 1 = K_2' \frac{P}{T}\left(A + \frac{B}{T}\right) \tag{2.35}$$

where K_1', K_2', A and B are constants.

For a mixture of gases, Dalton's law of partial pressures is assumed to hold with the result that we can sum the effects of polar and non–polar gases and obtain

$$\epsilon - 1 = \sum_i K_{1i}' \frac{P_i}{T} + \sum_j K_{2j}' \frac{P_j}{T}\left(A_j + \frac{B_j}{T}\right) \tag{2.36}$$

For the troposphere, only the effects of CO_2, dry air (non-polar) and water vapor need be considered, thus

$$\epsilon - 1 = K_{11}' \frac{P_d}{T} + K_{21}' \frac{e}{T}\left(A + \frac{B}{T}\right) + K_{12}' \frac{P_c}{T} \tag{2.37}$$

where P_d is the pressure of dry air, e the partial pressure of water vapor, and P_c the partial pressure of CO_2.

2.4.2 The Radio Refractive Index of Air

In the previous section we obtained an expression for the dielectric constant ϵ. In this section the radio refractive index equation will be derived. Rewriting Equation 2.29 as

$$n = [1 + (\mu\epsilon - 1)]^{\frac{1}{2}} \tag{2.38}$$

or, as an approximation

$$n - 1 \simeq \frac{\mu\epsilon - 1}{2}, \tag{2.39}$$

then we can see that

$$N = (n-1) \times 10^6 = K_1 \frac{P_d}{T} + K_2 \frac{e}{T} + K_3 \frac{e}{T^2} + K_4 \frac{P_c}{T} \tag{2.40}$$

where the $K_i, i \in \{1,2,3,4\}$ are constants and N is termed the refractivity. To be able to obtain values of the constants K_i, it is necessary to first determine N for both wet and dry atmospheric conditions. The present discussion will not evaluate K_4 as this will not affect the value for N to a great extent.

Measurements of dry air refractive index and dielectric constant at 0 °C and 1 atmosphere pressure for frequencies ranging from optical (BARRELL, 1951) through to 24 GHz (ESSEN and FROOME, 1951) produce a mean value for $(\epsilon - 1) \times 10^6$ of 575.7 ± 0.1 and a mean value for N of 288.0 ± 0.0. Here N is determined from the relation $n = \sqrt{\mu\epsilon}$ where $\mu - 1 = 0.4 \times 10^{-6}$ is used for radio frequencies to account for the permeability. The constant K_1 may now be evaluated from

$$N = K_1 \frac{P_d}{T} \tag{2.41}$$

which is just the expression in Equation 2.40 evaluated for dry atmospheric condition. Substituting in with the measured values for $N = 288.04$, $P_d = 1013.25\ mb$ and $T = 273\ K$, gives a K_1 value of

$$K_1 = 77.607 \pm 0.13$$

To determine the constants K_2 and K_3 it is necessary to make measurements of the dielectric constant of water vapor. BIRNBAUM and CHATTERJEE (1952) gave values for K_2 and K_3 as follows:

$$\begin{aligned} K_2 &= 71.6 \pm 8.5 \\ K_3 &= (3.747 \pm 0.031) \times 10^5 \end{aligned}$$

These measurements were made at microwave frequencies but were in satisfactory agreement with those of other determinations at many varying frequencies by different authors. Equation 2.40 may now be written as

$$N = 77.6 \frac{P_d}{T} + 72 \frac{e}{T} + 3.75 \times 10^5 \frac{e}{T^2} \tag{2.42}$$

If the total pressure P is given by the sum of the corresponding dry and wet partial pressures, $P = P_d + e$, then a simplified two–term expression for Equation 2.42 is obtained:

$$N = 77.6 \frac{P}{T} + 3.73 \times 10^5 \frac{e}{T^2} \tag{2.43}$$

$$= \frac{77.6}{T} \left(P + \frac{4810e}{T} \right) \tag{2.44}$$

The constants in N described above are considered to be accurate to 0.5 of a percent in N for a range of frequencies up to 30 GHz and with normally encountered ranges

Gas	9 GHz	24 GHz	72 GHz
Water vapor	60.7 ± 0.2	60.7 ± 0.2	61.0 ± 0.2
Dry air	288.10 ± 0.10	288.15 ± 0.10	287.66 ± 0.11
Oxygen	266.2 ± 0.2	266.4 ± 0.2	263.9 ± 0.2

Table 2.1: Refractivities of water vapor at 20 °C, 10 mm Hg and dry gases at 0 °C, 760 mm Hg.

of pressure, temperature and humidity. The variability of N with frequency have been studied by ESSEN and FROOME (1951) and are summarised in Table 2.1 for reference.

2.4.3 Gradient of the Radio Index of Refraction

The derivation of the Radio Index of Refraction can be found in OTTERSTEN (1969b). Let us begin with the Equation of State for an ideal gas, which relates the pressure P in millibars to the volume V of gas and the absolute temperature T, i.e.

$$PV = nRT \tag{2.45}$$

where n is the number of moles and R is Boltzmann's constant.

For atmospheric work it is inappropriate to talk of "the volume of gas", and a more appropriate term is its density ρ, which equals the mass m of gas divided by its volume, i.e. $\rho = m/V$. A similar argument is applied to the mass m, which is related to n and the molecular weight M_w by $n = m/M_w$. With this background, the density of air can be written as

$$\rho = \frac{nM_w}{V} \tag{2.46}$$

or, after substituting Equation 2.46 into Equation 2.45, we have that

$$P = \rho\frac{RT}{M_w} \tag{2.47}$$

Another equation of interest is the Hydrostatic Equation, which is given by

$$dP = -\rho g dz \tag{2.48}$$

where g is the acceleration due to gravity and z is the height in metres (HOUGHTON, 1986; HOLTON, 1972). Dividing Equation 2.48 by Equation 2.47, this gives us

$$\frac{dP}{dz} = -p\frac{M_w g}{RT} \tag{2.49}$$

The main consequence of the Radio Refractive Index Equation is in its ability to best describe turbulent mixing. When air parcels are displaced in the atmosphere due to turbulent mixing, there exist inhomogeneities due to differences between the displaced parcels and its environment. The tendency of the "system" now is for the pressure of the displaced parcels to equilibrate with that of its environment, resulting in a change in both the temperature[3] and water vapor of the displaced parcels. However, both their potential temperature $\theta(T, P, z)$ and specific humidity $q(e, P, z)$ are preserved. Consequently, the resulting inhomogeneities in refractive index are best characterised by the differences in potential temperature and specific humidity between the regions exchanging air parcels. The mean vertical gradient M describing these differences is (TATARSKI, 1961, p.57)

$$M = \frac{\partial N}{\partial z} \tag{2.50}$$

$$= \left(\frac{\partial N}{\partial \theta}\frac{\partial \theta}{\partial z} + \frac{\partial N}{\partial q}\frac{\partial q}{\partial z}\right) \times 10^{-6} \tag{2.51}$$

Since $n = n(z)$, Equation 2.50 may also be written as $M = dn/dz$.

To expand Equation 2.51 it is necessary to use appropriate expressions for the potential temperature and the specific humidity. The following equations are assumed:

$$q = \frac{e}{1.62P} \tag{2.52}$$

$$\theta = T\left(\frac{P_0}{P}\right)^{2/7} \tag{2.53}$$

where P_0 is a reference pressure, normally taken to be the 1000 mb level. Substitute for e and T from Equations 2.52 and 2.53 into Equation 2.44 to obtain the following expression for N:

$$N = 77.6\frac{P}{\theta}\left(\frac{P_0}{P}\right)^{2/7}\left[1 + \frac{7800q}{\theta}\left(\frac{P_0}{P}\right)^{2/7}\right] \tag{2.54}$$

A partial differentiation of N with θ and of N with q produces the following results:

$$\frac{\partial N}{\partial \theta} = -77.6\frac{P}{\theta^2}\left(\frac{P_0}{P}\right)^{2/7}\left[1 + 15600\frac{q}{\theta}\left(\frac{P_0}{P}\right)^{2/7}\right] \tag{2.55}$$

$$\frac{\partial N}{\partial q} = 77.6\frac{P}{\theta}\left(\frac{P_0}{P}\right)^{2/7}\left[\frac{7800}{\theta}\left(\frac{P_0}{P}\right)^{2/7}\right] \tag{2.56}$$

[3]The change in temperature is not really a response to try and equilibrate with the environment, but is in fact an adiabatic process.

Using the Chain Rule expression (Equation 2.51), and the expressions involving the partial derivatives of N with θ and that of N with q, we arrive (after some rearranging) at the desired expression for the gradient of the index of refraction:

$$M = -77.6 \times 10^{-6} \frac{P}{T} \left(\frac{\partial \ln \theta}{\partial z} \right) \left[1 + \frac{15500q}{T} \left(1 - \frac{1}{2} \frac{\partial \ln q/\partial z}{\partial \ln \theta/\partial z} \right) \right] \qquad (2.57)$$

Manipulation of (2.56) actually produces a quantity "15600", but we have substituted 15500 because this is more consistent with recent, more accurate measurements of constants like those in Equation 2.40.

Chapter 3

Determining $\bar{\epsilon}$ From Radar Measured $C_n{}^2$

3.1 Introduction

Small scale atmospheric events are to a large extent random in nature; therefore, the best means of studying such an event is to use statistics. From a knowledge of the statistical nature of wind shears (the latest model also includes the stability and humidity 'fine structures' — see VANZANDT *et. al.*, 1981; WARNOCK and VANZANDT, 1985), VANZANDT *et. al.* (1978) were able to determine the turbulent eddy dissipation rate within the radar volume $\bar{\epsilon}$ from its radar averaged measured value. This type of model calculation can be used for obtaining profiles of $\bar{\epsilon}$ over long periods of time, much like wind profiling, even though the calculated instantaneous values may be out by as much as an order of magnitude, depending on the condition of the atmosphere (WEINSTOCK, 1981).

In this chapter we shall give an indepth discussion of the equations which were derived for the determination of the various parameters used in calculating the energy dissipation rate values for the troposphere and stratosphere. To obtain absolute values of ϵ it is necessary to do a calibration, and Section 3.2 will deal with the calibration side of the work. In Section 3.3, the expression for the reflection coefficient $\overline{\zeta^2}$ will be presented, and Section 3.4 discusses the turbulence model of VANZANDT *et. al.* (1978).

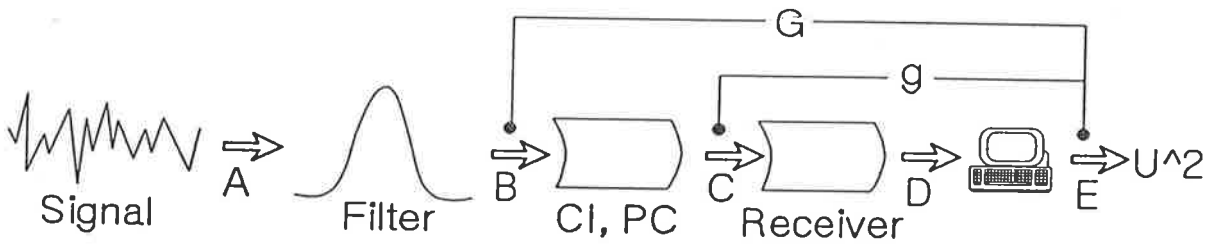

Figure 3.1: A diagramatical representation of a radar signal processing procedure.

3.2 Absolute Calibration of Radar Receivers

To determine the absolute value of the kinetic energy dissipation rate, the radar system used must be calibrated against some known parameter. With the Buckland Park VHF system, this is done by feeding a known noise temperature source, from a reliable signal noise generator, into the receiver as shown in Figure 3.1 in order to determine the gain g at stage C. It is not important to know the order in which the operations takes place, but only that the gains before and after the coherent integration/pulse coding stage be determined. It is also not relevant as to which type of pulse coding technique is used, whether it be the Barker code or the Complementary code (for a discussion on Complementary coding refer to SCHMIDT *et. al.*, 1979).

Let N be the number of coherent integrations. Then the signal at C can be thought of as an improvement over the signal at stage B by a factor which is the coherent integration (HOCKING *et. al.*, 1983b), that is,

$$V_C = NV_B \tag{3.1}$$

To determine g we need to know the power at point B, and this is given by

$$P_B = kT \int_{-\infty}^{+\infty} F(f)\, df \tag{3.2}$$

where $F(f)$ is the receiver power frequency response function, k is Boltzmann's constant, and T the absolute noise temperature. Now, let f_{eq} be the equivalent frequency band–

width, where

$$f_{eq} = \int_{-\infty}^{+\infty} F(f)\, df \tag{3.3}$$

Then, from $P_B = \overline{V_B{}^2}/2R$, we arrive at an expression for $\overline{V_B{}^2}$, where

$$\overline{V_B{}^2} = 2RkTf_{eq} \tag{3.4}$$

Using noise in the calibrations, we need to take into account that noise is incoherent and that VHF radars usually employ coherent integration of the signal; that is, for noise, the sum of N coherent integrations increases the total power by a factor of N times, whilst for coherent signal it increases by a factor of N^2. Therefore, from Equation 3.1, we have for noise that:

$$\overline{V_C{}^2} = N\overline{V_B{}^2} \tag{3.5}$$

Let the mean square digital units at the output (point E) be denoted by $\overline{U^2}$; then the gain G at stage B is given by

$$G^2 = \overline{U^2}/\overline{V_B{}^2} \tag{3.6}$$

$$= Ng^2 \tag{3.7}$$

One other equation needs to be derived. From Equations 3.6 and 3.7, and substituting in for $\overline{V_B{}^2}$ from expression 3.4, the gain g at stage C is

$$g^2 = \frac{1}{N}\frac{\overline{U^2}}{T}\left(\frac{1}{2Rkf_{eq}}\right) \tag{3.8}$$

where $m = \overline{U^2}/T$ is the slope of the "calibration curve" of received signal strength versus absolute noise temperature; and the slope is taken to be the linear part of the curve.

Now, gain G is obtained simply by feeding in some random noise signal from a noise–generator and measuring the output signal $\overline{U^2}$. Using Equation 3.7 one then determines g, from which $\overline{U^2}$ can be related back to an input power at point B.

3.3 RMS Voltage Reflection Coefficient, $\overline{\zeta^2}$

For total reflection from a height with zero absorption the radar equation gives the total received power as

$$P_R = \frac{P_t D^2 \epsilon^2 \lambda^2}{16\pi^2 (2h)^2} \tag{3.9}$$

where P_t is the transmitter power ($Watts$), D the array directivity, ϵ the system efficiency, λ the radar wavelength (m), and h the height of scatter (m). The efficiency of the system is here taken to be between the transmitter (or receiver) and the final aerial stage, while P_t is the effective power after the transmitted pulse has been convolved with the filter impulse response.

The square of the reflection coefficient is defined as the ratio of the mean signal peak power actually received P_r to the total received power which would have been received in the case of total reflection and zero absorption P_R. This ratio is given as

$$\overline{\zeta^2} = \frac{P_r}{P_R} \tag{3.10}$$

where $P_r = \overline{V_B{}^2}/2R$, V_B is the signal voltage at point B (see Figure 3.1), and R is the input impedance (50 Ω). From Section 3.2, Equations 3.6 and 3.7 give us

$$\overline{V_B{}^2} = \overline{U^2}/G^2 \tag{3.11}$$

In the event that some attenuation of the signals is required (for example, when the receiver gain saturates for some signal strengths, in particular for lower tropospheric heights), then Equation 3.11 becomes

$$\overline{V_B{}^2} = \frac{\overline{U^2}}{Ng^2} 10^{dB/10} \tag{3.12}$$

where dB is the attenuation (if any) in decibels applied at the receiver stage.

The expansion of Equation 3.10 using $\overline{V_B{}^2}$ from Equation 3.12 leads to the following result

$$\overline{\zeta^2} = \frac{1}{N}\left(\frac{\pi h}{gD\epsilon\lambda}\right)^2 \frac{32\overline{U^2}}{P_t R} 10^{dB/10} \tag{3.13}$$

where g^2 is given by Equation 3.8. Finally, combining Equations 3.13 and 3.8, we obtain an expression for the reflection coefficient which can be experimentally determined, *i.e.*

$$\overline{\zeta^2} = \frac{32kf_{eq}}{mP_t}\left(\frac{\pi h}{D\epsilon\lambda}\right)^2 \overline{U^2} \tag{3.14}$$

where $\overline{U^2}$ is the actual signal strength in digital units squared as measured with the radar and m is defined in Equation 3.8 as the ratio of $\overline{U^2}$ (during calibration) with the absolute noise temperature T. If one now assumes isotropic turbulence that fills the radar volume,

Radar Parameters	
Operating frequency	54.1 MHz
Average transmitted power	20 kW
Coherent integration	1024 points
Pulse repetition frequency	4096 Hz
Input impedance	50 Ω
Effective pulse length	7 μ s
Equivalent receiver frequency BW	0.356 MHz
θ_{HPHW}	0.0278^c or 1.5928°
$\theta_{1/2}(\equiv \theta_{HPHW}/\sqrt{2})$	0.0197^c or 1.1287°
Directivity	36.45 dB
Transmitter efficiency	0.37[1]

Table 3.1: Parameters for the Adelaide VHF radar. Use $\theta_{1/2}$ when using the same antenna for both transmission and reception, otherwise use θ_{HPHW} as the value for $\theta_{1/2}$.

then the refractive index structure constant $C_n{}^2$ is related to $\overline{\zeta^2}$ by the following relation (HOCKING and VINCENT, 1982)

$$C_n{}^2 = \frac{\lambda^{1/3}}{0.38}\left(\frac{\ln 2}{\theta_{1/2}{}^2 L}\right)\overline{\zeta^2} \tag{3.15}$$

where $\theta_{1/2}$ is the radar half–power–half–width (for transmission and reception polar diagrams combined) in radians, and L (equal to one half the true pulse–length) is the effective pulse–length in metres.

To summarise: the rms voltage reflection coeficient is calculated using expression 3.14, where m is determined from a calibration of the receiver, by feeding in some random noise signal with absolute noise temperature T from a noise–generator, and measuring the output signal voltage $\overline{U^2}$. Then the slope for the linear part of the $\overline{U^2}$ *vs* T (or calibration) curve is determined. Other parametric values determined for the Adelaide VHF radar are summarised in Table 3.1. The transmitter efficiency was determined using the method described in Appendix E.

Having now determined $\overline{\zeta^2}$, we use Equation 3.15 to calculate the refactive index structure constant. The relationship between $\overline{C_n{}^2}$ and the average kinetic energy dissipation rate $\bar{\epsilon}$ will now be considered.

[1] As measured by D. Neudegg, 1987.

3.4 Statistical Model for $C_n{}^2$ and $\bar{\epsilon}$

The notion that radar scattering occurs within layers/structures not filling the entire radar sample volume was first considered by KROPFLI (1971), who later corrected for his results using a *filling factor*, which he determined from *in situ* aircraft measurement of wind speed, temperature and humidity. This then allows the energy dissipation rates calculated from the radar and radiosonde data to be consistent with those derived from velocity spectra (one of 3 methods Kropfli used to calculate the energy dissipation rates).

3.4.1 Local $C_n{}^2$ *vs.* Radar Averaged $C_n{}^2$

To begin, let us consider the gradient of the refractive index structure constant for *turbulence* which is generated by shear instability in a hydrostatically stable region of the free atmosphere. Using the turbulence parameters derived by TATARSKI (1961), *viz.* the refractive index structure constant $C_n{}^2$ and the energy dissipation rate ϵ, which are given by the equations:

$$C_n{}^2 = a^2 \alpha' L_0^{4/3} \left(\frac{dn}{dz}\right)^2 \tag{3.16}$$

$$\epsilon = b \left(\frac{d\bar{u}}{dz}\right)^3 L_0^2 \tag{3.17}$$

where dn/dz is the refractive index gradient, L_0 is the outer scale of turbulence, a_n^2 ($\approx$ 2.8) is a universal dimensionless constant characteristic of the turbulence spectra of passive additives, α' is the ratio of Eddy Refractivity Diffusivity K_n to Eddy Viscosity K_M — Ottersten implicitly takes this as 1.0; $d\bar{u}/dz$ is the shear in the mean wind, and b is a constant equal to unity. Then, given values of $C_n{}^2$ it would be possible to determine L_0, which implies that ϵ may be determined from the relationship given by Equation 3.17. By this argument, and noting that $d\bar{u}/dz = (\omega_B{}^2/Ri)^{1/2}$, where $\omega_B = (g\partial ln\theta/\partial lnz)^{1/2}$ is the Brunt Väisälä frequency and Ri is the gradient Richardson number, GAGE and BALSLEY (1978) gave this relationship in the following form,

$$C_{n,t}{}^2 = a_n^2 \alpha' Ri_c \, \omega_B{}^{-2} \epsilon_t{}^{2/3} M^2 \tag{3.18}$$

where ${C_{n,t}}^2$ is the local refractive index structure constant, Ri_c (= 0.25) is the critical gradient Richardson number[2], and M is the gradient of index of refraction. The other parameters are θ ($\equiv T(P/P_0)^{2/7}$), P, P_0, T and q corresponding to potential temperature, atmospheric pressure (mb), a reference pressure (take this to be the 1000 mb level), absolute temperature and specific humidity, respectively.

Taking all the constants into the equation, we have that

$$ {C_{n,t}}^2 = 0.7{\epsilon_t}^{2/3}(M^2/{\omega_B}^2) \tag{3.19} $$

VANZANDT *et. al.* (1978), considered the fact that generally the radar volume is not completely filled with turbulence, but that only a small fraction of the volume is filled. This *filling factor* F can be used to relate the *radar volume-averaged* $\overline{{C_n}^2}$ measurement to the *local* refractive index structure constant ${C_{n,t}}^2$, *i.e.*

$$ \overline{{C_n}^2} = F{C_{n,t}}^2 \tag{3.20} $$

A similar argument can be applied to the kinetic energy dissipation rate equation, *i.e.*

$$ \bar{\epsilon} = F\epsilon_t \tag{3.21} $$

where $\bar{\epsilon}$ is the mean value of the energy dissipation rate averaged over the radar volume — including non-turbulent regions — and ϵ_t is the energy dissipation rate within a turbulent layer.

A direct substitution of Equations 3.20 and 3.21 into 3.19 produces

$$ \overline{{C_n}^2} = 0.7F^{1/3}\left(M/\omega_B\right)^2 \bar{\epsilon}^{2/3} \tag{3.22} $$

The gradient of the index of refraction is (Equation 2.57)

$$ M = -77.6 \times 10^{-6}\frac{P}{T}\left(\frac{\partial ln\theta}{\partial z}\right)\left[1 + \frac{15500q}{T}\left(1 - \frac{1}{2}\frac{\partial lnq/\partial z}{\partial ln\theta/\partial z}\right)\right] \tag{3.23} $$

Let χ be the expression in the square brackets; then Equation 3.22 can be rewritten, after substitution and some simplification, as

$$ \overline{{C_n}^2} = 4.2 \times 10^{-9}\frac{F^{1/3}\chi^2}{{\omega_B}^2}\left(\frac{P}{T}\frac{\partial ln\theta}{\partial z}\right)^2 \bar{\epsilon}^{2/3} \tag{3.24} $$

[2]Theoretical analysis shows that the critical Richardson number for instability is 0.25 or, more precisely, that $Ri > 1/4$ is sufficient for stability and that $Ri \leq 1/4$ is necessary but not sufficient for instability. See Appendix E for a discussion.

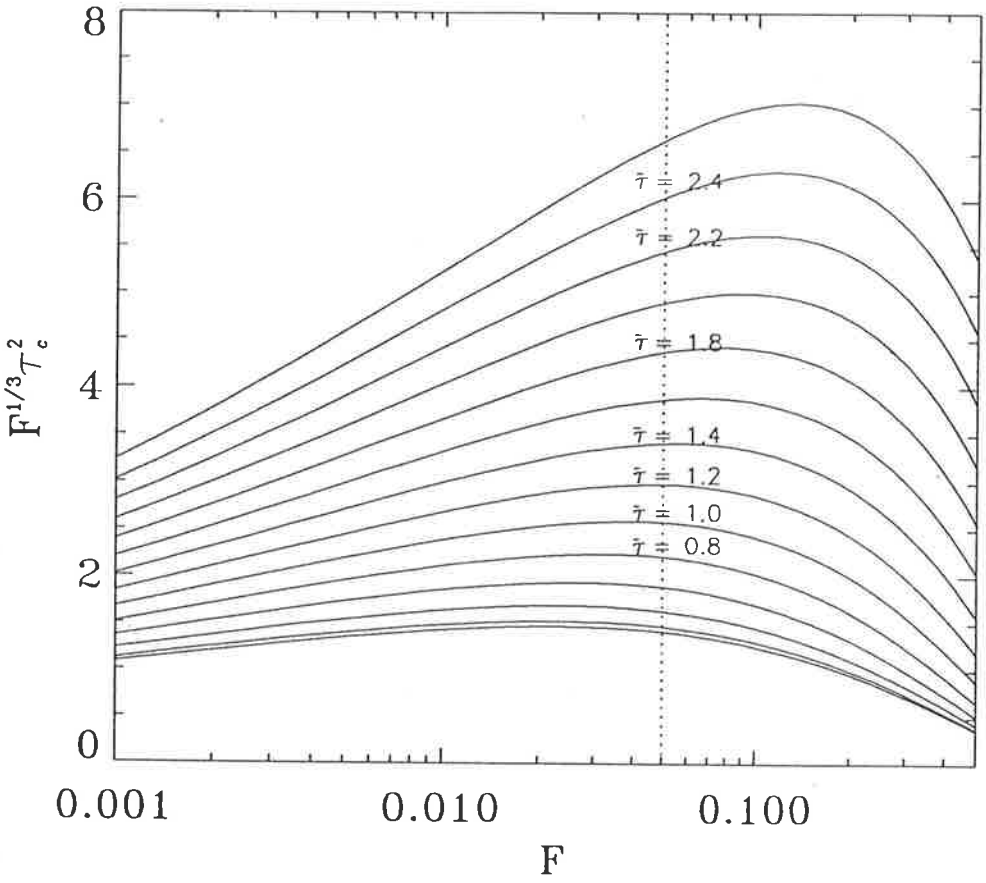

Figure 3.2: A turbulence model plot of $F^{1/3}\tau_c^2$ with F and $\bar{\tau}$ — see text.

Furthermore, from the Brunt Väisälä frequency expression, we have that $\partial ln\theta/\partial z = \omega_B{}^2/g$, which when substituted into Equation 3.24 and making $\bar{\epsilon}$ the subject of the equation, we have that

$$\bar{\epsilon} = 3.5 \times 10^{15} \left(\frac{T}{P}\right)^3 \left(\frac{\overline{C_n{}^2}}{F^{1/3}\omega_B{}^2}\right)^{3/2} \chi^{-3} \tag{3.25}$$

Equation 3.25 enables one to calculate, assuming turbulence is the cause of the radar scatter, the kinetic energy dissipation rate from the radar measured refractive index structure constant. In addition, pressure, temperature and humidity measurements from radiosondes are required for determining $\bar{\epsilon}$. The only other unknown is the *filling factor* F, which has been experimentally determined by aircraft measurements to lie in the range $0.01 < F < 0.1$ (GAGE *et. al.*, 1980).

3.4.2 The Statistical Distribution of Wind Shears

To calculate $F^{1/3}\omega_B{}^2$, the model of VANZANDT *et. al.* (1978) is used. This simple model is based upon the statistical distribution of wind shears, which in its simplest form can be

compared to the Rayleigh Distribution. To represent the random nature of wind shears, the instantaneous values (as per kilometre altitude) can be written as a mean component $\bar{s}$ plus its fluctuating component s' (also termed microshear or variance), that is,

$$s = \bar{s} + s' \tag{3.26}$$

Assuming that the microshear s' is distributed according to the Gaussian Distribution Function $Z(x)$, which can be described by its two moments, *viz.* mean μ and variance σ, then

$$Z(x) = \frac{1}{\sqrt{2\pi}} \exp\left(\frac{-(x-\mu)^2}{2\sigma^2}\right) \tag{3.27}$$

or, as

$$Z(s'/\sigma') = \frac{1}{\sqrt{2\pi}} \exp\left(-\frac{1}{2}(s'/\sigma')^2\right) \tag{3.28}$$

where by definition $\bar{s'} = 0$, and σ' is the variance of the microshear: VANZANDT *et. al.* (1978) have taken σ' to be 0.010 s^{-1} in the troposphere and 0.015 s^{-1} in the stratosphere. Before we proceed, let us define some turbulence parameters. The normalised critical shear τ_c is defined as the ratio of the critical shear s_c to the variance of the microshear σ', where the critical shear s_c ($\equiv g\partial ln\theta/\partial z/Ri$) is that total shear which gives rise to turbulence — this occurs when the gradient Richardson number $Ri \leq 1/4$. Similarly, the normalised shear is given by $\tau = s/\sigma'$.

The probability f for a total shear to occur between s and $s + ds$ is given by the Normalised Gaussian Function, where

$$f(s)\,ds = Z([s - \bar{s}]/\sigma')\,ds/\sigma' \tag{3.29}$$

If we now assume that the atmosphere is turbulent when the size of the total shear is at least greater than the size of the critical shear, *i.e.*, when $\mid s \mid \geq \mid s_c \mid$, then the probability F that a given height is turbulent is given by

$$\begin{aligned} F(\mid \tau_c \mid, \mid \bar{\tau} \mid) &= \int_{-\infty}^{-|s_c|} f(s)\,ds + \int_{+|s_c|}^{+\infty} f(s)\,ds \\ &= P(-\mid \tau_c \mid - \mid \bar{\tau} \mid) + Q(\mid \tau_c \mid - \mid \bar{\tau} \mid) \end{aligned} \tag{3.30}$$

where $P(x)$ is the Cumulative Distribution Function of $Z(x)$, and $Q(x) = 1 - P(x)$.

Equation 3.25 may now be determined by a change of variable. For the onset of turbulence, let $Ri = 1/4$; this implies that the critical shear is now

$$\begin{aligned} s_c^2 &= g\frac{\partial ln\theta}{\partial z}/Ri \\ &= 4{\omega_B}^2 \end{aligned} \tag{3.31}$$

In addition, from the normalised critical shear expression, we have that

$$s_c^2 = 4{\omega_B}^2 = \tau_c^2 s_c'^2 \tag{3.32}$$

or, after multiplying both sides by F and rearranging, the required expression is

$$F^{1/3}{\omega_B}^2 = \frac{s_c'^2}{4} F^{1/3}\tau_c^2 \tag{3.33}$$

From this, it is possible to calculate, using statistical analysis of wind shears, the kinetic energy dissipation rates. To summarise, F is calculated using Equation 3.30, where the critical shear is determined from Equation 3.31 and the mean wind shear is calculated from balloon measurements of the mean horizontal winds. Finally, the normalised shears can be obtained assuming $\sigma' = 0.010\ s^{-1}$ in the troposphere and $0.015\ s^{-1}$ in the stratosphere.

Chapter 4

Experimental Techniques

4.1 Introduction

The aim and purpose of this chapter is to give an account of the experimental work undertaken for this thesis. However, due to the nature of the work, in which a large portion of it is computational work involving programming, it would not be possible to document all the programs which were written. However, where possible, a brief description will be given on certain programming techniques used in some of the calculations. The titles for our discussion will be as follows:

1. Retrieving data from radiosondes.
2. Absolute calibration of the radar.
3. Radar beam tilting.
4. Data handling and computation.

Items (2) and (3) deal principally with the design and implementation of hardware (electronic or otherwise) for an *indirect* modification to the radar, and item (4) is concerned with the software (computer programs) used for data collection, handling and analysis. By *indirect* modification, the implication is that of a temporary modification to the existing equipment, i.e., not an internal/permanent modification. Such temporary measures for the Adelaide VHF radar were found to be necessary in the course of this project work, particularly in relation to the calibration of the radar. The experimental work involves two important types of equipment; a VHF radar, and radiosondes. Let us begin by briefly describing the work involving radiosondes.

4.2 Retrieving Data From Radiosondes

In order to make humidity corrections to obtain the optical $C_n{}^2$, it was necessary to take measurements of temperature and humidity. The closest station to the radar site was the Adelaide airport, where radiosondes are launched every 12 hourly, starting at 0830 CST. For a description of the type of radiosonde used, refer to Appendix C. There were two phases to this work, a result of changes to the Bureau of Meteorology's radiosonde operation, with the introduction of a new computing network (with such facilities as real–time editing from the computer terminal, easy access to archived data, etc) in the second phase, which also enabled archiving of data from all radiosonde flights. However, during the initial phase, due to the Bureau's practice of making available calculations of only standard and significant level profiles, it was necessary to collect the data by interfacing a personal computer to the receiver of the radiosonde (Information on the radiosonde receiver's serial output is given in Table C.2). To process the raw data we used the same Väisälä program and obtained a fine vertical resolution of approximately 50 m. For further information on the radiosonde work, refer to Appendix C.

With the installation of the new system, the digitised data from all radiosonde flights are directly displayed and edited in real time from a computer terminal. Using the standard Väisälä program, which interpolates profiles of temperature T, Pressure P and Humidity U, other parameters such as the Brunt Väisälä frequency and specific humidity can be determined at standard levels of the atmosphere. These and the raw data files are then archived.

4.3 Absolute Calibration of the Radar

In the world today, a large number of MST (Mesosphere–Stratosphere–Troposhere) and ST (Stratosphere–Troposphere) radars are available for the study of atmospheric turbulence. Therefore, for the purpose of a world–wide comparison of such calculated parameters as the backscater cross–sections of the scatterers or the reflection coefficients of the reflectors from the power received, it is necessary to calibrate the radar. One such method is to determine the signal–to–noise (S/N) ratio, from which an approximate measure of

the received power may be obtained by reading off the noise level from standard sky–noise charts[1]. This method only works well for VHF radars, where noise is mainly due to extra–terrestrial sources, while MF and HF radars are sensitive to other additional atmospheric noise sources. VANZANDT *et. al.* (1978) used this method to determine the reflection coefficient and hence the refractive index structure constant.

A better method of calibration, as presented by HOCKING and RÖTTGER (1983), is to use a noise generator to calibrate the receiver. To do this, a random–noise–producing signal generator was used as a known calibration source, and this is fed into the receivers at the point where the receiving antennas are normally connected; measurements of received signal strengths $\overline{U^2}$ corresponding to different settings of the random–noise signal generator temperature T can then be made (as already discussed in previous chapter). A plot of $\overline{U^2}$ *vs.* T (henceforth called a *calibration* or *gain curve*) can then be used to determine the maximum received signal strength (from atmospheric 'scatterers') which would lie within the "linear region" of the calibration curve. After a few trials, the range of gain positions on the receiver which produced an appropriate linear curve was found. However, it was later found that the "cut–off point"[2] for all the calibration curves were too low; very strong signals correspond to a non–linear region of the receiver response, making it impossible to make any calculations of turbulence parameters around the 2–3 km height range[3]. To compensate for the larger signal strengths received at lower tropospheric heights, it was suggested that the incoming signals from the Co–Co array be split into two identical signals[4]; this was accomplished with the aid of a power splitter[5]. With two identical signals, it was possible to attenuate one of the receivers to "force" any extra–large signal strengths, which would otherwise have saturated the receiver, to *stay in the linear region of the calibration curve.* Experience with the variability of signal strengths taken with the Adelaide VHF radar suggested that an extra attenuation of around 16 dB was required in one of the two receivers. One important point to note when using an attenuator at the

[1]This would introduce some error, because the true noise level varies diurnally.

[2]That is, the value of $\overline{U^2}$ for which the curve starts to deviate from a straight line.

[3]Signal strengths received from around 2–3 km height range are usually several orders of magnitude larger than those higher up.

[4]Both signals would be 3 dB down from its original strength.

[5]See Appendix H for more details.

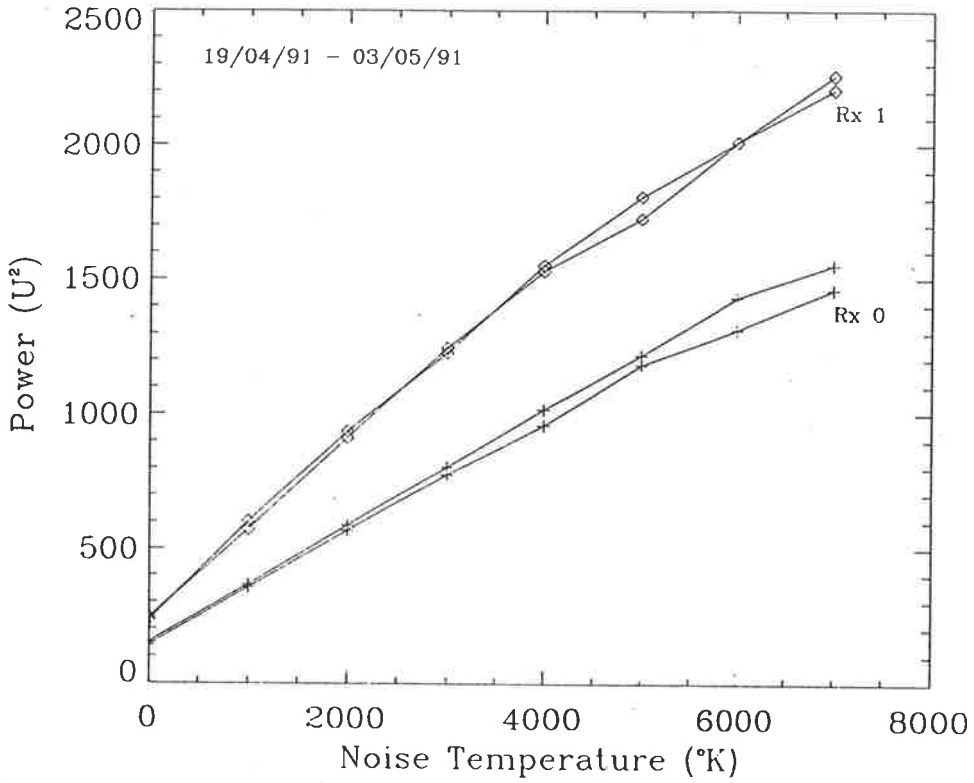

Figure 4.1: Samples of gain/calibration curves for receiver channels 0 and 1.

inputs to the receiver channels is the existence of +12 volts DC potential at these input terminals. This potential may be large enough to overload and burn the resistors in the attenuator, thereby giving wrong readings of the attenuation. To rectify this, capacitors were required at either end of the attenuator to cutout the DC component.

Figure 4.1 gives a set of *gain/calibration curves* for channels 0 and 1 respectvely, corresponding to receivers 1 and 2 of the Buckland Park VHF radar system. As seen from the plots, the form of the calibration curves — at one particular receiver gain setting — do not vary a great deal over long period of time. This can be seen as an indication that the receivers are in good and proper working order.

Separate data files were created to store the data from the two receiver channels. When analysing such data, signal strengths saturating receiver 0 would therefore be replaced by those from receiver 1. If, perchance, receiver 1 still saturates, then the data point would be considered invalid and subsequently rejected. It is to be noted that the extra attenuation of 16 *dB* for receiver 2 was a compromise between (a) loss of "resolution" in the received signal strengths and (b) some relatively strong signals would not stay within the linear range of the calibration curve.

4.4 Radar Beam Tilting

Due to a higher incidence in the occurence of *specular reflections* from a radar whose polar diagram is directed close to the zenith, it is desirable to have an off–vertical beam at some angle farther from the zenith, say 11° off–vertical (CHU *et. al.* (1990) and TSUDA *et. al.* (1986), using the Chung–Li VHF radar, have shown the range of angular dependence of echo power to lie within ±10° from zenith, above this angle there is no observable aspect sensitivity.). The implementation of a beam tilt is achieved by introducing phasing cables of appropriate lengths to the transmitting array; for example, if a westward pointing beam at an angle θ is required, then considering a one–dimensional case, we have the situation as illustrated in Figure 4.2. The cable–lengths are easily calculated from the following algorithm:

$$L_i = Abs\,(i\delta - Int\,(i\delta/\lambda)\,\lambda) \tag{4.1}$$

where $\delta = \lambda \sin\theta/2$, $i = 1 \ldots 32$, λ is the radar wavelength, *Abs* is a function which returns the absolute value to an expression and the function *Int* returns a result equal to the expression inside the bracket converted to integer type. For the Buckland Park VHF radar Co–Co array, the phasing cable–lengths were calculated assuming the transmitter building (actually a caravan) to be an antenna (or string) which is part of the array — there are 32 strings altogether making up the array (see Figure D.1). Figure 4.3 gives the calculated phasing cable–lengths for such an array for a beam pointing angle of 11° off–zenith. Whether a westward or eastward pointing polar diagram is used is a matter of choice, although it pays to position the antenna beam away from strong cosmic noise sources, thus improving on the S/N ratio. We have generally chosen to use a westward pointing beam.

4.5 Data Handling and Computation

A brief discussion on the many and varied programs written for both the collection of data using the VHF radar and the subsequent analysis of these data will be given here. Where appropriate, a one line algorithm to explain the particular technique used in the

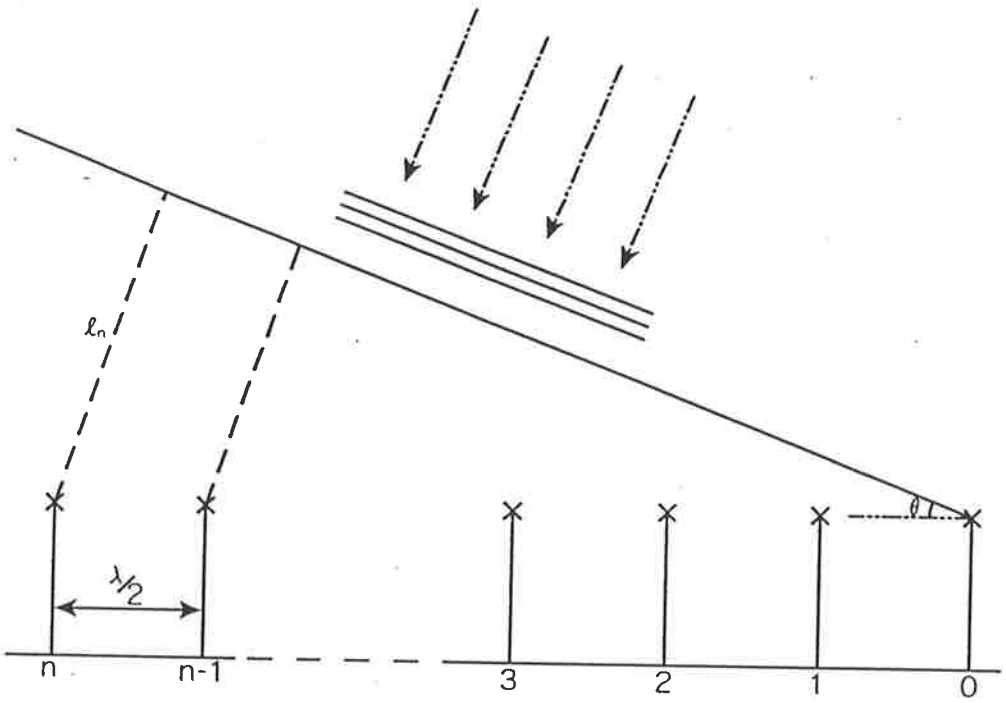

Figure 4.2: Calculating the cable–lengths for a one–dimensional array of antennae for a given angle θ and a separation distance from antenna to antenna of $\lambda/2$, where λ is the operating frequency of the radar.

calculations will be given. The section is divided into two parts: part I deals principally with software programs running on the VHF radar minicomputer, and part II discusses all the other software programs written, most of which were for analysis and for graphical presentation of the results.

4.5.1 Minor Software Programs

There already exist a large number of software programs available for the direct operation of the VHF radar, most of which were written in either Pascal or Fortran codes[6], being linked together by machine codes. All program units (i.e., procedures or subroutines) are easily accessible by other programs. It is therefore not too difficult to write a program to invoke the radar controller with the aim to start sampling and collecting data in accordance with certain preset parameters. Table 4.1 gives typical operating parameters for probing the clear air with the VHF radar. Given these typical values, the program would collect data for about 50 seconds with a total of 200 coherently integrated data

[6]Recently, an updated version written in Quick C was used as a replacement.

Phasing cable lengths with its associated connector in units of λ^{-1}

1	0.0954	**9**	0.8586	**18**	0.8127	**26**	0.5759
2	0.1908	**10**	0.9540	**19**	0.9081	**27**	0.6713
3	0.2862	**11**	0.0494	**20**	0.0035	**28**	0.7667
4	0.3816	**12**	0.1449	**21**	0.0989	**29**	0.8621
5	0.4770	**13**	0.2403	**22**	0.1943	**30**	0.9575
6	0.5724	**14**	0.3357	**23**	0.2897	**31**	0.0529
7	0.6678	**15**	0.4311	**24**	0.3851	**32**	0.1483
8	0.7632	**16**	0.5265	**25**	0.4805		

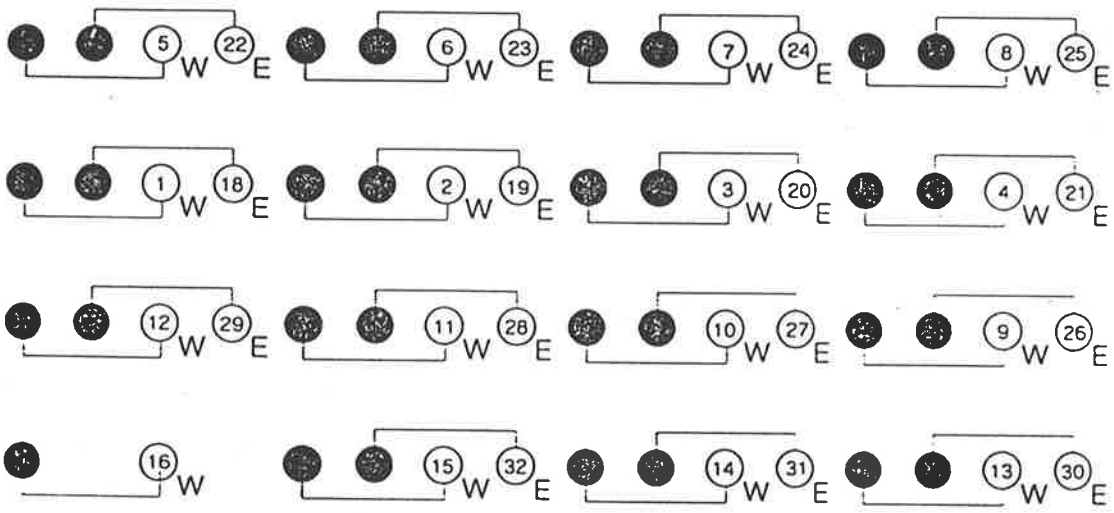

Figure 4.3: The connections for the phasing cables as used by the Adelaide VHF radar. The calculated cablelengths for each connectors are shown in units of λ^{-1}, where λ is the operating wavelength of the radar, and the beam pointing angle is 11° off vertical (westward).

Transmitting System	
Frequency	54.1 MHz
Peak power	40 kW
Mean Power	200 W
Effective pulse length	7 μs
Range resolution	1 km
Antenna area	7700 m^2
PRF	64–2048 Hz
Receiving System	
Antenna(s)	Co–Co array
Sampling interval	0.3–2 km
Maximum number of gates	256
Signal conversion	10 bit A/D
Coherent Integration (CI)	16–1024 points
Typical operation in doppler mode	
CI	1024
PRF	4096
Sample rate	0.25 s
Number of gates used	200
Record duration	50 s

Table 4.1: Operating parameters for the VHF radar as used in 1991.

points per 30 height ranges[7]. For a long campaign (say, a few days) it is desirable to store as few data points as possible: to do this, the mean value for the 200 points collected may be determined for each height, and these averages written to a file in binary format, with the 30 mean values written as long integer (i.e., 4 bytes) records of 5 rows and 6 columns. The entire process is repeated each minute.

There are three files which were opened for writing; in two of the files were stored the differing degree of attenuated data from the Co–Co receiver (i.e., from receiver 0 and receiver 1, respectively), and the third file is basically a log file where information relevant to the present run are recorded for future reference. The prefix of the filenames are of the form *yddmmhh*, where *y* is the last digit of the year, *ddmm* is the day and month of the year, and *hh* is the hour for the start of run. To facilitate an easier access to the datafiles and also as a precautionary measure against power failures[8], it was decided to run the

[7]Oversampling at every 500 metres with a height resolution of 1 km.
[8]This happens quite often at Buckland Park.

n	T ($^\circ K$)	P_R (U^2)	r
0	OFF	—	—
1	0	—	—
2	1000	—	—
3	2000	684	0.9999
4	3000	940	0.9999
5	4000	1176	0.9998
6	5000	1400	0.9995
7	6000	1605	0.9990
8	7000	1743	0.9968

Table 4.2: An example of the calibration results for the receiver pre–amplifier.

data collection program for only twelve hours, after which the *buffered* data[9] would be written to their respective files (i.e., by closing the files); the whole process can then be repeated as often as required.

Let us now consider a software program used to allow easy calibration of the receiver pre–amplifiers. This was achieved through the use of a known source of random noise temperature, *e.g.,* a signal generator (see Section 4.2). The program is similar to the one discussed above, except that it operates under slightly different conditions and with different operating parameters. The layout for the calibration program may be considered in two parts: firstly, it was necessary to check whether or not the chosen gain position on the receiver was a suitable setting (that is, is there a good linear correlation between noise–temperature and the received signal strengths?) — five points are normally used for this purpose, and the correct position(s) is found by trial and error; and secondly, once the correct position is found the calibration proper may proceed, and this is usually done for a total of nine points; a typical calibration run is shown in Table 4.2, together with their respective correlation value as calculated to that particular point. On the completion of a run, the calibrated points are appended to a calibration file with relevant information stored in its header.

[9]All collected data are temporarily stored in the computer's buffer — this would naturally imply a total loss of data when a power failure occurs during a program run.

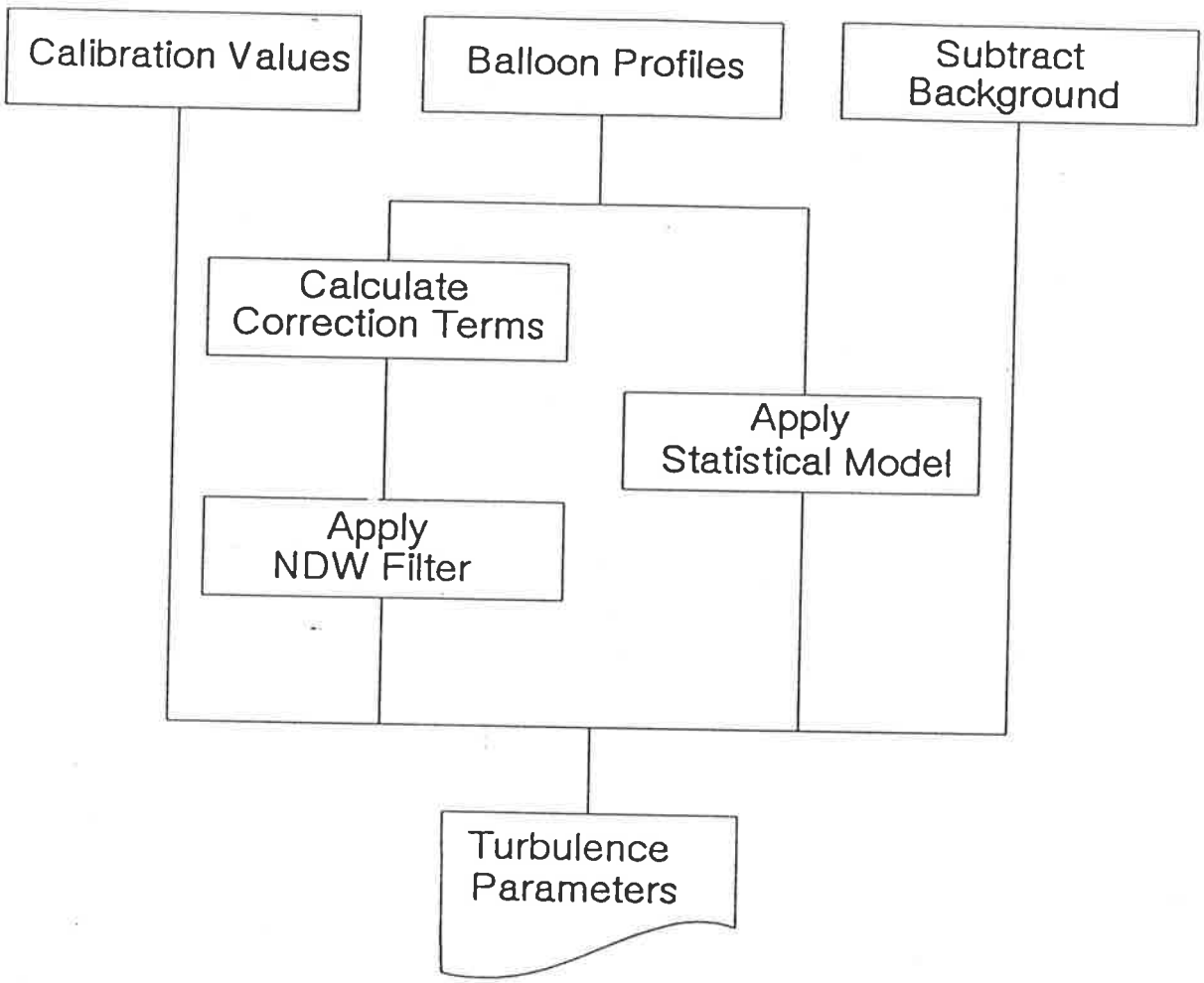

Figure 4.4: A flow chart showing the flow of processes leading to a calculation of the turbulence parameters.

4.5.2 Major Software Programs

Quite a number of software programs were written for analysing the Buckland Park VHF radar data, as well as some for analysing the data taken from balloon soundings at Adelaide airport. For our discussion we will follow the flow chart as given in Figure 4.4, which shows the different types of calculations needed in the lead up to the model calculations of the refractive index structure constant and the energy dissipation rate. Starting from the top left–hand corner of the chart and moving from top to bottom, we have the following calculations:

CALIBRATION VALUES: Initially, it was necessary to determine some relevant parameters from the calibration data. Given values of noise temperature T and received signal strengths U^2, the program used a linear regression analysis to calculate the correlation coefficient for different 'lengths' of the calibration values, which can then be used to determine the 'critical point', or the point at which the relationship between T and U^2 begins to depart from linearity. Having determined the critical point, the gradient of the straight line to this point can be calculated. From the gradient m, we can calculate the gain of the receiver channel from Equation 3.8; the critical point is used to test which of the two attenuation levels[10] is appropriate for a particular data point — if neither of the two levels is appropriae, then the point is discarded.

BALLOON PROFILES: The main program was written in Fortran, and this was adapted from an existing program commonly used by meteorological bureaus around Australia; the program was originally written in Pascal. The Fortran program was incomplete, however, because it does not apply the Väisälä–radiation correction to the temperature data. But for the purposes of our analysis, this is not of major concern, because this correction only becomes important when considering heights above the tropopause.

Raw data obtained from radiosonde flights at the Adelaide airport[11] are stored in binary format. A program to convert such files to ASCII character codes also exists. The radiosonde program would read the appropriate datafile, and if an error occurs during the reading process (this is caused by the so called *spurious signals*, which can be easily detected from their non–numeric values — usually represented by a back–slash) it prompts the user to edit the data file, and once editing has been completed, it re–reads the file. Finally, it does the appropriate analysis to give the resulting interpolated smoothed and filtered data of temperature, pressure and humidity for every 10 seconds, or a corresponding height resolution of approximately 50 metres. The program also calculates the Brunt Väisälä frequency and the mixing ratio.

With a recently introduced fully computerised system, including real–time analysis of radiosonde data, the Meteorological Bureau have been storing raw–data from all their

[10]The original signal was split using a power splitter and different attenuations were used in the respective signals.

[11]For a discussion on this subject, refer to Appendix C.

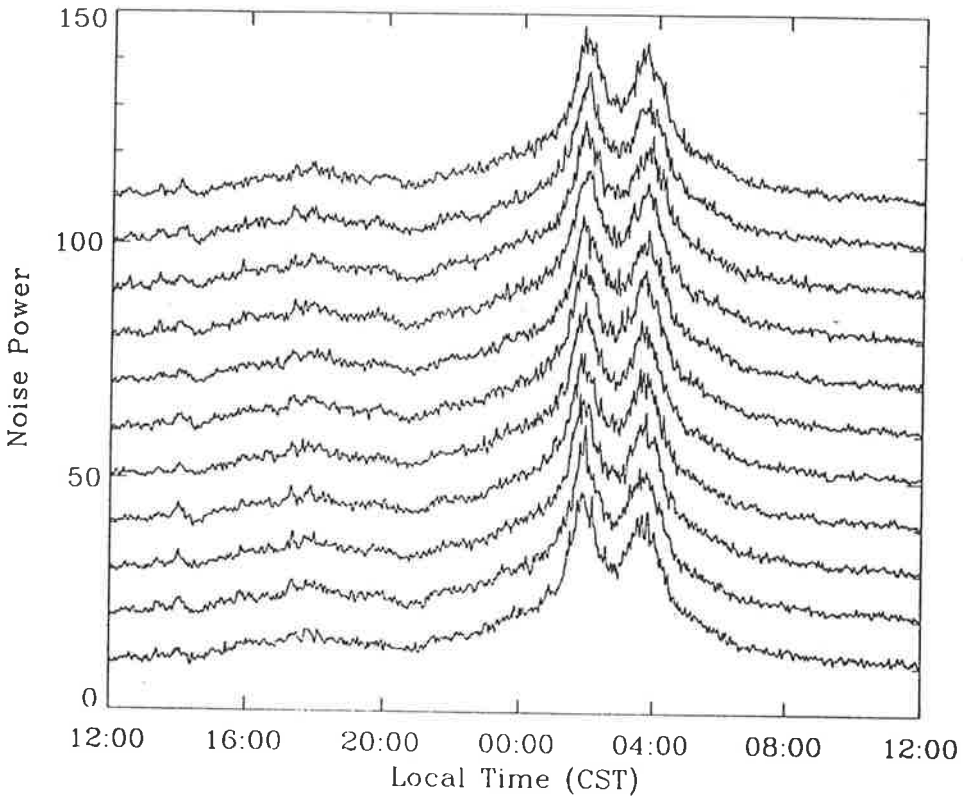

Figure 4.5: Noise profiles for heights 3–8 km. Taken at Buckland Park Research Station with a beam zenith angle of 11°.

balloon flights. Each file contains all the relevant information necessary for a re–analysis of the data at a future date.

SUBTRACT BACKGROUND: A typical noise profile for heights 3–8 km is shown in Figure 4.5. In recording the noise, the same setup as that used when recording the signals was used. It is then a simple matter to subtract off the noise from the signal values. If the result is less than 0 then the point is rejected. Two factors which require attention are: (a) noise has a diurnal variation — It was decided not to exceed 7 days between taking the noise and signal data, and (b) the earth rotates 360° on its axis every 23 hours 56 minutes and 4 seconds.

CALCULATE CORRECTION TERM: From the relationship for the gradient of the potential refractive index M (Equation 2.57), where

$$M = -77.6 \times 10^{-6} \frac{P}{T} \left(\frac{\partial \ln \theta}{\partial z} \right) \left[1 + \frac{15500q}{T} \left(1 - \frac{1}{2} \frac{\partial \ln q / \partial z}{\partial \ln \theta / \partial z} \right) \right]$$

we have called the bracketed term χ, the *correction term*, because it corrects for the contributions due to humidity in a 'wet' atmosphere. The balloon data were used to measure χ. In calculating this term, we have used the approximate relationship for the calculation of the partial derivatives, that is,

$$\frac{\partial x}{\partial y}(y_i) \approx \left| \frac{x(y_i + \Delta y) - x(y_i - \Delta y)}{2\Delta y} \right|$$

where Δy is usually between 20–40 metres. The q and T terms are specific humidity and temperature, respectively; these are taken to be the values at that particular height.

APPLY STATISTICAL MODEL: The statistical model of VANZANDT *et. al.* (1978) was used to determine the volume–averaged turbulent energy dissipation rate values: the theory was discussed in Chapter 3. The aim of this program is to calculate the quantity $F^{1/3}{\omega_B}^2$, where F is the fraction of the radar volume which is turbulent and ω_B is the Brunt Väisälä frequency. Equation 3.30 was used to calculate F, giving values of $\tau_c = s_c/\sigma_\mu$ and $\tau_m = \overline{s}/\sigma_\mu$. A typical value for the variance of the microshear σ_μ in the troposphere is around 0.010 s^{-1} and for the stratosphere 0.015 s^{-1} (VANZANDT *et. al.*, 1978). The mean wind shear $\overline{s}$ can be calculated from rawinsonde flights, which is then averaged over the troposphere (up to 8.5 km) and the stratosphere (11.5 km to 18.0 km). A similar averaging procedure is used for the critical shear $s_c \equiv 4{\omega_B}^2$. It is then a simple matter to determine the quantity $F^{1/3}{\omega_B}^2$, where values of ${\omega_B}^2$ have been filtered using the NDW filter, which we will consider next.

APPLY NORMAL DISTRIBUTION WEIGHTED (NDW) FILTER: Due to the very large range resolution of the Adelaide VHF radar ($\approx$ 1 km) compared to that of a radiosonde, it was decided to smooth such atmospheric parameters as ${\omega_B}^2$, χ and M^2, which were calculated from the much finer resolution data of the radiosonde, in a manner which will convey information with approximately the same resolution as that of the radar. This was done by convolving the true radiosonde data with a Gamma function, in line with the fact that the radar pulse is also approximately Gaussian in shape. In addition, a 5% rejection of the highest and lowest bounds in the sorted data was used before the smoothing procedure, due to the common occurrence of 'spikes'. The pseudocode for this program is given in Appendix G.

TURBULENCE PARAMETERS: For profiles of the energy dissipation rates calculated over a long time span, it was decided to use a 2 km resolution filtered data using the NDW filter as discussed above. In addition, the length of the data was restricted to 4 hours between 0700–1100 CST and 1900–2300 CST. This is in consideration of the fact that radiosondes are launched daily at 0830 CST and 2030 CST respectively, and also due to the large distance separating the radar and radiosonde sites. By specifying the start and finish time for analysis of the radar data, the program then calculates the reflection coefficient ζ, the radar measured structure constant of the refractive index $\overline{C_n^2}$, and the radar measured energy dissipation rates $\bar{\epsilon}$. Model calculations of $\overline{C_n^2}$ and $\bar{\epsilon}$ can then be made and these were later compared to the radar measured values. Heights ranging from 2 to 16 km in steps of 500 m intervals were analysed; however, the final analysis was only performed for heights between 2 and 8 km, due to the low signal–to–noise ratio above $\approx$ 8 km altitude.

The radar data from Buckland Park are subject to contamination from high–level aircraft fly–by's, and these are required to be taken out before any averaging can be done. To do this a simple routine for rejecting spikes was used. The condition for spike rejection is that a point is rejected when a data point is at least 2.5 times larger (or smaller) than the average of its 'non–spike' neighbours.

Chapter 5

Results and Discussions

5.1 Introduction

Using the original statistical model of $\overline{C_n{}^2}$ by VANZANDT *et. al.* (1978), and later modified by GAGE *et. al.* (1980) to infer the energy dissipation rates ($\bar{\epsilon}$) from radar measured $\overline{C_n{}^2}$ values, the following chapters will describe results of observations made using the 54.1 MHz doppler radar at Buckland Park, South Australia. In addition, data from radiosonde soundings of the atmosphere (such as the vertical profiles of pressure, temperature, humidity and horizontal wind speed) were used to improve the accuracy, and these were taken at the Adelaide airport[1] in co–operation with the Adelaide Weather Bureau.

The analysis presented here will, in the main, be a case study of three mornings and three evenings of data taken during the approach and passage of a cold front in the autumn month of May, 1991. Synoptic weather charts giving the situation at 0900 CST and 2100 CST during the period will be used in conjunction with discussions of the results obtained at those particular times. The break–up of the discussions will be in three major parts: in Section 5.2, all the meteorological data (and calculations made from it!) are given for the period to be analysed, in addition to a description of the weather conditions based on synoptic charts; Section 5.3 will give some results on the measurement of the refractive index structure constant made with the Adelaide VHF radar during winter, and the typical outer scales obtained; finally, the energy dissipation rate per unit mass is discussed in Section 5.4.

[1]The airport is situated some 35 km South of Buckland Park.

5.2 Preliminaries

The period beginning at 0900 CST May 3 and ending 2100 CST May 4, saw the high–pressure system as a dominant feature over the radar site, while the latter period of May 5/6, saw the effects of the approaching cold–front starting to make its presence felt, as the high is pushed further away in a north–eastward direction. The topics for discussion will include a description of the weather conditions for each of the period studied, followed by some preliminary discussion on the meteorological data obtained from the radiosonde/balloon flights and including calculations based solely on these data will be given.

5.2.1 Weather Conditions

A synoptic chart for the period May 6, at 0900 CST, is shown in Figure 5.1, on which also is superimposed the situations for the period May 03–05. The approximate position of the centre of the high–pressure system is shown by a *cross*, and the number along–side it gives the day number with respect to May, 1991; *unprimed* and *primed* numbers correspond to 0900 and 2100 CST, respectively. From a study of the synoptic chart, we have the following situation for the period May 3 at 2100 CST to May 6 at 0900 CST: a high–pressure system, with a pressure reading of 1030.7 hPa measured at Adelaide airport, is situated over South Australia on May 3 and is slowly moving eastward. By May 4 0900 hours CST, a pressure reading of 1020.9 hPa was registered at the airport. At this point in time we observe also the passage of a low–pressure system moving across the Bight towards the mainland. On the same day at 2100 CST, the high has moved across to Victoria and is heading for the Tasman sea, while the low–pressure system has yet to reached South Australia. The pressure reading recorded at the airport was 1024.7 hPa.

A weakening low–pressure system south of Western Australia is steadily moving in an east to north–east direction, as shown in the synoptic chart for May 5 at 0900 CST. With the movement of the low towards South Australia, a change in weather condition is expected throughout the state. The pressure readings measured at Adelaide airport at 0900 CST and 2100 CST for May 5, and 0900 CST for May 6 are 1015.9, 1014.9 and

1019.1 hPa, respectively.

5.2.2 Meteorological Parameters

Let us begin to describe the conditions of the atmosphere from 2 to around 9 km altitude. The height profiles of these meteorological parameteres were measured by radiosondes launched at Adelaide airport. Figure 5.2 gives the profiles of temperature, potential temperature and specific humidity for the period May 3 to May 6, where each profile is separated by 12 hours and the first vertical line shows where the succeeding profile is actually centered[2]. Our interest will mainly be concerned with the profiles of specific humidity, as this is one variable which contributes significantly to the back–scattered power of the signal received by the radar, and where a correction to the energy dissipation rate has been made from this. The potential temperature profiles are also important, because they show the regions where the temperature inversion(s) takes place, that is, regions of strong atmospheric stratification resulting in very strong echoes[3]; however, such inversions tended to be very localized (in three dimensions), and it is very unlikely that the same inversion(s) would occur 35 km away. As noted in the figure, the profiles of specific humidity are very similar for the period May 3/4. In addition, the first profile has negligible humidity contribution above 7 km altitude.

Shown in Figure 5.3 is the profiles for the horizontal wind velocity and its vertical shear. These velocity measurements are of very coarse resolution, increasing with altitude. For this reason, it was not possible to do a similar statistical analyis on the fine structures of the vertical wind shear for the Adelaide area, as was done by VANZANDT *et. al.* (1978) for their particular area, which was later used in their model calculations.

An important result for interpreting the energy dissipation rate profiles is the characteristic of positive correlation between the range–squared corrected received power, Power$\times z^2$, and the square of the mean gradient of generalized potential refractive index, M^2. Figures 5.4 and 5.5 shows the vertical profiles of log[Power$\times z^2$] and log[M^2], and the correlation coefficients r and slopes b for each of the cases studied: of note are two

[2]For specific humidity, each profile is centered at zero g/kg.

[3]In all the cases studied here, the radar polar diagram was pointed sufficiently off–vertical to negate any aspect sensitivity

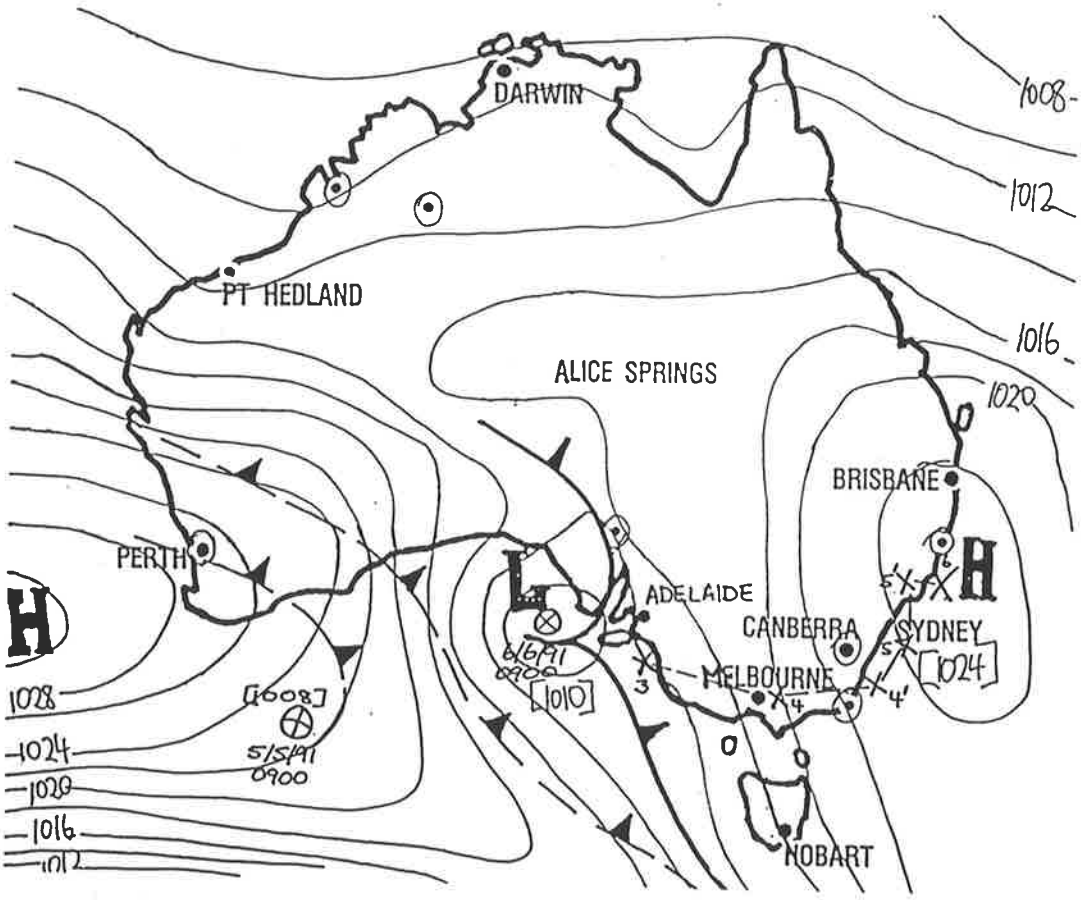

Figure 5.1: Synoptic charts for the weather situation on May 3–6, 1991 are shown. This information was kindly supplied by the Bureau of Meteorology, Adelaide.

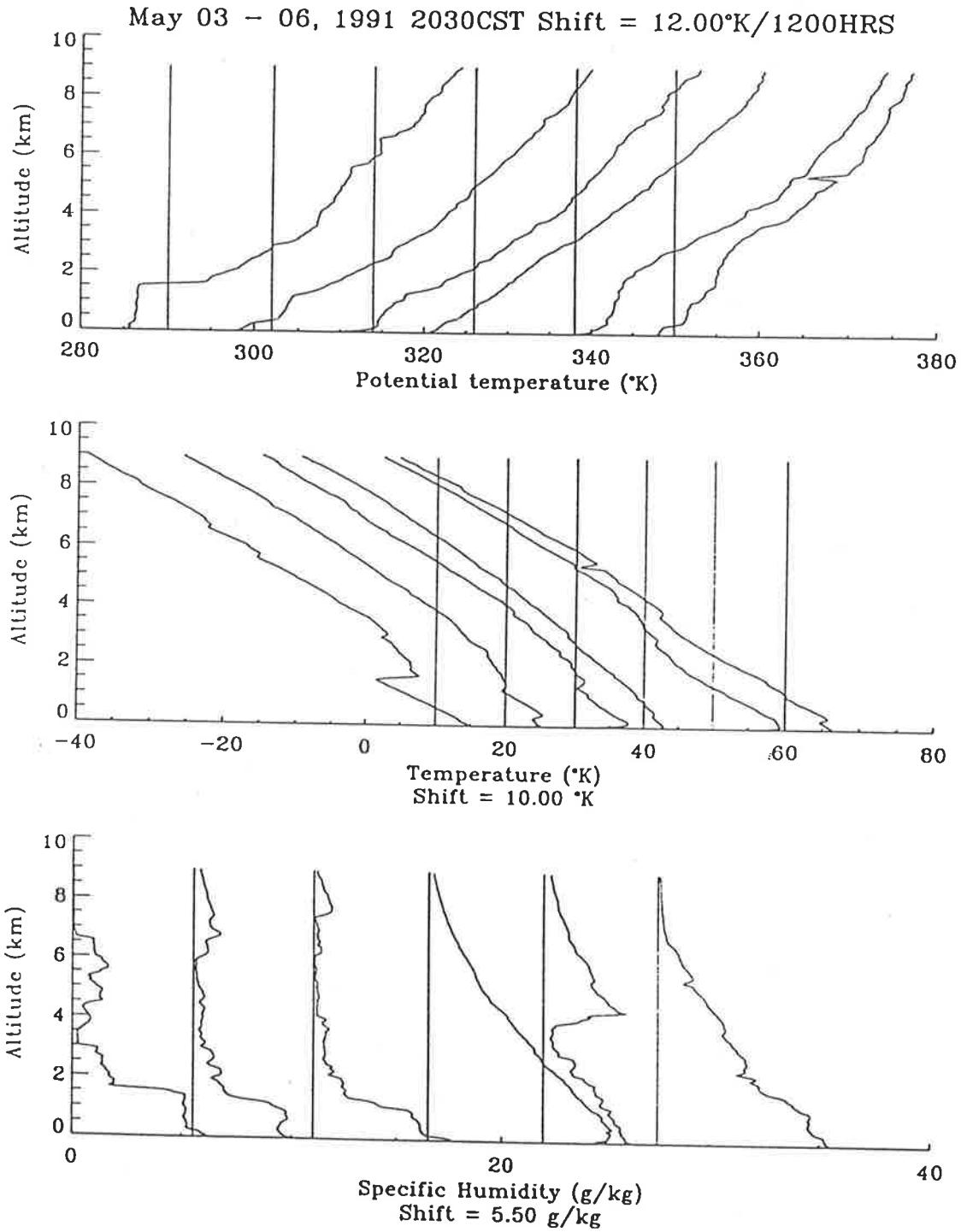

Figure 5.2: Balloon–borne radiosonde measured profiles of temperature and humidity, and the calculated potential temperature profiles are given. Each profile is right–shifted by the specified value, with a temporal displacement of 12 hours between each profile.

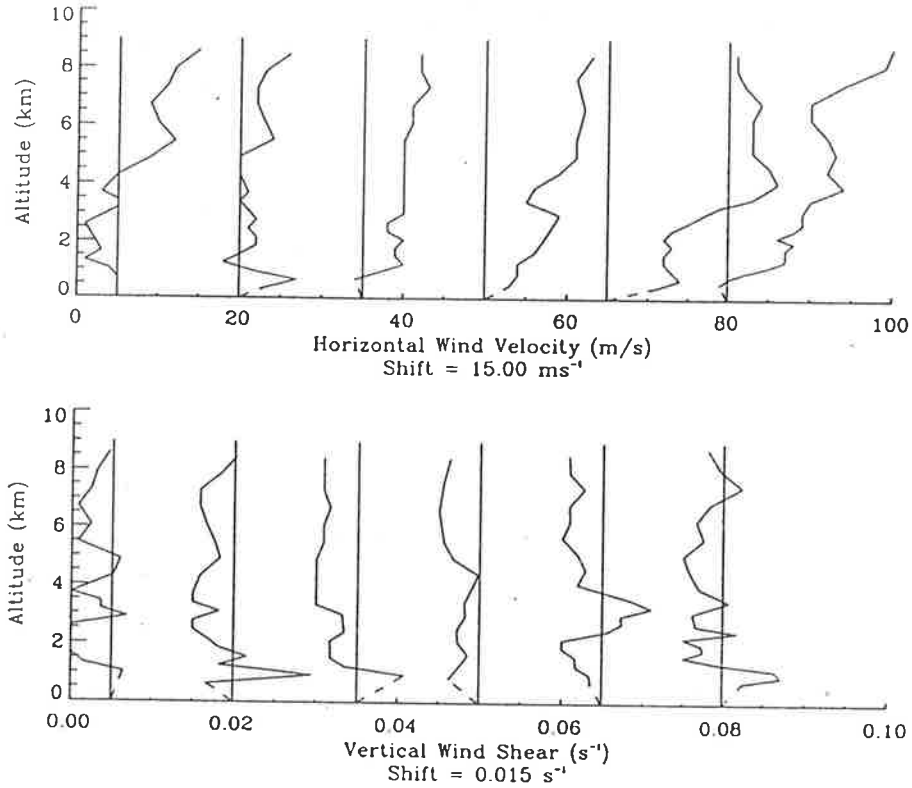

Figure 5.3: Balloon measurements of the horizontal wind speed and direction, and the calculated wind shear are shown.

cases where the correlation coefficients are very poor, those for May 4 and May 5, both at 0900 CST. As we shall see later, this may be explained in terms of the atmospheric condition existing at the time. A note of caution when interpreting results based on these correlation values: in certain cases there is an element of doubt as to the definition of 'best fit' when applying the analysis of linear regression to the data points. A 'best fit' can only be 'true' when one considers an instantaneous comparison; however, in the case of the balloon, the type of correlation would very much depend on the position of the ascending balloon relative to the radar site, and also the spatio-temporal variation of the relevant atmospheric parameters.

Table 5.1 gives the average model parameters (and constants) for both the troposphere and stratosphere, where the troposphere is defined here to be that region between heights of 2 and 8.5 km, and for the stratosphere from 11.5 to 17 km. For the tropospheric case, the fractional volume which is assumed turbulent ranges from 2.3% to 6.2%, which is within the range given by GAGE *et. al.* (1980). In addition, the calculated values for $F^{1/3}\tau_c^2$ lies between 1.5 and 1.6 (approximately), which also agrees with their estimated value of 1.5, as measured in the troposphere.

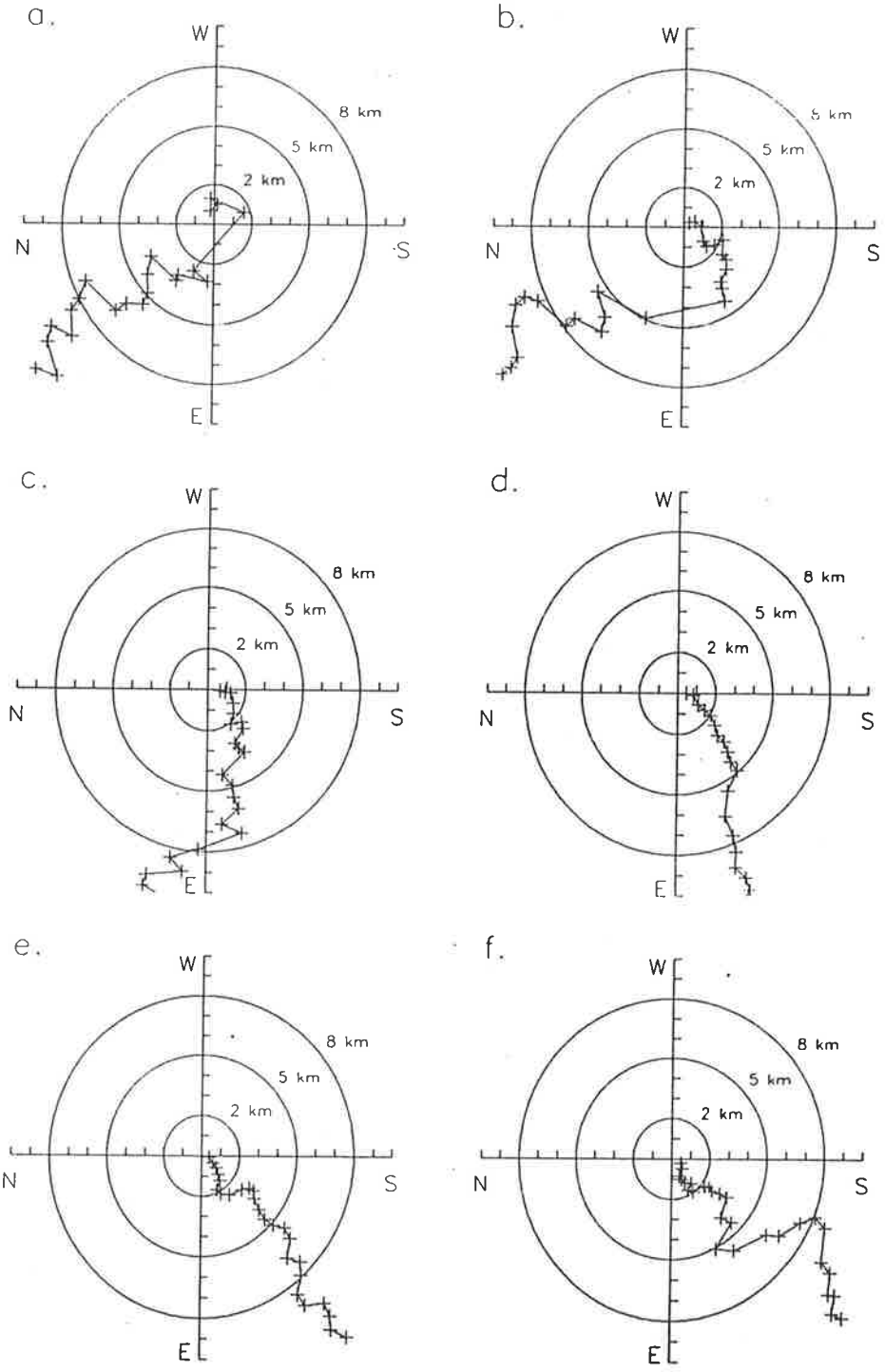

Figure 5.3 (cont.): Balloon measurements of the horizontal wind speed and direction, and the calculated wind shear are shown.

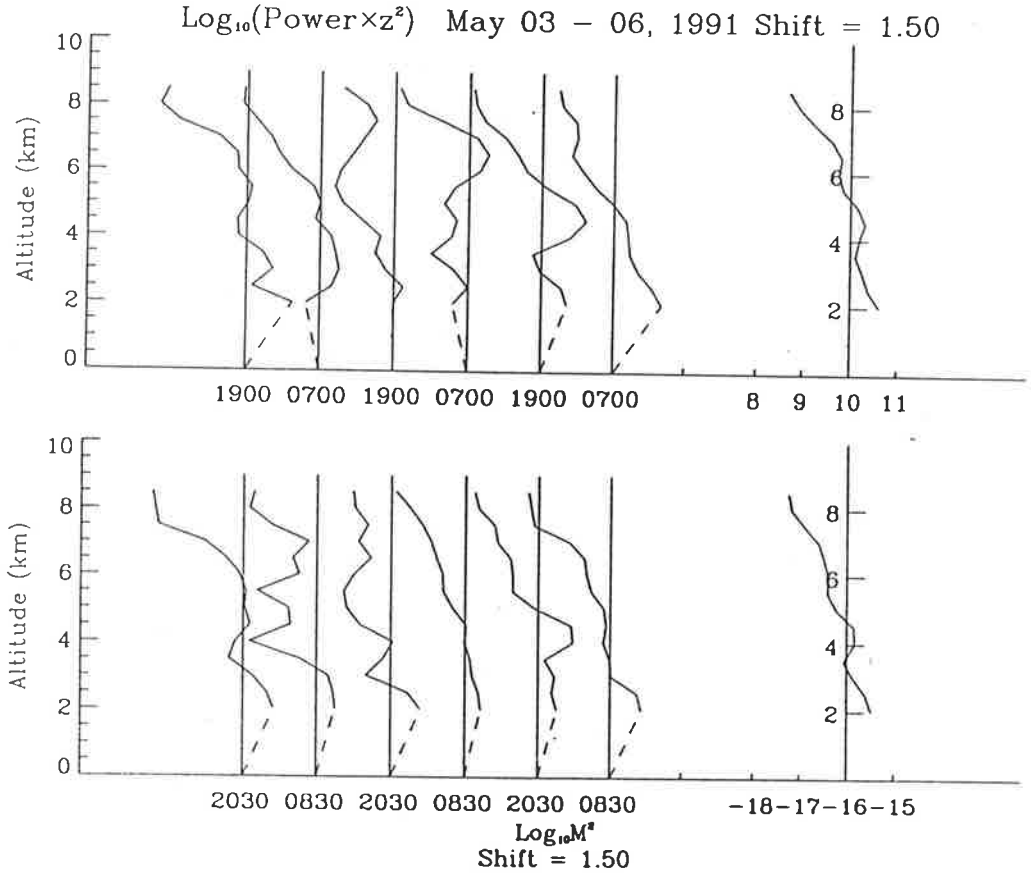

Figure 5.4: Profiles of echo power and M^2 for May 03–06.

Date/Time	*Troposphere*				*Stratosphere*			
	$\overline{s}$	F	$F^{1/3}\tau_c^2$	C_t	$\overline{s}$	F	$F^{1/3}\tau_c^2$	C_s
3 May, 2100CST	2.86	0.0371	1.5658	1.4042	2.87	0.0063	1.4275	0.4780
4 May, 0900CST	2.79	0.0303	1.5734	1.4695	2.48	0.0053	1.3912	0.5506
2100CST	1.95	0.0295	1.5191	1.3432	4.09	0.1148	1.2990	0.3596
5 May, 0900CST	2.25	0.0228	1.5431	1.3931	7.52	0.0079	1.7093	0.4958
2100CST	3.26	0.0300	1.6140	1.4353	7.28	0.0101	1.7256	0.3648
6 May, 0900CST	3.90	0.0620	1.5847	1.3792	5.08	0.0120	1.6006	0.4026

Table 5.1: Calculated mean vertical wind shears $\overline{s}$ (10^{-3} s^{-1}), the fraction of the radar volume which is turbulent F, model parameter $F^{1/3}\tau_c^2$ and the model constants C_t and C_s (in units of 10^{22}) are given for both the troposphere and stratosphere.

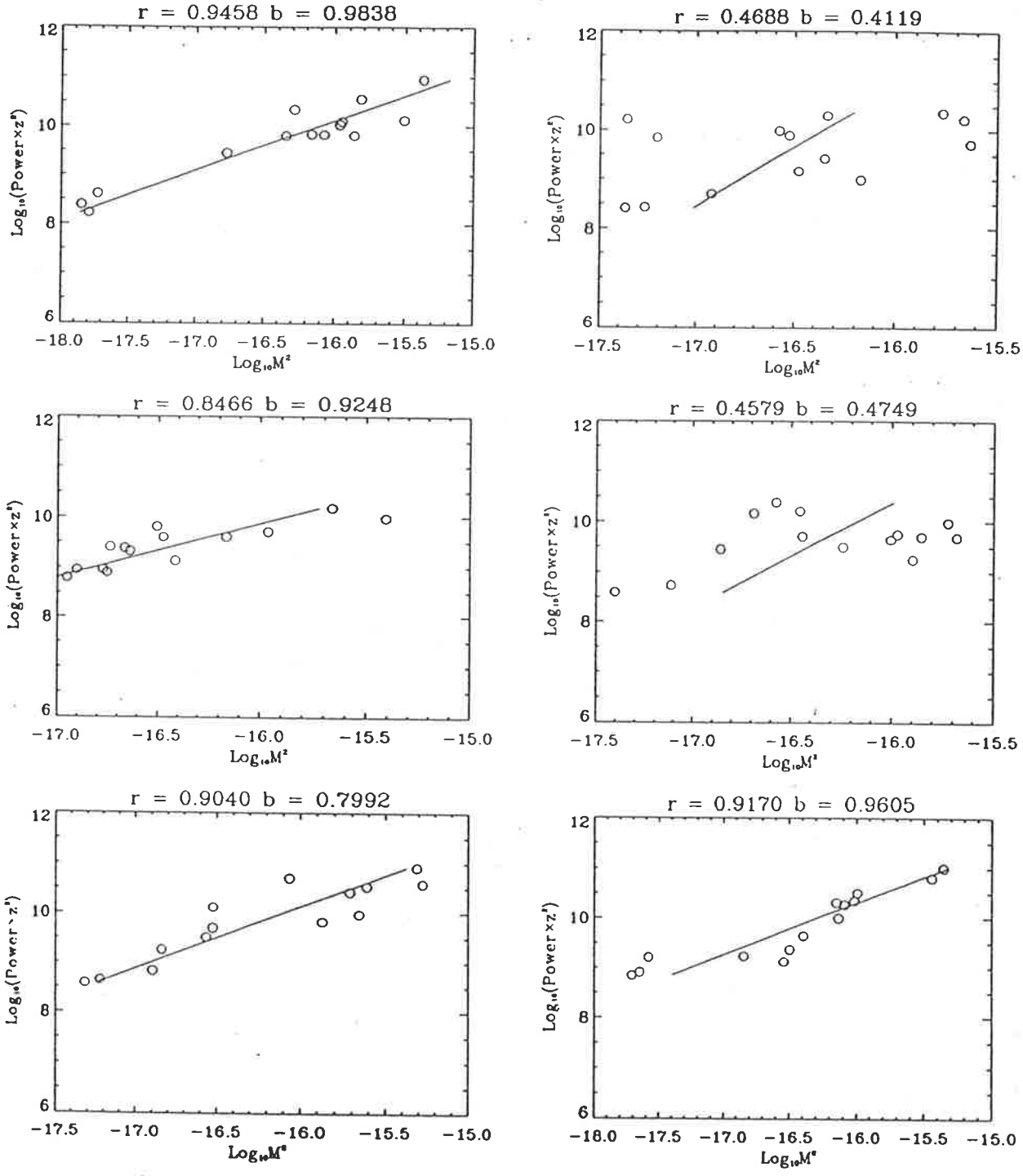

Figure 5.5: From left to right (and from top to bottom), respectively, are shown the scatter diagrams of echo power with M^2 for May 3 to May 6.

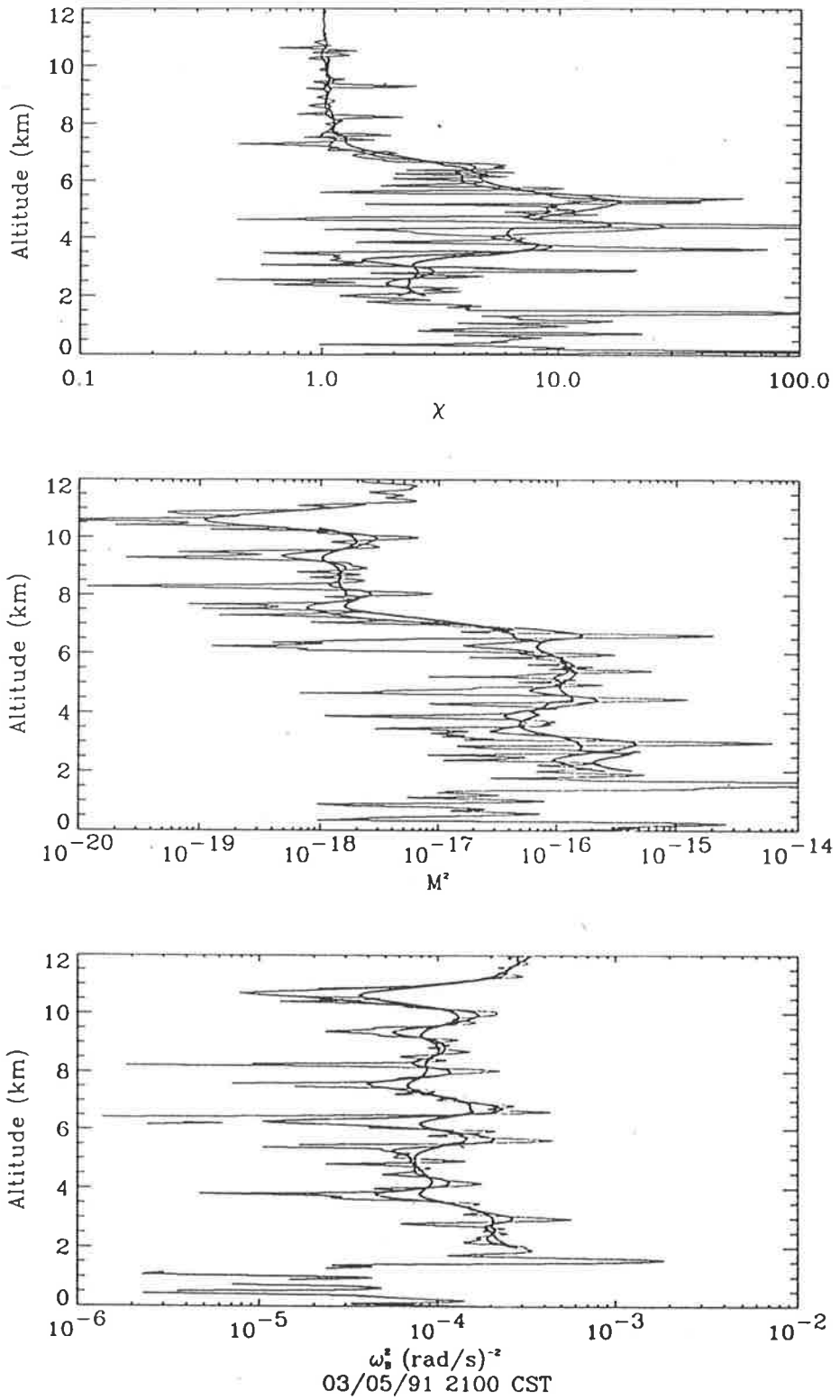

Figure 5.6: Height profiles of $\omega_B{}^2$, M^2, and the correction term, χ for May 3, 0900 CST — see text for more details.

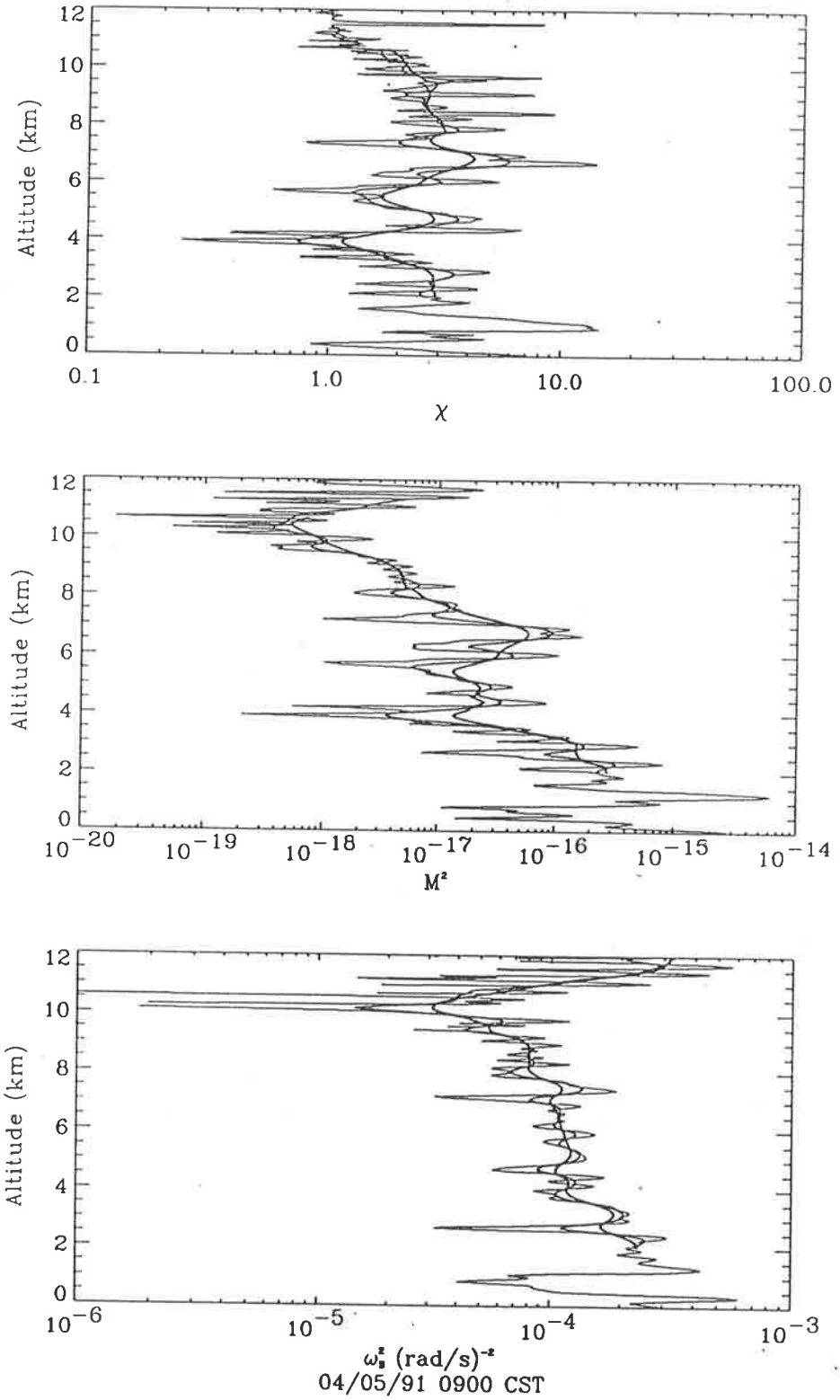

Figure 5.7: As for Figure 5.6, but for May 4, 0900 CST.

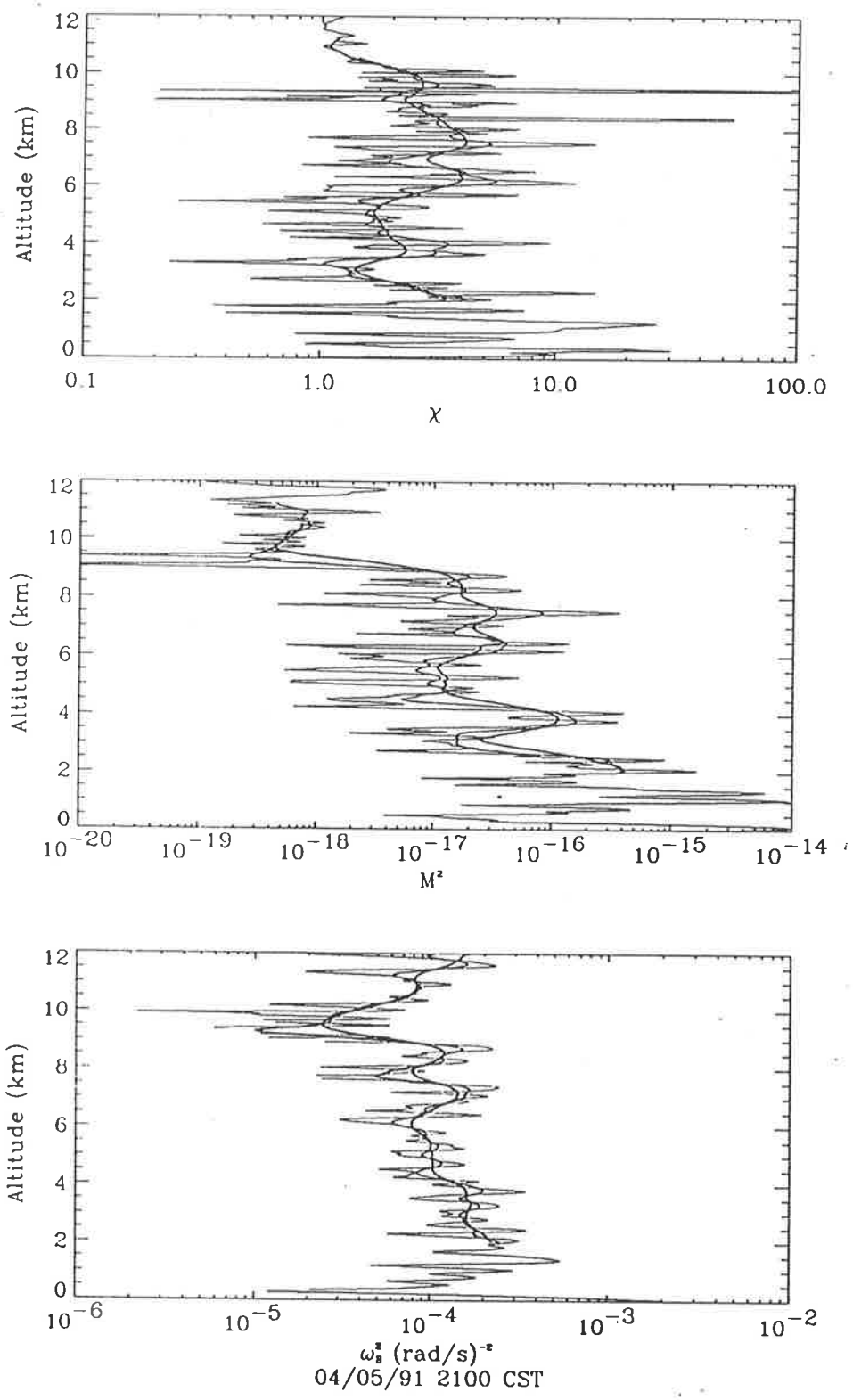

Figure 5.8: As for Figure 5.6, but for May 4, 2100 CST.

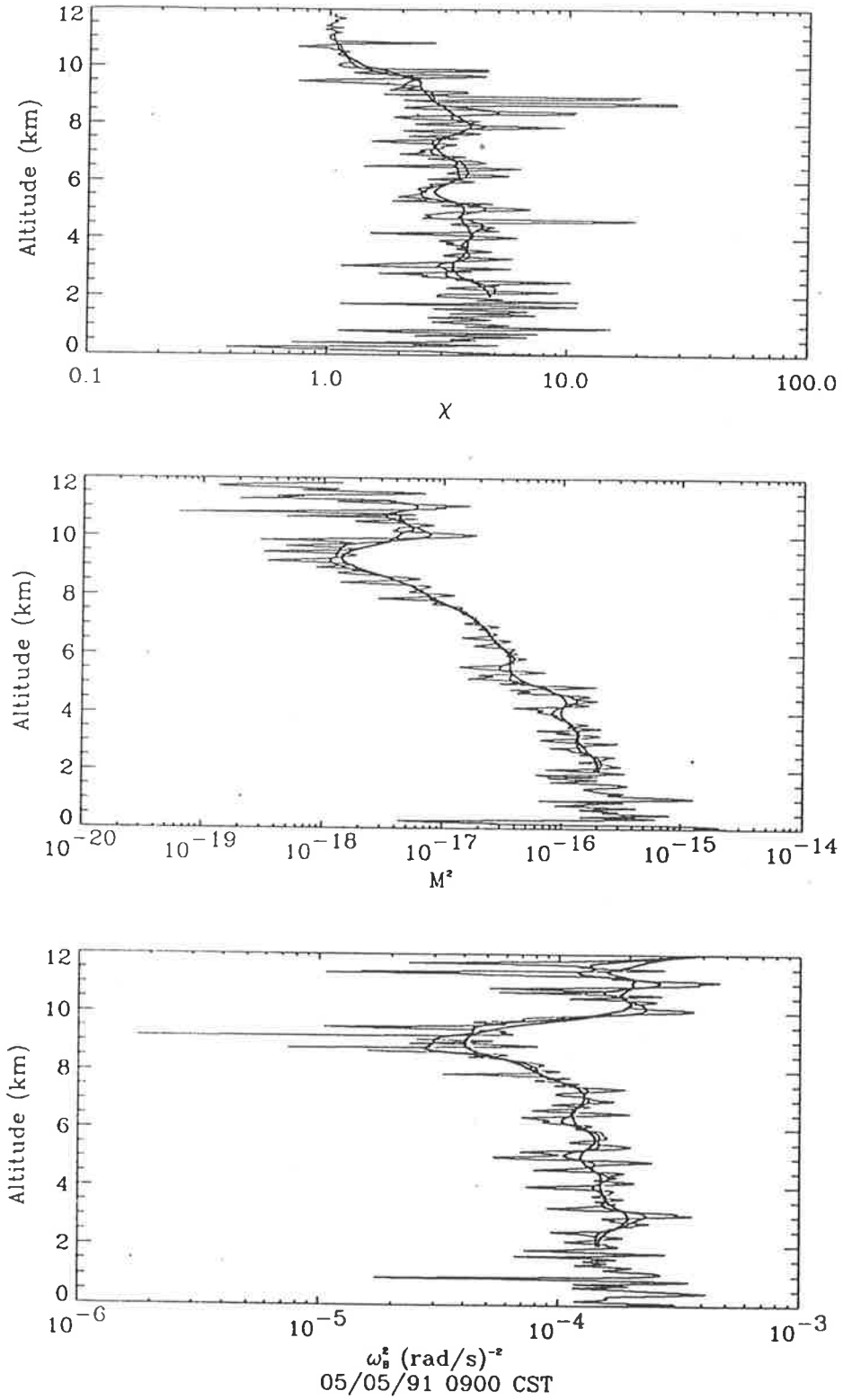

Figure 5.9: As for Figure 5.6, but for May 5, 0900 CST.

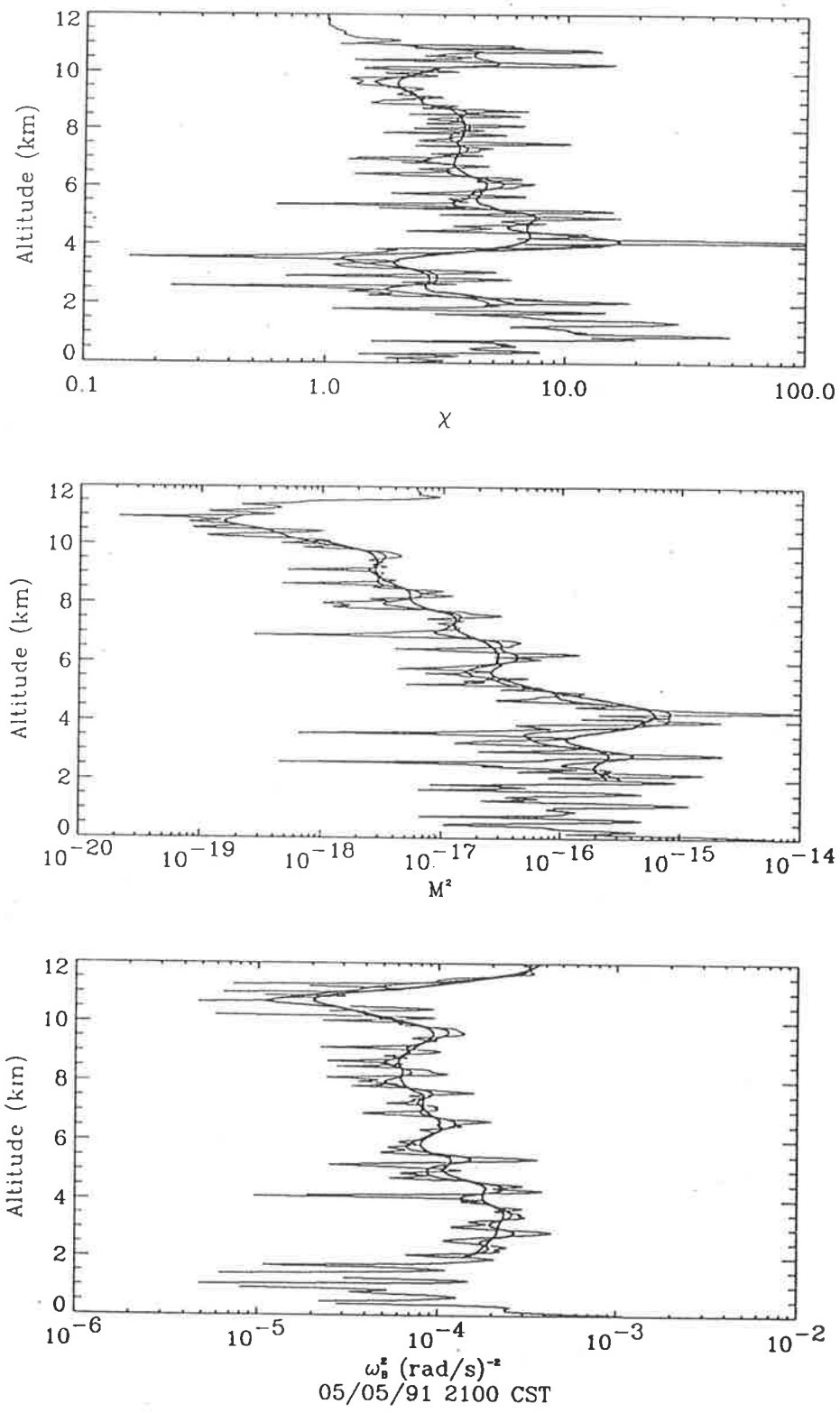

Figure 5.10: As for Figure 5.6, but for May 5, 2100 CST.

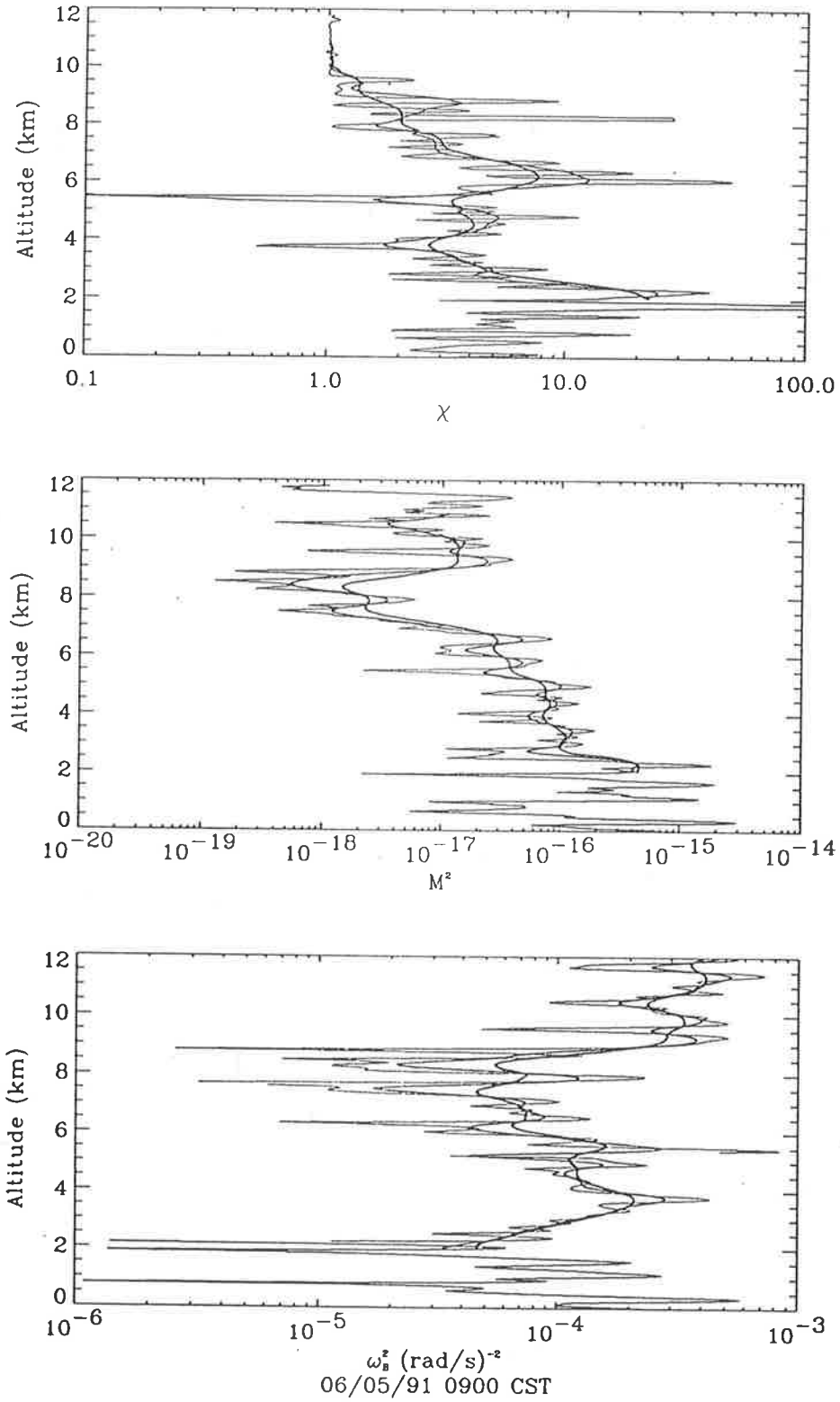

Figure 5.11: As for Figure 5.6, but for May 6, 0900 CST.

Profiles of the square of the Brunt Väisälä frequency, $\omega_B{}^2$, the gradient of the radio index of refraction, M, and the humidity correction term, χ, are given in Figures 5.6– 5.10. The different line thicknesses correspond to the different averaging and filtering which was applied to the raw data: the thinnest of the lines implies that the raw data was filtered and averaged to give interpolated values at every 10 seconds, which gives roughly about 50 m resolution; for the other two profiles, a Gaussian filter routine (codenamed NDW Filter — see Appendix G) was applied to the 50 m resolution data to give us, respectively, the 1 and 2 km resolution data.

From the $\omega_B{}^2$ profiles it is noted that the tropopause height decreases steadily from May 3 through to May 5 0900 CST at an estimated mean rate of 0.5 km per 12 hours; after that, it varies considerably over the remaining day and a half, increasing by approximately 1.5 km in the first 12 hours to May 5 2100 CST and later decreasing by about the same rate in the final 12 hours. This is clearly the result of the passage of the cold-front, and this also correlates very well with an increase in the measured horizontal wind speed, which is strongest on May 5 2100 CST due to a moderate jet stream centered at around 5 km altitude (see Figure 5.3).

In our treatment of the model parameter $F^{1/3}\omega_B{}^2$, it was assumed that this can be approximated by a constant value, which was calculated from a statistical analysis of the wind shears; however, some caution is required, because the $\omega_B{}^2$ varies considerably from one turbulence layer to another (this has been taken into account in the improved model of VANZANDT *et. al.,* 1981). This variation may be an order of magnitude or larger. The implication is this: since typical values of F can be considered to lie between 0.01 and 0.1, this implies that $F^{1/3}$ can only change by a factor of 2.2; an order of magnitude variation in $\omega_B{}^2$ would therefore mean that $\bar{\epsilon}$, which is proportional to $(F^{1/3}\omega_B{}^2)^{-3/2}$, may be incorrect by an order of magnitude. The Brunt Väisälä frequency data used in our calculations of the energy dissipation rate have been filtered and averaged to give the same resolution as the radar data; however, since turbulence occurs in thin layers with thicknesses of the order of 50 m or so (see, for example, SATO and WOODMAN (1982), BARAT and BERTIN (1984)), coupled with the fact that the radar is biased toward the layer with the greatest turbulence intensity, then it may also be necessary to be biased

toward the $\omega_B{}^2$ corresponding to this layer when performing the filtering and averaging of the data. Otherwise, the energy dissipation rate may be in error by an order of magnitude or greater.

5.3 Refractive Index Structure Constant

In this section, the average radar measured $C_n{}^2$ will be examined in more detail. There is good agreement between the humidity gradient profile (dq/dz) and the peaks in $\overline{C_n{}^2}$ with height: however, due to the different locations of the radar and the radiosonde/balloon launch site, and depending on the 'scale' and variability of the weather over the state, such a dependence may not be so obvious; this was seen in two of the six cases under consideration.

5.3.1 $\overline{C_n{}^2}$ for May 3/4, 1991

May 3, 2100 CST: the time profile of $C_n{}^2$ shows enhancements at 3, 4, 5.5, 6.5 and 7 km, all lasting for at least 4 hours (Figure 5.12), except for two heights situated at 5.5 km (enhancement from 1930–2100 CST) and 7 km (enhancement from 1900–2130 CST). All of which have contributions due to gradients in the humidity (see Figure 5.18, profile a.). The correlation between enhanced $C_n{}^2$ and the gradient in humidity has been observed to be in agreement with observations made by WARNOCK *et. al.* (1988), among others. An interesting case is that shown for heights of 6.5 to 7.5 km; here, we see a dramatic drop in the refractive index for the latter height (and the later stages of the 7 km region!), even to the extent that at this height the signal to noise ratio was at its minimum[4].

May 4, 0900 CST: this is an interesting case, because it exhibits very poor correlation between the echo power and the gradient of the radio index of refraction M^2, even though at the time the region was dominated by a high–pressure system. Considering heights of 2.5 to 4.5 km, there is no more than an order of magnitude difference in the radar measured $C_n{}^2$ between these heights (see Fugure 5.13). In contrast, the region between 5 and 7 km altitude has some three orders of magnitude difference. The large variations in

[4]This is shown by an increasing occurrence (and extent) of the broken lines and the large variability of the time profile over short time periods.

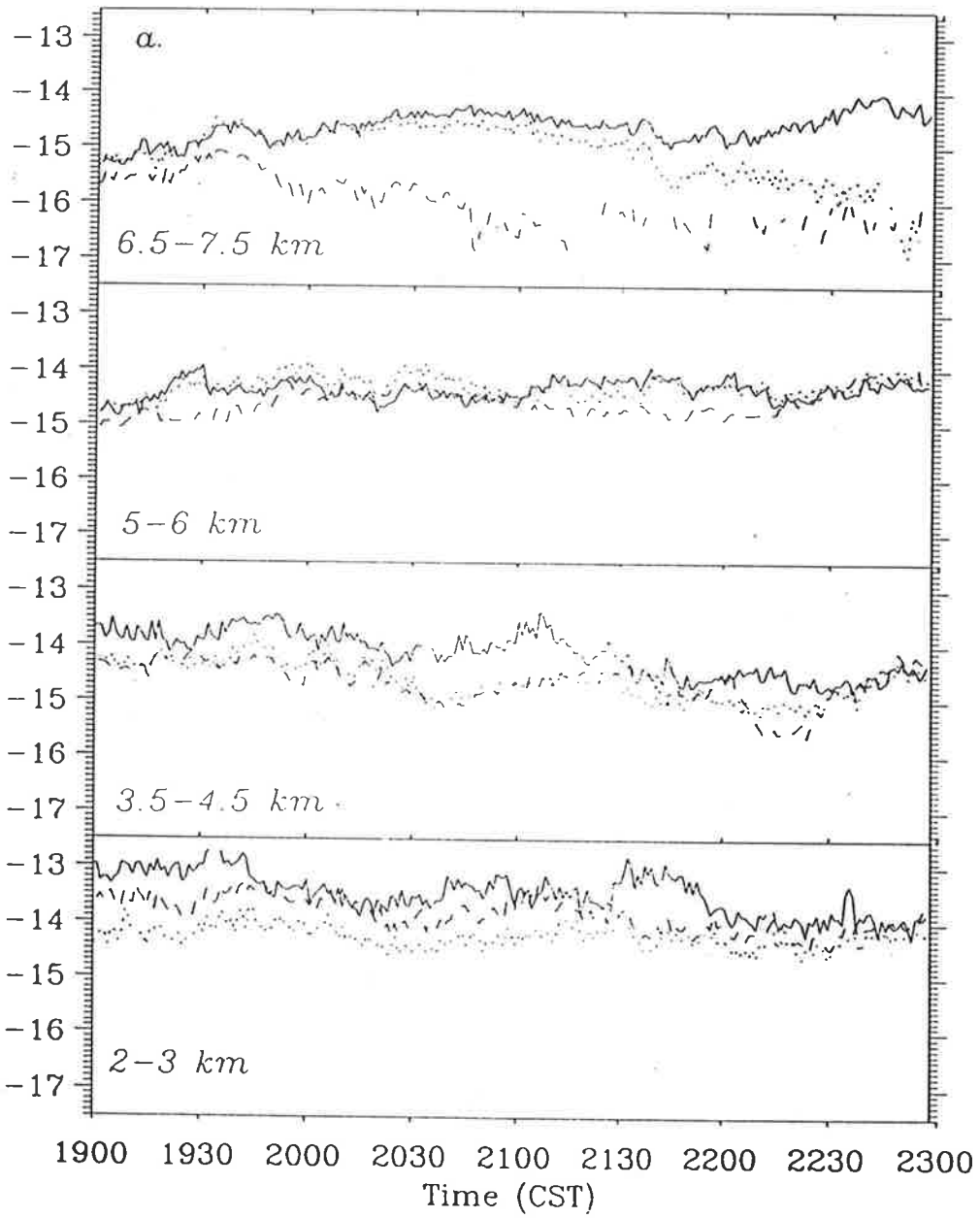

Figure 5.12: Time Profiles of radar C_n^2 ($m^{-2/3}$) with height for May 3, 0900 CST. The different linestyles represent increasing height in the following order: solid, dashed and dotted.

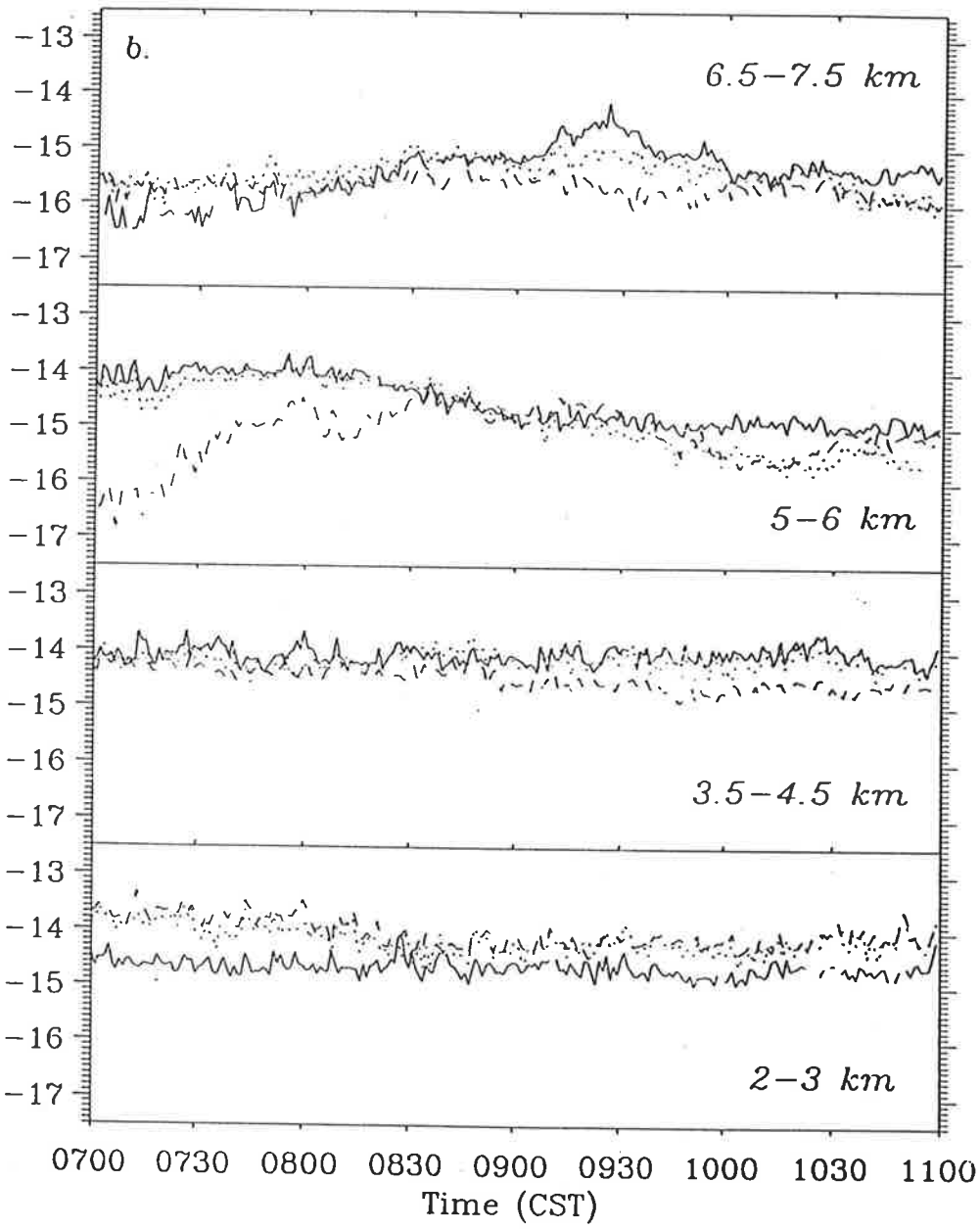

Figure 5.13: As for Figure 5.12, but for May 4, 0900 CST.

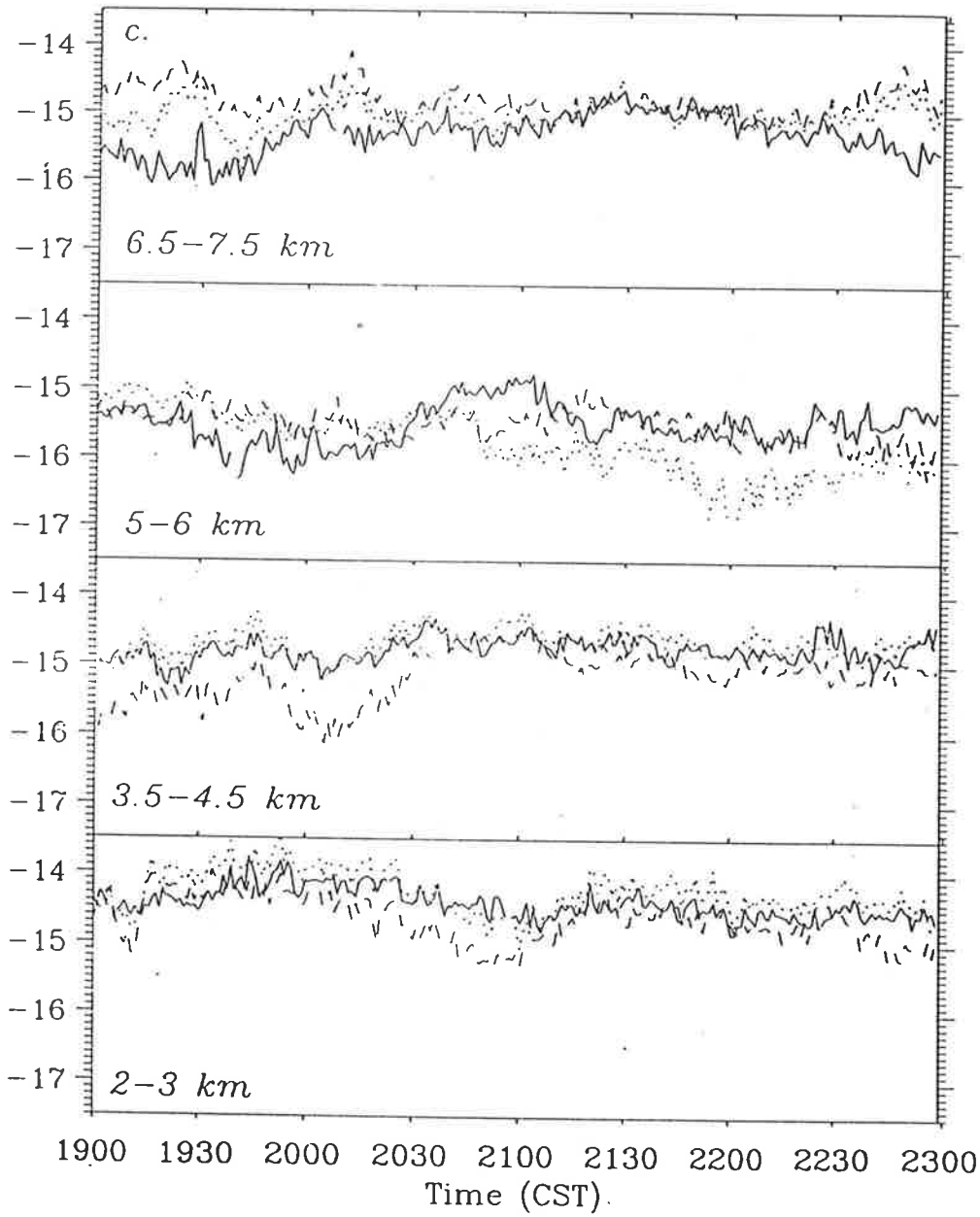

Figure 5.14: As for Figure 5.12, but for May 4, 2100 CST.

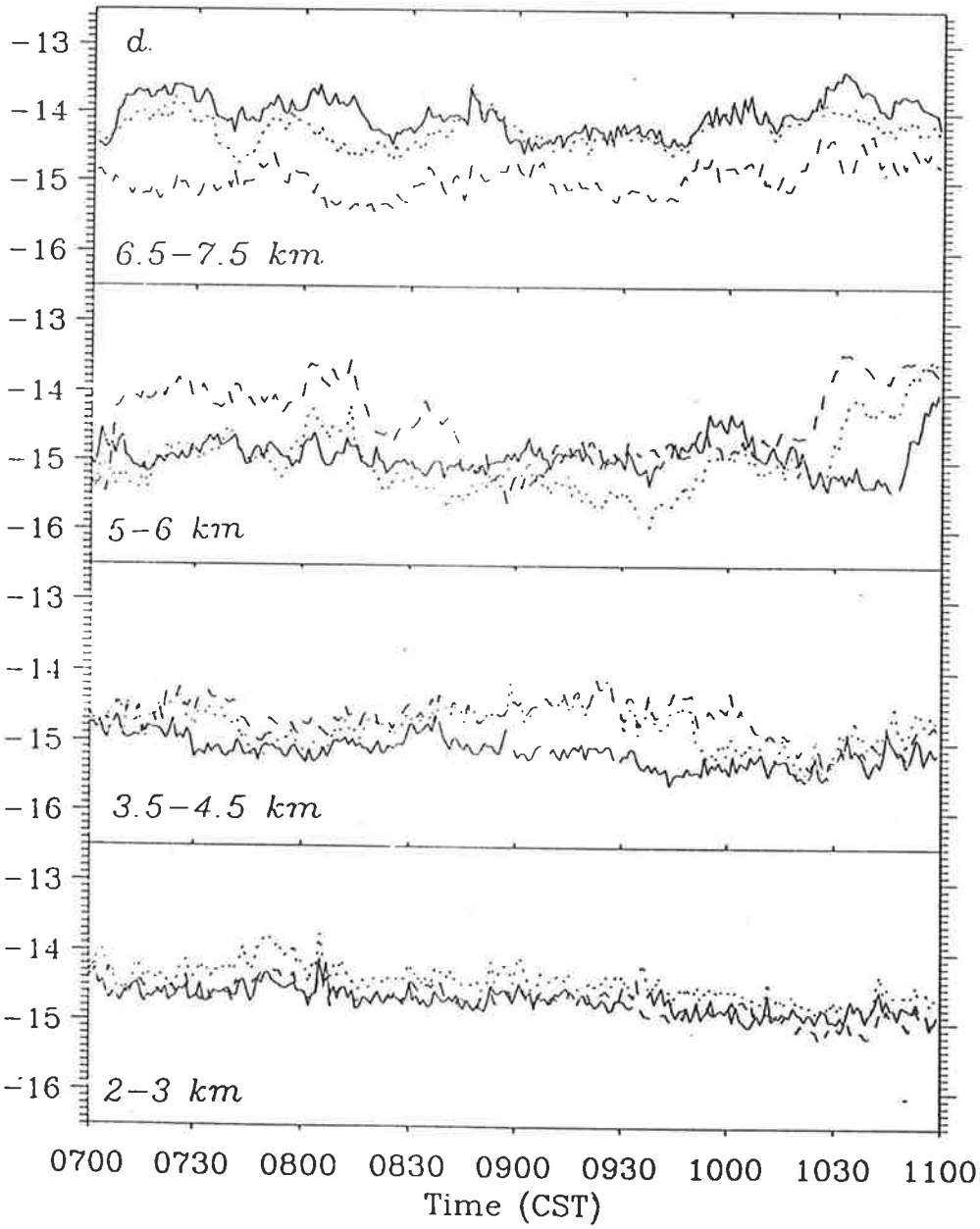

Figure 5.15: As for Figure 5.12, but for May 5, 0900 CST.

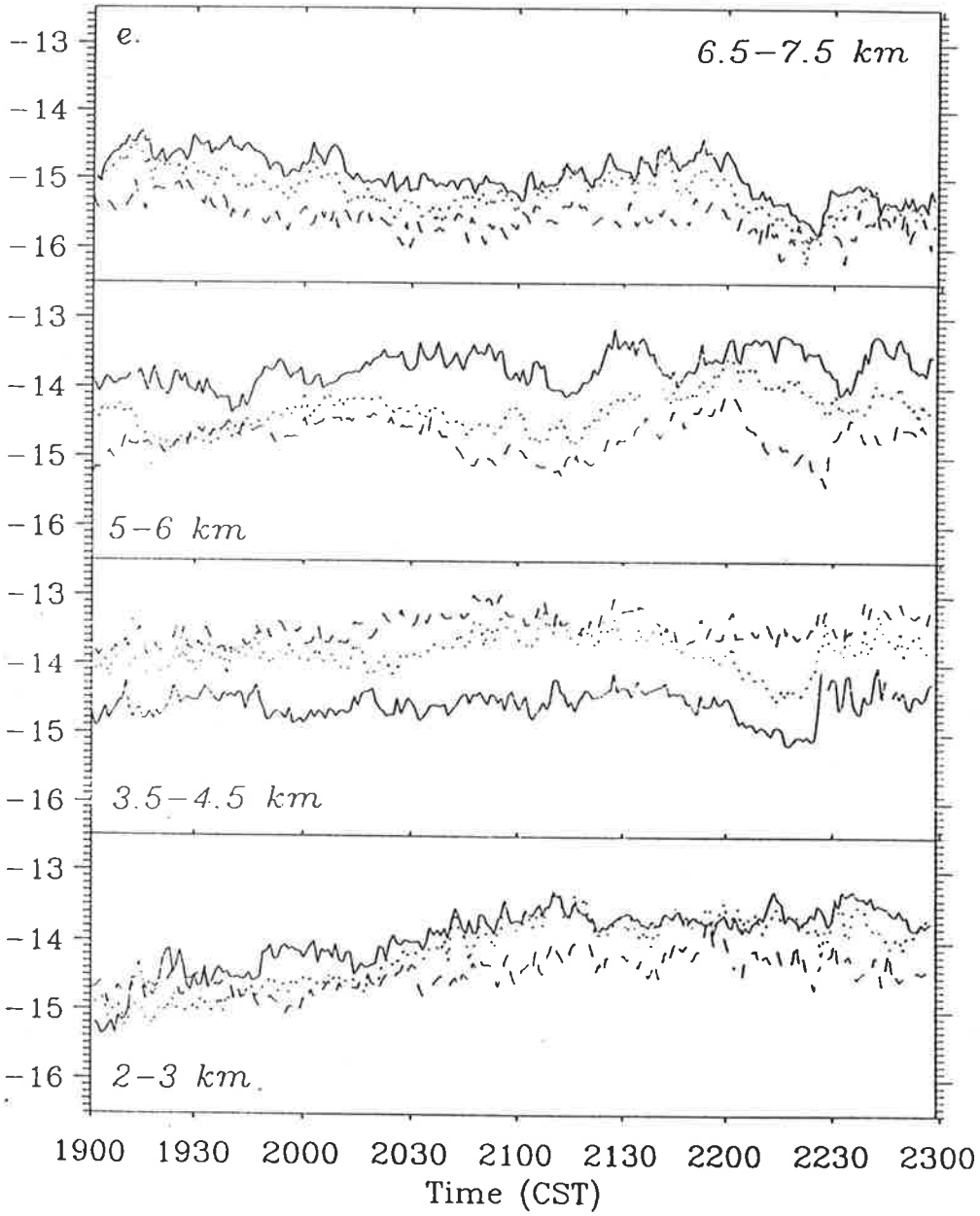

Figure 5.16: As for Figure 5.12, but for May 5, 2100 CST.

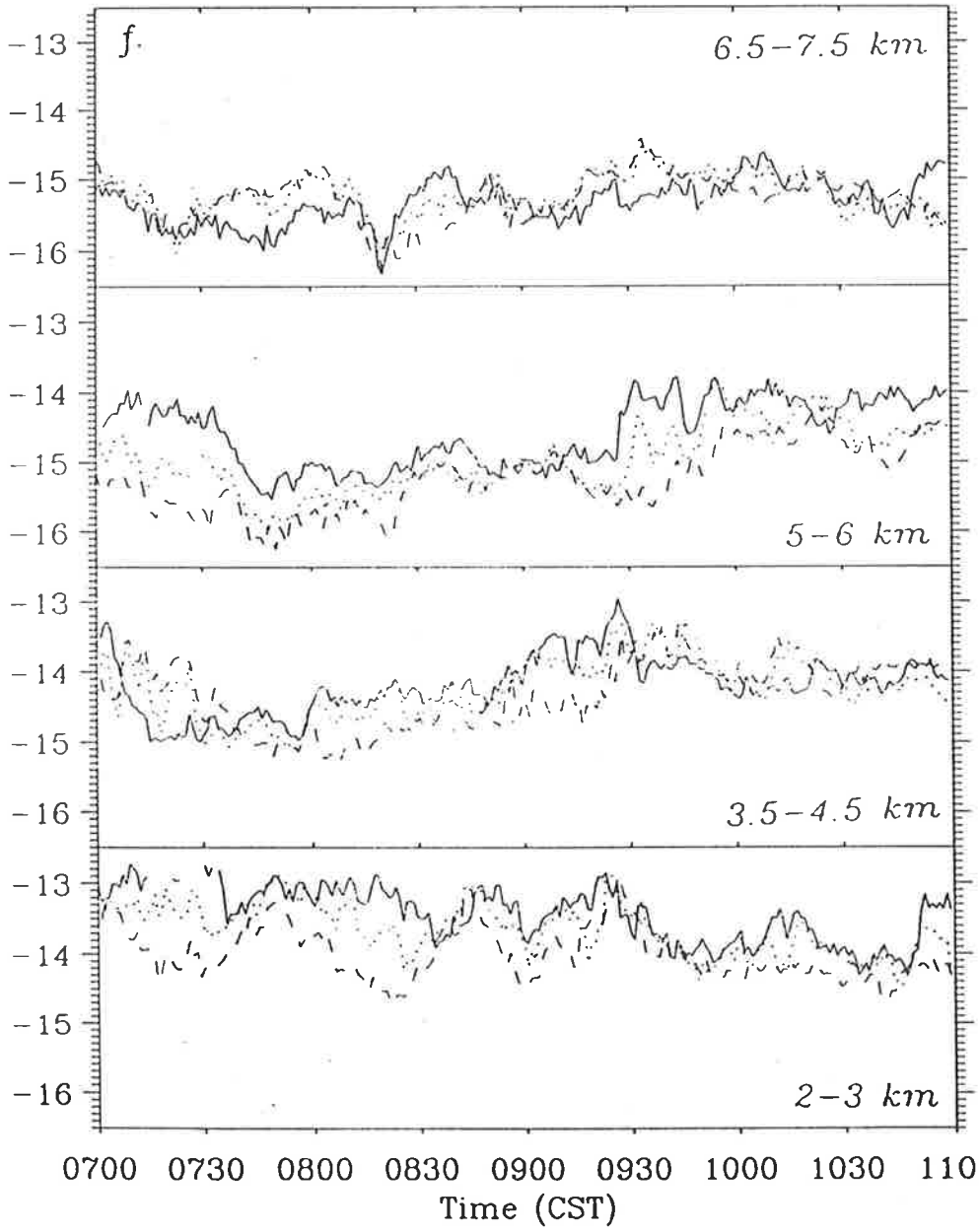

Figure 5.17: As for Figure 5.12, but for May 6, 0900 CST.

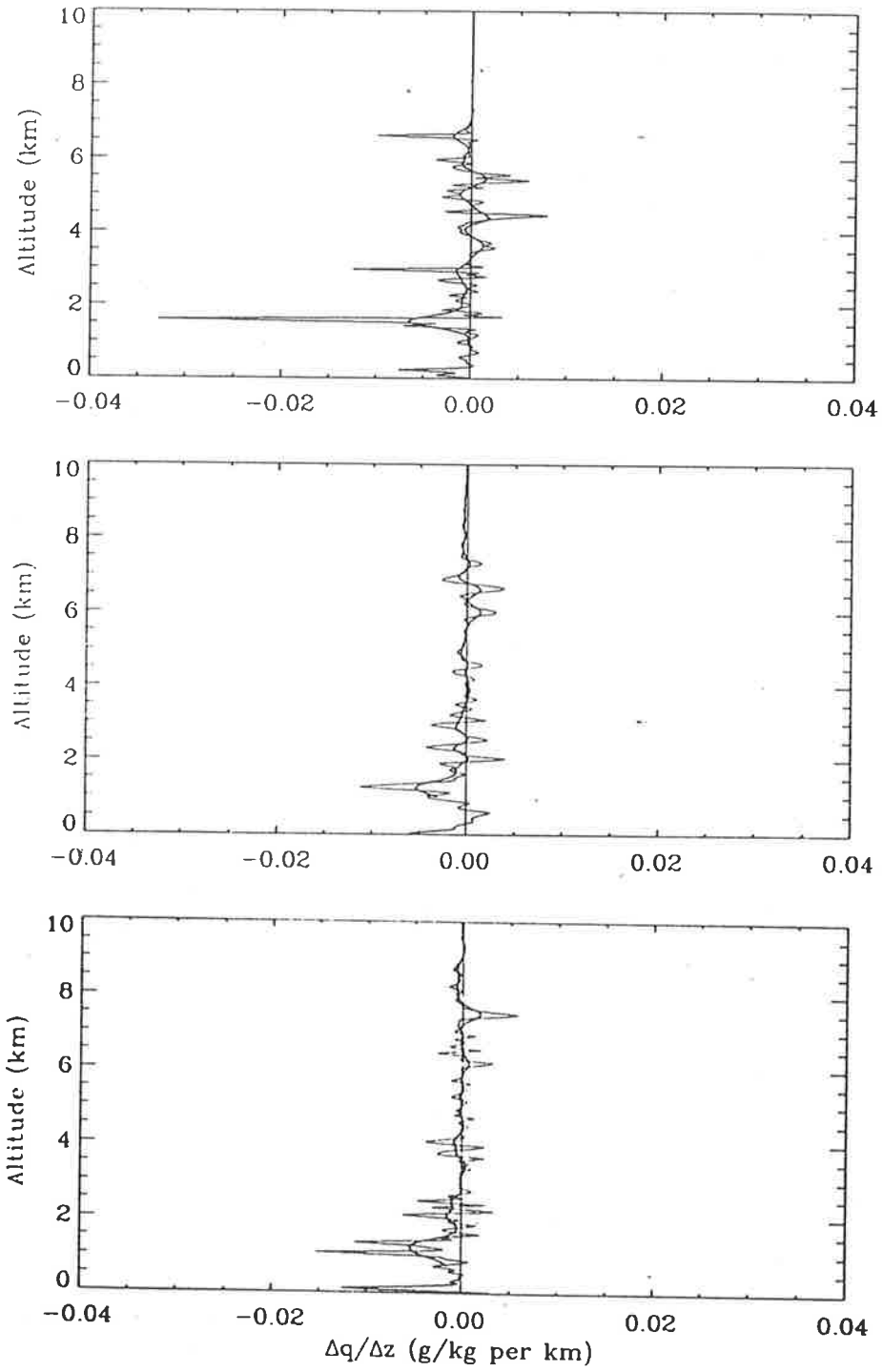

Figure 5.18: Profiles of humidity gradient in units of g/kg per kilometre for period May 3/4. The thicker line corresponds to a filtered profile with a vertical resolution of approximately 1 km.

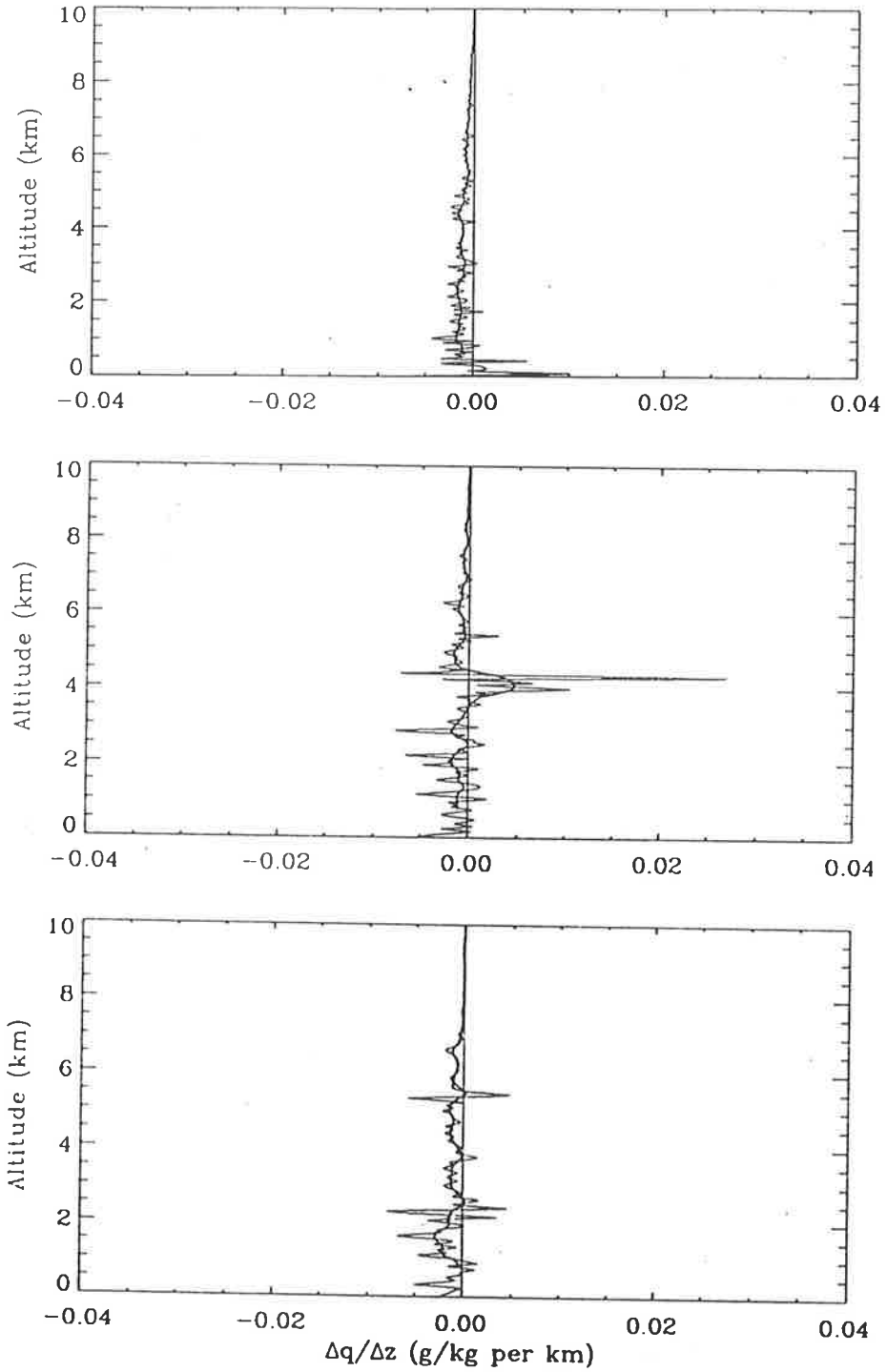

Figure 5.19: Profiles of humidity gradient in units of g/kg per kilometre for period May 5/6. The thicker line corresponds to a filtered profile with a vertical resolution of approximately 1 km.

the magnitude of C_n^2 with time within this region would mean that the atmosphere is very disturbed, with accompanying larger backscatter returns. There exist only one height at which there is an appreciable gradient in the humidity, and this is found at around 6 km (see Figure 5.18, profile b.). We may also infer from this that there was differences in the weather conditions measured at the airport as compared to the radar site, resulting in a very poor correlation between log [Power$\times z^2$] and log [M^2]. Alternatively, if the bearing of the balloon have been directed away from the radar, than this could also account for the differences in the weather conditions. Figure 5.3 shows clearly the direction of the balloon to be southerly, particularly below 4 km altitude.

May 4, 2100 CST: of note are the large enhancements of C_n^2 at heights of 2.5, 4 and from 7 to 8 km altitude (Figure 5.14), with observed humidity gradient contributions at heights of 2, 2.5, 4 and, in particular, at 7.5 km. Figure 5.18 (profile c.) shows the good agreement in contributions by the gradient in humidity for these heights. On this particular evening we have the largest variation of values of the refractive index structure constant observed for the six case studies analyzed so far: at about 8 km the measured C_n^2 was observed to be the largest, and the lowest values were observed for the 4.5 to 5.5 km height range. For the case where there exist a minimum in the measured C_n^2, one reason could well be that there was almost no contributions from the humidity gradient at these height ranges, plus the existence of a large potential temperature gradient. It is generally known that for high turbulence intensity, one generally needs the conditions of $d\theta/dz \simeq 0$ and dT/dz near the adiabatic lapse rate, that is, -9.6×10^{-3} Km^{-1} (BARAT, 1982).

5.3.2 $\overline{C_n^2}$ for May 5/6, 1991

May 5, 0900 CST: approximately an order of magnitude increase in the refractive index structure constant was observed for heights of 6 to 7 km relative to values measured at 5 (or 5.5) kilometre altitude (Figure 5.15). There is nothing in the humidity gradient/temperature (see Figures 5.19, profile (a.) and 5.2) profile to suggest a likely cause for such an occurrence. Let us turn our attention for a moment to Figure 5.9, which gives profiles of the Brunt Väisälä frequency and other meteorological parameters. In the

1 km (linestyle of medium thickness; 2 km — thick linestyle) resolution profile, we observe that there is very little variation in $\omega_B{}^2$ (ranging from 1×10^{-4} to 2×10^{-4} $(rad/s)^2$) from ground level up to a height of about 7.5 km, after which it decreases considerably to about 4×10^{-5} $(rad/s)^2$ at about 9 km. This however, does not solve the problem of the enhanced $C_n{}^2$ values between 6 and 7 km altitude!

In light of what we have just discussed, and the fact that the correlation between log [Power$\times z^2$] and log [M^2] is very poor (see Figure 5.4), one possible conclusion from this would be that there was an appreciable difference in the weather condition existing at Buckland Park compared to that at Adelaide airport, since the sites are separated by a distance of about 35 km. This is a distinct possibility, because at about this time, a transition period from a high–dominated condition to a low–dominated one was in effect, that is, neither the high nor the low was dominant during this transition period. Another possible explanation is that the balloon have been blowing away from the radar, that is, in a southerly direction. At first glance, the wind direction profile agrees with this view (see Figure 5.3); however, it is to be noted also that similar profiles exist for (e) and (f), and yet these tend to have very good correlations. The enhanced region at 6 to 7 km altitude can be explained in terms of large humidity gradients existing at Buckland Park, but was not present at Adelaide airport, where the radiosondes were launched. This is evident when we study the humidity gradient profile and observe that it actually decreases approximately linearly with height.

May 5, 2100 CST: there is a large increase in humidity from about 4 to 5 km altitude which is not related to a temperature inversion (see Figure 5.2). Time profiles of $C_n{}^2$ for this case shows the refractive index structure constant peaking at about 4.5 km, which is just above the region of the maximum humidity gradient layer (at 4 km — c.f. Figure 5.19, profile (b.) and 5.16). This discrepancy of 500 m is yet to be explained; nevertheless, it is an interesting result, due to the remarkable correlation between the power and M^2 profiles.

May 6, 0900 CST: there is a temperature inversion at about the 5.5 km region, and a maximum humidity gradient at 5 km (Figures 5.2, 5.19, profile (c.)). Below the 3 km region the $C_n{}^2$ values are relatively large (Figure 5.11, but here the atmosphere is

considerably more unstable, as shown by the $\omega_B{}^2$ profile. What we have here is decreasing $C_n{}^2$ measurements with height, except for some local enhancements and for heights above 6 km. The correlation between range–squared corrected power and M^2 is also very good.

5.3.3 Turbulence Outerscale, L_0

Figure 5.20 gives the histogram plots for the outerscale of turbulence L_0 for each of the cases already studied. In most cases, the most frequent occurrence of L_0 is at a value less than about 10 metres, or less than about 250 metres for L_B , where the buoyancy range L_B is approximately given as $L_0 = 0.035 L_B$ (HOCKING, 1985). Refer to Appendix A for a definition of L_B. This value for L_0 is in good agreement with that used by VANZANDT *et. al.* (1978) to infer $C_n{}^2$ values from model calculations; however, it is necessary to exercise great caution in using a typical value for L_0, as it is clearly evident from the height profile that the outerscales do vary considerably with time and with height (see Figure 5.21).

Comparing profiles of the mean outerscales for the six cases, we have almost similar profiles for the evening conditions, while those shown for the morning conditions have considerably larger L_0, which can be very large in some cases, as a result of severe turbulence. In addition, we observe a much larger variation in L_0 for the period May 6, in particular below the 6.5 km height region.

5.4 Energy Dissipation Rate

In categorizing the $\bar{\epsilon}$ values, VINNICHENKO and DUTTON (1969) considered their energy dissipation rate values as falling within the four categories (as generally reported on the basis of reactions of aircraft encountering the turbulence) which they termed 'no', 'light', 'moderate' or 'severe' turbulence, according to the values specified in Table 5.2. In the same year TROUT and PANOFSKY (1969), using the geometric mean values of measured energy dissipation rates from different sources[5], associated 'no', 'light', 'moderate' and 'severe' turbulence with $\bar{\epsilon}$ of 1.5, 30, 85, and 675 cm^2s^{-3}, respectively. The uncertainty estimated for the latter three turbulence classes was thought to be in error by as much as 50%, and a much greater uncertainty exists for the 'no' turbulence class.

[5] All these measurements of $\bar{\epsilon}$ were made using clear–air turbulence spectra.

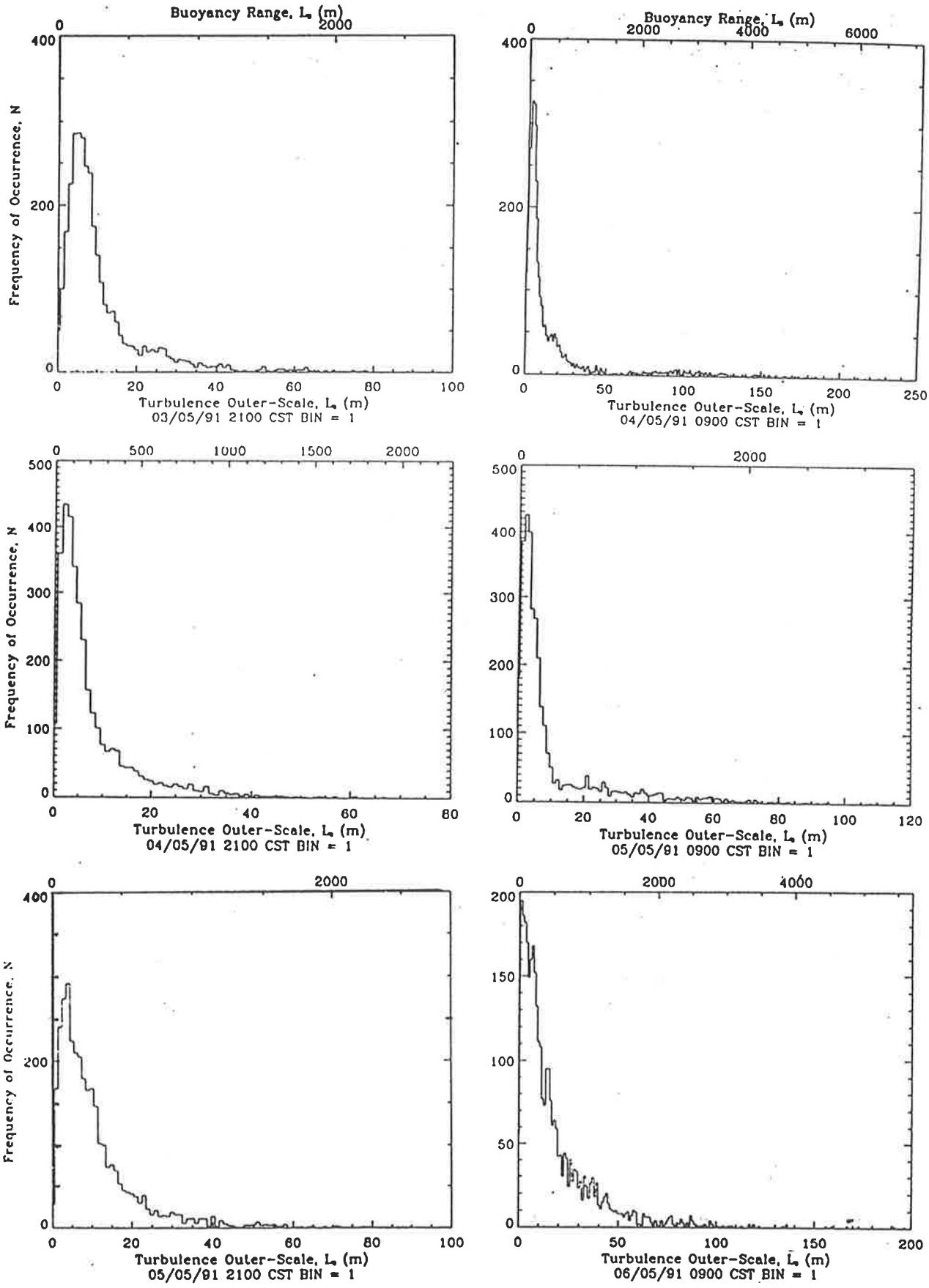

Figure 5.20: Histogram plots of L_0 ($L_B \approx L_0/3.5\times10^{-2}$) for the period May 03–06. The L_0 was determined directly from the radar measured C_n^2 values.

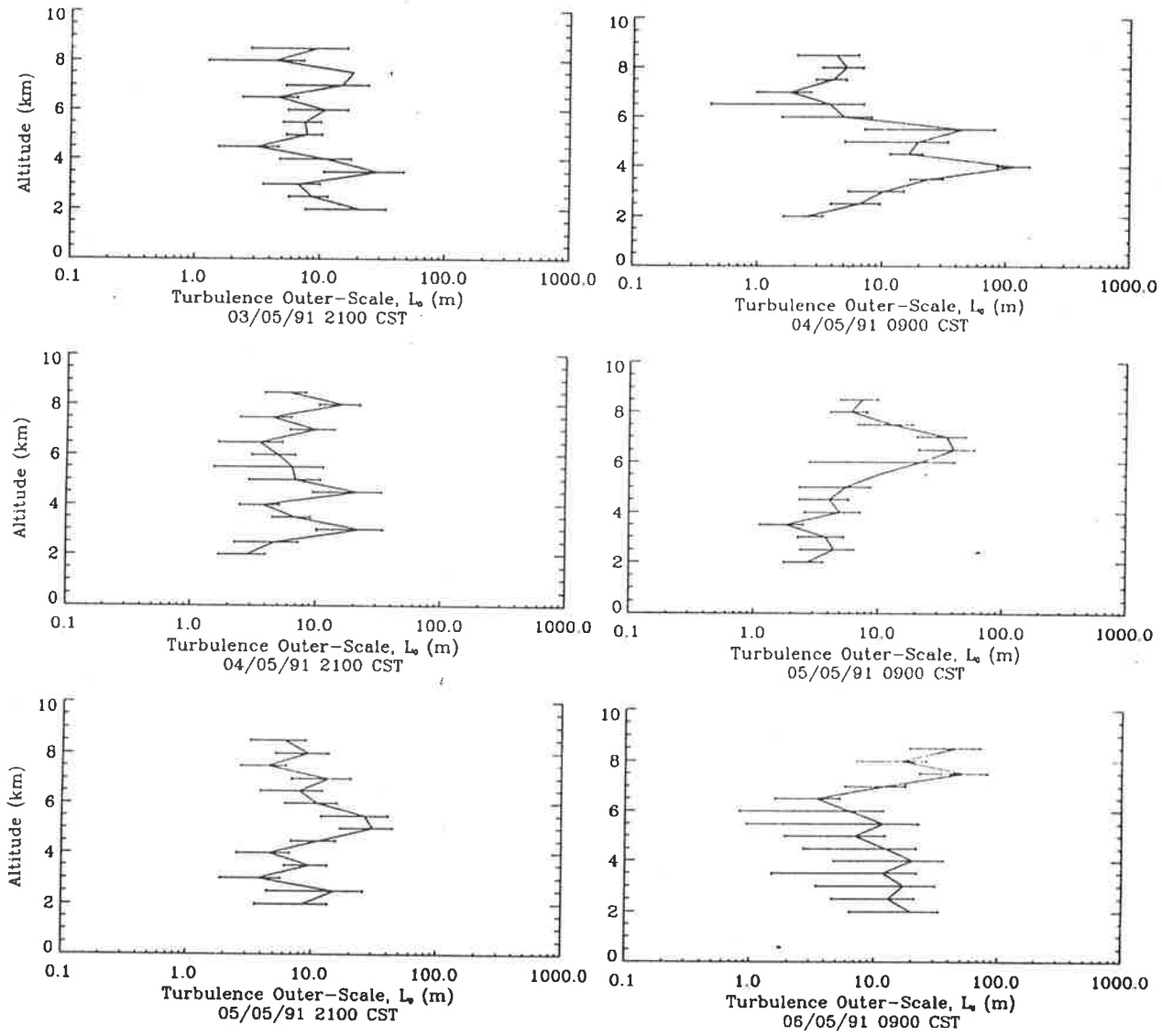

Figure 5.21: The mean of the turbulence outerscales is plotted with height, where the error bars represent the one standard deviation values.

Category	$\bar{\epsilon}$ $(cm^2 s^{-3})$
no turbulence	< 30
light turbulence	> 30 and < 120
moderate turbulence	> 120 and < 1000
severe turbulence	> 1000

Table 5.2: Approximate range of turbulence intensities as categorised by Vinnichenko and Dutton, 1969.

As we consider the following situations with respect to $\bar{\epsilon}$ measurements, let us state again the form of the equation which was used:

$$\bar{\epsilon} = 3.5 \times 10^{15} \left(\frac{T}{P}\right)^3 \left(\frac{\overline{C_n^2}}{F^{1/3}\omega_B{}^2}\right)^{3/2} \chi^{-3} \tag{5.1}$$

where χ is the 'wet' term and is given by the expression (see Equation 2.57)

$$\chi = \left[1 + \frac{15500q}{T}\left(1 - \frac{1}{2}\frac{\partial lnq/\partial z}{\partial ln\theta/\partial z}\right)\right] \tag{5.2}$$

To calculate this expression, we used the balloon data from Adelaide airport, which is approximately 35 km north of the radar site.

5.4.1 $\bar{\epsilon}$ for May 3/4, 1991

To help with the discussion, Figures 5.22 to 5.27 presents some results of the energy dissipation rates in units of $cm^2 s^{-3}$ for the period May 3/4, 1991. In each figure, the first plot contains the height profiles of the corrected (unfilled circles) and uncorrected (filled circles with error bars) energy dissipation rate per unit mass averaged over four hours: the error bars represent the upper and lower decile points. The second plot gives the time–log–height profiles of the mean energy dissipation rate per unit mass in units of $m^2\ s^{-3}$, averaged over N minutes and shifted from one another by the specified value. The average over the whole period is given at the end of the profile, which also shows the value at which each preceeding profile are centered. A contour plot of the humidity–corrected $\bar{\epsilon}$ is given in the final plot.

May 3, 2100 CST: on this particular evening, there was some moderately strong vertical wind shears measured at the airport, peaking at heights of 3.5, 4.5 and 5 km (see Figure 5.3). Turning to the contour plot for the humidity–corrected energy dissipation

rate per unit mass (Figure 5.22), there exists some moderate turbulence at heights between 2.5 to 4.5 km, and from approximately 5 to 6 km. As shown, the moderate turbulence occurs in short bursts at higher altitudes and in much longer bursts at lower heights. As a result of the high–pressure system dominating this period, and the fact that the moderate turbulence occurred at heights where relatively large wind shears ($\approx 1.6\times10^{-2}$ s^{-1}) exist, one may arrive at the conclusion that such turbulence was wind shear induced.

May 4, 0900 CST: this is one example where severe turbulence was detected for a considerably long period of time (see Figures 5.23). Such category of turbulence is seen to occur at the 3 to 4 km height region, with a relatively short burst centered at about 5 km altitude. Height profiles of the horizontal wind speed and the respective wind shear do not show any case for wind shear induced turbulence — at least there was none detected at the airport site! However, it has already been pointed out in our discussion on the refractive index structure constant that, on this particular occasion, there was some evidence to suggest that the atmospheric parameters measured by the balloon was considerably different to that existing above the radar site. The very small humidity correction term χ (correction factor between 1 and 2, see Figure 5.7) at these heights coupled with the large scattered power received from these heights produces the observed values for the corrected $\bar{\epsilon}$. One other point to note from this case is the large variation in the average energy disspation rate at the 5.5 km height, compared to the one at the 3 to 4 km height region.

May 4, 2100 CST: in this case, there is some moderate turbulence detected below 4.5 km (Figure 5.24); an interesting situation arises from 2030 to about 2130 CST, where it seems as though the turbulence was 'lifted up' by about 1 km above its present position to a higher height and then decreases back to its normal position. Whatever the interpretation, it is not possible to associate this event with any possible causes, because of the limited information which is available to us.

5.4.2 $\bar{\epsilon}$ for May 5/6, 1991

May 5, 0900 CST: this is another case where a poor correlation exist between log of Power$\times z^2$ and M^2 (see Figure 5.5). The humidity gradient profile shows a small and

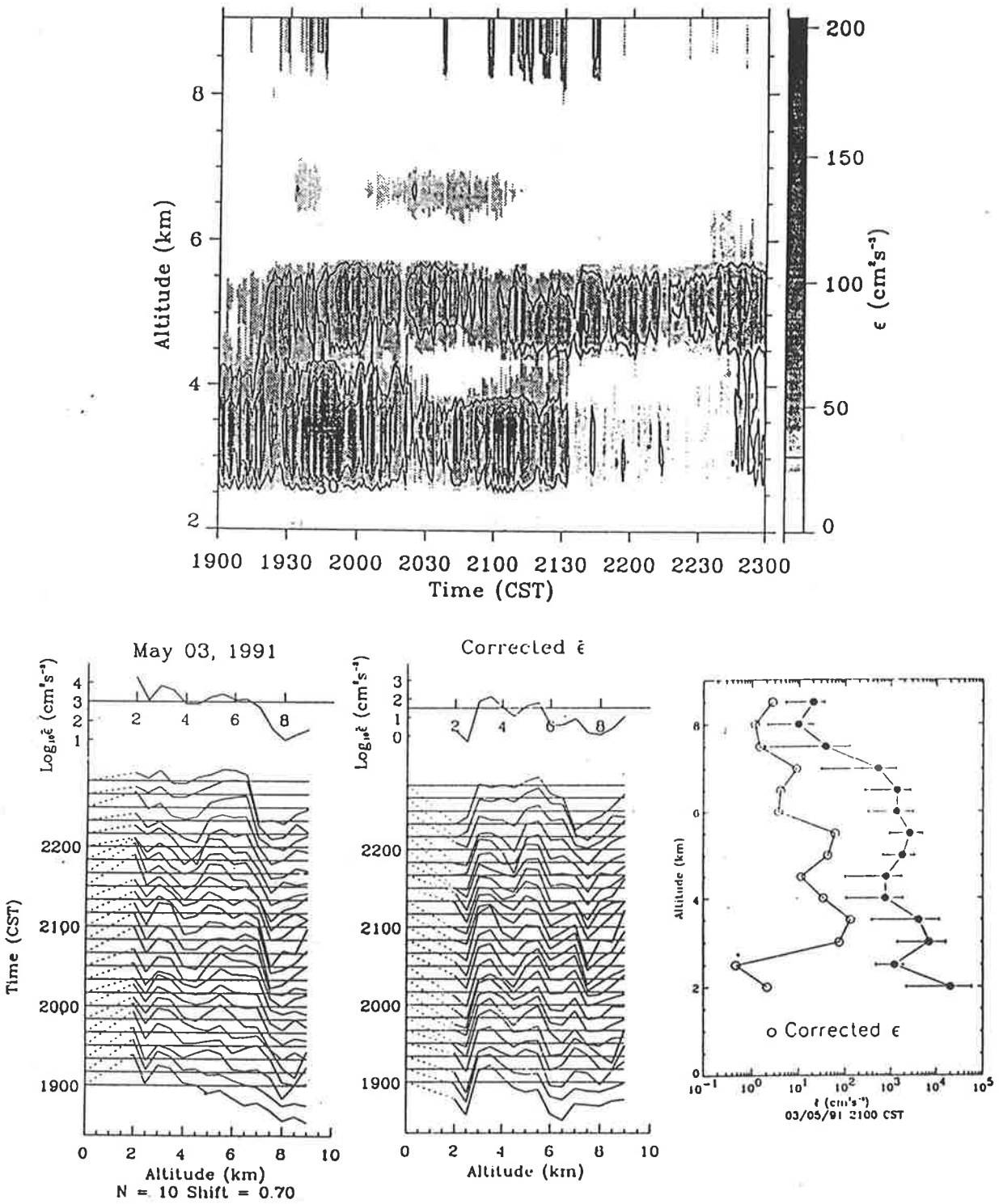

Figure 5.22: Height, time–log–height and contour plots/profiles of energy dissipation rate per unit mass for the period May 3, 2100 CST. See text at beginning of this section for more details.

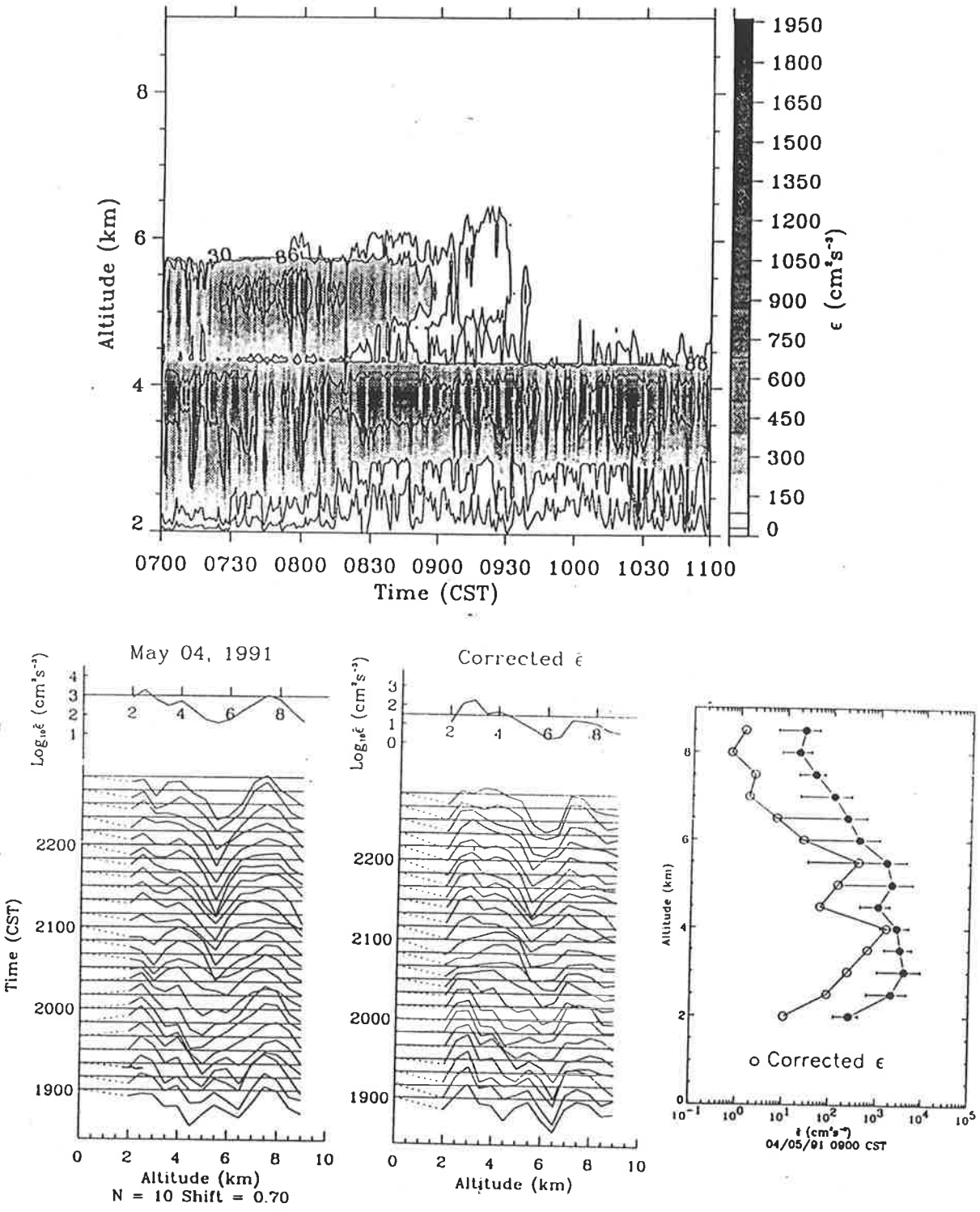

Figure 5.23: As for Figure 5.22, but for May 4, 0900 CST.

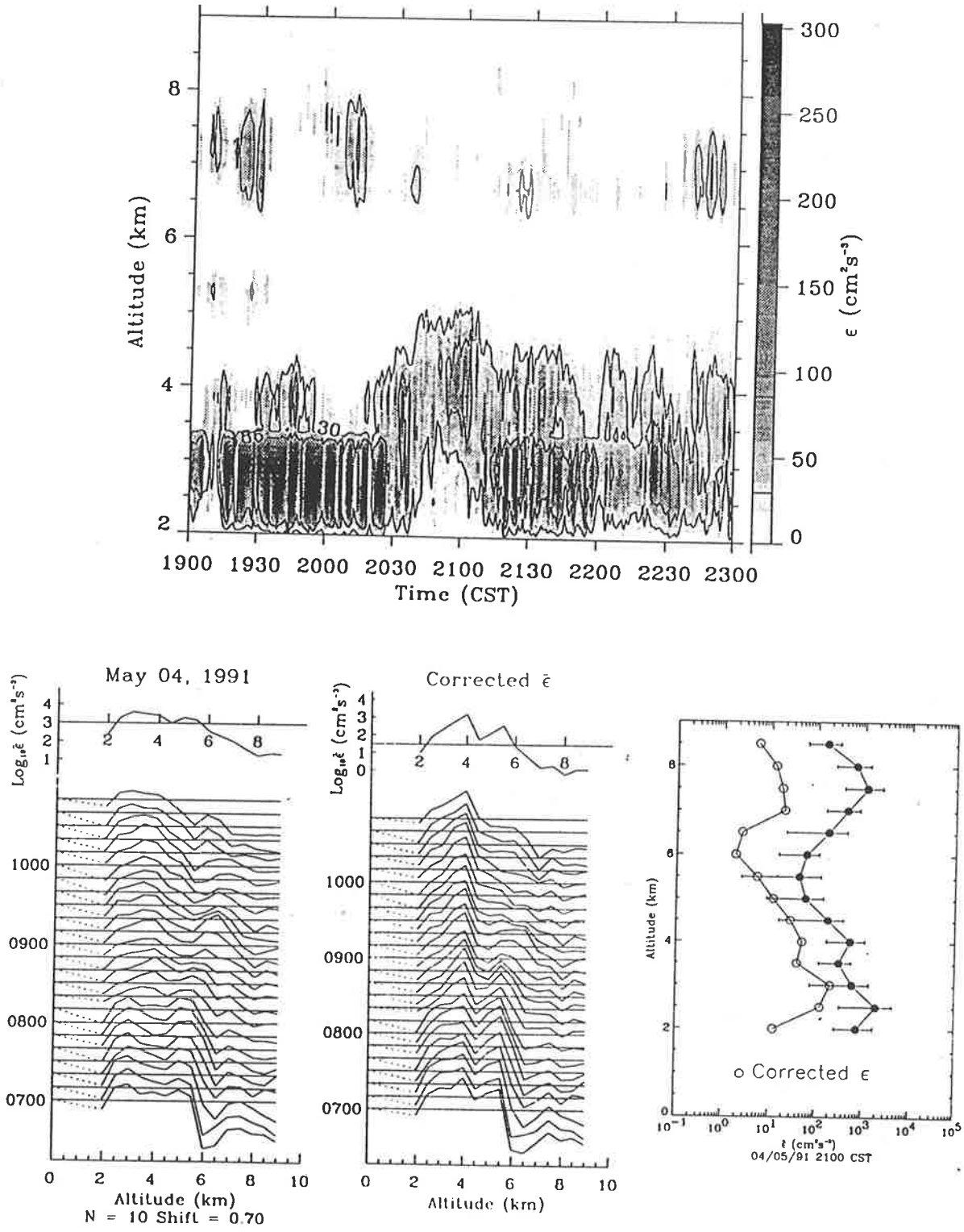

Figure 5.24: As for Figure 5.22, but for May 4, 2100 CST.

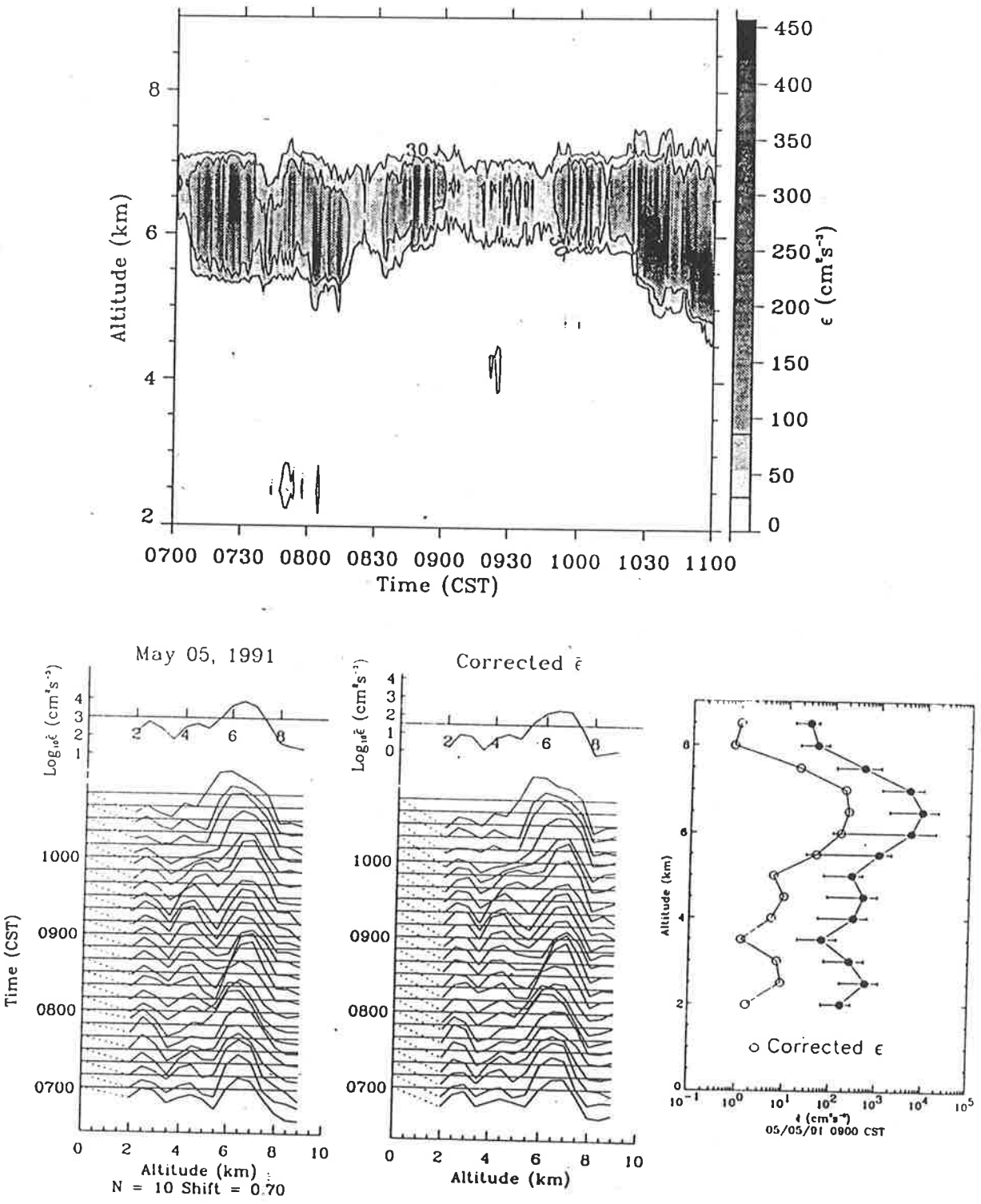

Figure 5.25: As for Figure 5.22, but for May 5, 0900 CST.

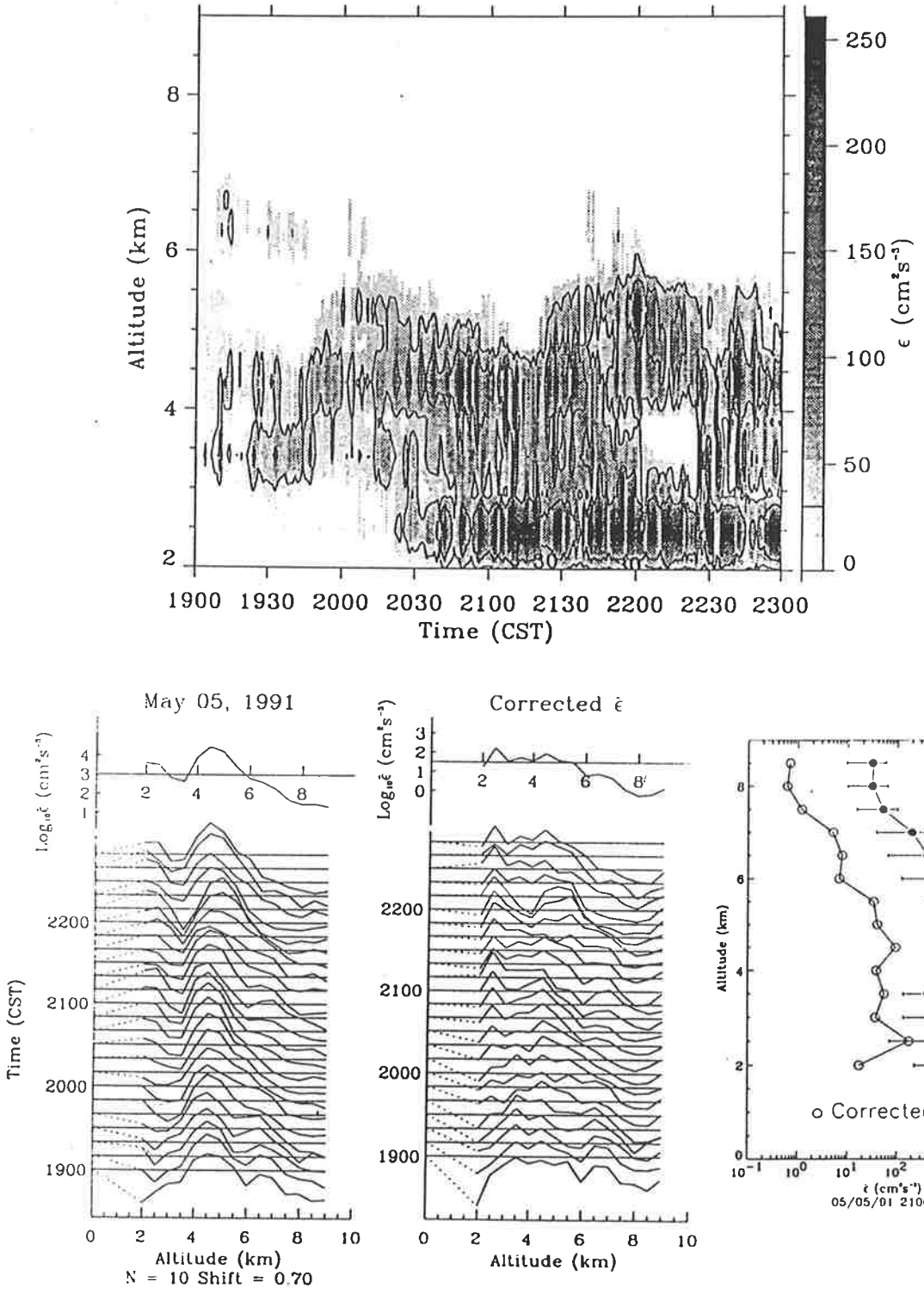

Figure 5.26: As for Figure 5.22, but for May 5, 2100 CST.

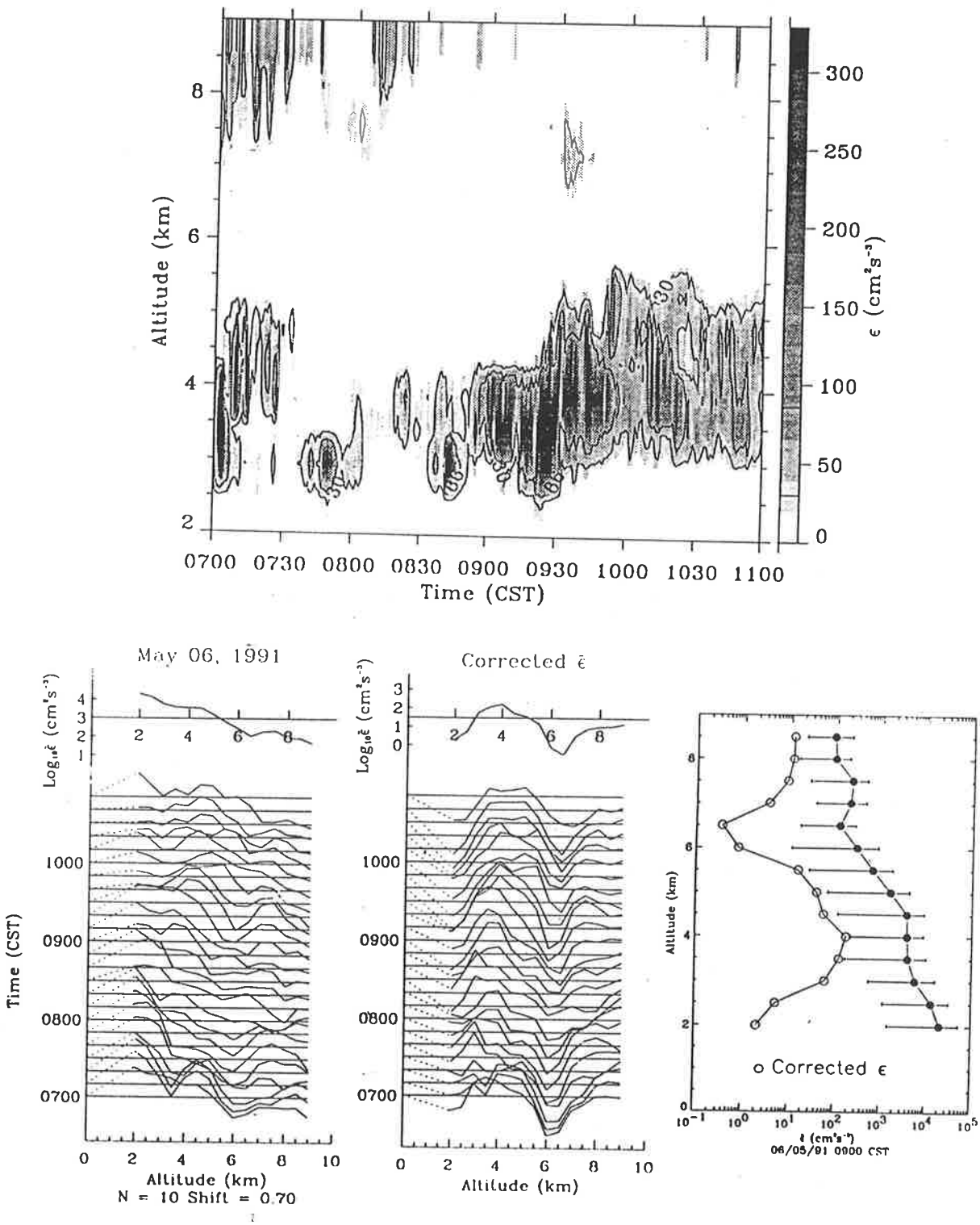

Figure 5.27: As for Figure 5.22, but for May 6, 0900 CST.

decreasing gradient with height (Figure 5.19, profile (a.)), and the wind speed/shear profiles show the relatively small wind shears present above 5.5 km height (Figure 5.3). Assuming that the humidity concentration is about the same as that at Buckland Park, then one possible cause for this moderate turbulence (plus some bursts of severe turbulence in the last half hour — see Figure 5.25) may well be wind–shear induced. This is very probable, since the wind profile for this period shows some large vertical wind shears at certain heights.

May 5, 2100 CST: the situation present at this time shows clearly a large wind shear centered at about 4 km which introduces the large humidity gradient at this height range and the enhanced echo power above 4 km (Figures 5.3 and 5.19, profile (b.)). Though the meteorological profiles may be very well correlated with one another, this cannot be said also of the strength (or concentration) of the different meteorological parameters measured, because of the large spatial separation between the radiosonde measurements and the location of the radar site; therefore, one must be careful in interpreting the humidity corrected values as the true $\bar{\epsilon}$ (see Figure 5.26).

May 6, 0900 CST: the very coarse resolution wind profile do not show any wind shear present at this height range; however, it is expected to be seen if better resolution wind data were available, since the humidity gradients tend to be very localized events. The contour plot for this case shows the very intermittent nature of atmospheric turbulence, with some occurrences of severe turbulence (Figure 5.27). Below about the 3 km range, and above about 7 km, there occurs light turbulence; and between 6 and 7 km, no turbulence is detected.

Chapter 6

Conclusions

The work presented here is one of the most extensive applications of using C_n^2 to obtain $\bar{\epsilon}$. The main points of which are:

- The radar was carefully calibrated.
- Extensive numerical analysis was performed on the radiosonde data to obtain profiles with the same resolution as the radar data.
- The model was tested for very different weather conditions.
- The flat terrain in which the radar is sited makes interpretation that much easier.

The relatively large spatial separation between the location of the radar and the airport is known to be a crucial factor in the interpretation of the results. From the author's own experience at Buckland Park, it is often the case that the weather conditions exhibited here are in stark contrast to that happening in Adelaide[1]. Another important factor is that the radiosonde measures instantaneous values, whereas the radar measures an average value over the volume occupied by the polar diagram. For these reasons, an unambiguous interpretation of the results would require more *in situ* experiments coupled with higher resolution wind profiles (which are presently unavailable).

Since the 'original' model of VANZANDT *et. al.* (1978) was proposed for the calculation of C_n^2 in the free atmosphere, there has been two subsequent models which are improvements to the original; they are VANZANDT *et. al.* (1981) and WARNOCK and

[1]This is especially so during the months of autumn, winter and spring.

VANZANDT (1985), the latter of which deals principally with improvements in the application of numerical techniques. We have only used the original model in our calculations of C_n^2, because it was thought appropriate to test and appreciate this model first. In the near future, it is expected that the improved model will be used, and the results to be compared with the present analysis.

Aside from the uncertainties in the interpretation of the results, some points of note are summarised as follows:

- very localized and/or small humidity gradients are less likely to correlate with measurements of the received echo power, where distances between the radar site and the radiosonde launch site are in the order of 35 km or so.

- poor correlation between log [Power$\times z^2$] and log [M^2] normally implies that the weather condition existing above the two sites, that is, airport and radar, are different. It can also mean that the atmosphere is very variable during the measurement run, or that the trajectory of the balloon borne radiosonde was directed away from the radar site and towards the sea.

- in most cases, the atmosphere is either free of turbulence or it has light and/or moderate turbulence. Severe turbulence are thought to be wind shear induced. All turbulence categories are very intermittent in nature, which is in general agreement with other more detailed studies of turbulence (see, for example, TENNEKES, 1973).

Presently, the Adelaide VHF radar is able to provide tropospheric measurements of clear air turbulence (CAT); it is to be expected that this will be extended to regions in the stratosphere, where humidity contributions are negligible, and thereby simplifying the analysis and for intercomparisons with other independent measurements of $\bar{\epsilon}$. In addition, it would be possible to study tropspheric/stratospheric exchange processes caused by mixing from turbulence.

Some thoughts for future work:

1. a more detailed analysis of the data would be possible if balloons were lauched at Buckland Park.

2. the effects of multiple layers of turbulence occurring in the same volume need to be studied further, with particular emphasis on applying it to measurements of the gross structures of turbulence.

3. measurements of the energy dissipation rate and the radar measured refractive index structure constant must be made directly and independently, to test the appropriateness of the turbulence equations in the atmosphere.

4. comparisons between the different methods for estimating the turbulence, with special regard to *in situ* measurements, are required.

Another important aspect of this work, which will give us a better feel for the reliability of the theoretical model of VANZANDT *et. al.* (1978), will be to study the long term variations of the energy dissipation rate (or the refractive index structure constant) in the troposphere and stratosphere with the seasons of the year. This may take a lot of patience, however, due to the nature of the work required, but it is expected to be of much value to those who need a better understanding on measurements of the gross structures of turbulence, which is still very limited.

Appendix A

Definitions and Terms

A.1 Dot Angel Echoes

The name 'dot' or 'point' was given to this type of echo, from their appearance as point targets on a Plan–Position Indicator (PPI) or Range–Height Indicator (RHI) scope photograph. Dot angels were seen consistently with radars having wavelengths of less than 3 cm, implying that these echoes have relatively small cross sections. The results of cross section measurements of insects and birds at different radar frequencies, together with observations of dot angel cross sections, by various investigators, showed that all of the dot angels observed in detail have characteristics which identify them as either insects or birds.

The ease with which radars are now able to detect birds and insects has paved the way for two new branch of the natural sciences, radar ornithology (see, for example, EASTWOOD, 1967), and radar entomology (see, for example, GLOVER *et. al.*, 1966b). In fact, insects have been observed to play a role in atmospheric studies as a source of tracers for studying atmospheric flow circulations.

A.2 Aspect Sensitivity

The tendency for stronger signals to be recorded with a vertically pointing beam rather than one at an oblique angle is termed the *aspect sensitivity*[1] of the received echoes. Several authors (GAGE and GREEN, 1978; RÖTTGER and LIU, 1978b) have shown that the highly aspect sensitive echoes tended to come from regions of static stability, because

[1] Experimental measurements at UHF do not show evidence of such physical mecahnisms (see, for example, Balsley and Peterson, 1981).

the strong signals observed tended to have long correlation times, of the order of 10 and even as long as 100 seconds duration, implying a more static process. In comparison the refractive index inhomogeneities have coherence times of less than a few seconds. Sometimes, signals from off–vertical are stronger than from the vertical. This can be explained by a tilting of the 'horizontal' layers, probably caused by gravity waves. Such tilting can be as much as 2° (see, for example, RÖTTGER and VINCENT, 1978a).

A.3 The Buoyancy length, L_B

Theoretical work on stably stratified turbulence give rise to the expression

$$(\epsilon^{2/3}/\omega_B^2)^{3/4} \tag{A.1}$$

where ϵ is the energy dissipation rate and ω_B is the Brunt Väisälä frequency, which has the dimensions of length (see, for example, LUMLEY, 1964; DOUGHERTY, 1961; WEINSTOCK, 1978). The Buoyancy length is defined as

$$L_B = 2\pi C_1 \epsilon^{1/2}/\omega_B^{3/2} \tag{A.2}$$

where $C_1 \approx 1.5$ is a numerical constant (WEINSTOCK, 1978). A physical definition of L_B is that it is the 'outer limit' of inertial subrange scales, or the transition region between the inertial and buoyancy ranges. Equation A.2 is only valid for $\omega_B^2 > 0$, that is, it only applies for shear generated turbulence in statically stable regions and not for convective turbulence. Also, L_B is quite different to L_0; this difference being in the definitions used to define these 'outer–scales' (HOCKING, 1985).

Appendix B

Coherent Integration

For a coherently scattered signal, a plot of the frequency distribution of the echoes would show the mostly high frequency noise power component and the relatively low frequency signal power component. This would imply that a low pass filtering of the coherent signals to eliminate the high frequency noise contributions is desirable. One simple method discussed here is that of coherent integration. The advantage of this process is the reduction in the number of raw data samples, without compromising the signal.

Let us assume the form of a complex raw data sample to be of the form:

$$\mathcal{C}_k = \Re_k + \jmath\Im_k \tag{B.1}$$

where $\jmath = \sqrt{-1}$, $\Re_k$ is the in-phase component and $\Im_k$ is the qudrature component of the signal. If we now consider the contributions from the following independent quantities, viz. noise (n), signal (s), DC–bias from an instrumental offset (d) and radar clutter echoes (c), then the resultant complex signal from all these contributions is given by

$$\mathcal{C}_{k,i} = \mathcal{C}^n_{k,i} + \mathcal{C}^s_{k,i} + \mathcal{C}^d_{k,i} + \mathcal{C}^c_{k,i} \tag{B.2}$$

In addition, the fact that one radar cycle yields two samples per range gate (say k and k'), a result of the transmitter phase being flipped by 180°, it would be necessary to change the sign of $\mathcal{C}_{k',i}$ when averaging, i.e.,

$$\mathcal{C}_{k,k'} = \frac{1}{N}\sum_{i=1}^{N}(\mathcal{C}_{k,i} - \mathcal{C}_{k',i}) \tag{B.3}$$

The DC–bias is simply a constant voltage contribution and so does not change its form when a transmitter phase change occurs, i.e., $\mathcal{C}^d_{k,i} = \mathcal{C}^d_{k',i}$; this is commonly called

instrumental–DC elimination. Both the signal and clutter would change their signs, that is, $C^s_{k,i} = -C^s_{k',i}$ and $C^c_{k,i} = -C^c_{k',i}$, but because noise is uncorrelated from one point to the next, a change in sign of $C^n_{k,i}$ does not alter its statistical properties. Therefore, for $k' = k$, we have that

$$C_k = \frac{2}{N}\sum_{i=1}^{N}(C^n_{k,i} + C^s_{k,i} + C^c_{k,i}) \tag{B.4}$$

The clutter contribution could either be negligible or be eliminated by means of a digital high–pass filter operation, and this is done after the coherent integration stage. In Equation B.4, the number N of added samples to be coherently integrated has to be carefully chosen. This is because the integration period, which is given by $\tau = 2NT_{ipp}$, where T_{ipp} is the interpulse period, has to be much shorter than the typical time scale of signal variations.

Appendix C

The Radiosonde Equipment

C.1 The Airborne Radiosonde

The airborne radiosonde equipment consists of a *radiosonde* and a *balloon train*. Here, we will briefly describe the radiosonde sub–system. The radiosonde used is that of an expendable type, with sensors (including internal reference sensors) to measure pressure, temperature and relative humidity profiles of the atmosphere through which it passes. A radio transmitter is used to transmit the signals of the measured parameters back to earth: a cycle of all sensor data is completed each 1.2 to 1.8 seconds. The instrumental package itself weighs only 190 gm, and there is a water activated battery to power the radiosonde.

The *barocell* used for measuring pressure is that of a single cell aneroid capsule which expands under decreasing pressure. The sensors used for temperature and humidity measurements are referred to as the *thermocap* and *humicap*, respectively. During flight the sensors are exposed away from the body of the radiosonde by the sensor arm, thereby (a) reducing the effects of radiation and (b) ensuring a smooth uninterrupted air flow over the sensors. The manufacturer's specifications for the sensors[1] are given in Table C.1.

C.2 The Receiver

Table C.2 lists all the relevant details which were specified for the radiosonde receiver's serial output. This information was used for the construction of a program (for use with a lap–top computer) to directly sample the digitised data from the receiver, storing

[1] A complete radiation correction routine is used to cover all solar elevations from the surface to 3 hPa.

	Temperature sensor	*Humidity sensor*	*Barocell*
Sensor type	Thermocap Capacitive bead	HUMICAP thin film capacitor	Capacitive aneroid
Measuring range	+60°C to −90°C	0% RH to 100% RH	1060 hPa to 3 hPa
Accuracy	± 0.2°C	± 2% RH	± 0.5 hPa
Resolution	0.1°C	1% RH	0.1 hPa

Table C.1: The sensor specifications as claimed by the manufacturer.

Serial Output	
Purpose	Output of meteorological values as an ASCII string
Standard RS-232C Serial Interface	
Data Bits	8
Parity	no
8th Data Bit	1
Stop Bits	1
Baud Rate	Programmable (110, 300, 1200, 4800 or 9600)
Output Format	t, LP, T, U, P, (CR)(CR)(LF) t = flight time in seconds LP = logarithmic pressure (≡ 4096 * ln(P/10)) T = temperature in 0.1 °C U = relative humidity in 1% RH P = pressure in 0.1 hPa
Number field	Integer (range: -32768, 32767) Exactly 6 ASCII characters (-)nnnnn (leading nulls if necessary)

Table C.2: Information for the radiosonde receiver's serial output.

them in file(s) for subsequent analysis later on. With this data, we would have total control of the format for the results from our analysis, rather than the awkward output of derived parameters calculated at standard and significant levels as used by the Bureau of Meteorology.

All equations were referenced from the handbook: *Radiosonde computation equations and procedures for the Philips carbon hygristor radiosonde.*

Appendix D

The Adelaide VHF Radar

The University of Adelaide operates one MF/HF radar (working at frequencies of 2 and 6 MHz) and one VHF radar (at a central frequency of 54.1 MHz) at Buckland Park, South Australia (34°S, 138°E). Its location with respect to the capital of South Australia (Adelaide) is that it is approximately 40 kilometres north of the city. Orographically, the site occupied by the two radars are quite flat and featureless (the site is level to 0.1°), with an existing water–table a few metres below the surface. The surrounding areas are mainly inhabited by small farming communities. The flat terrain limits ground–clutter and contamination of the wind field due to lee–waves.

A diagramatical representation of the Adelaide VHF radar installation is shown in Figure D.1. The main array is of the coaxial–colinear (Co–Co) type, and may be used for both transmission and reception, where a fast and highly insulating transmit–receive duplexer was used to switch the antenna from the transmitter to the receiver and vice versa. The three smaller arrays are composed of Yagi antennas and are used for reception only.

The Co–Co array is sixteen wavelengths square and is raised $\lambda/4$ above a copper wire ground–plane (also called reflector wires). Its theoretical half–power half–width is 1.6° with the first sidelobe centered at an angle of 6.5° and an amplitude which is - 12 dB relative to the main beam. By introducing suitable phase delays in the cables feeding the parallel rows (altogether 32 rows), it may be steered in the East–West plane. Because of the phase relation along a string (or row) is fixed, a beam steering parallel to the Co–Co string is not possible.

At the time of use, the receiving system was operated with a low power valve trans-

mitter which had a mean power of 200 W. This limit the height of observations to the troposphere. A more complete description of the Adelaide VHF radar system can be found elsewhere (e.g., VINCENT *et. al.*, 1987).

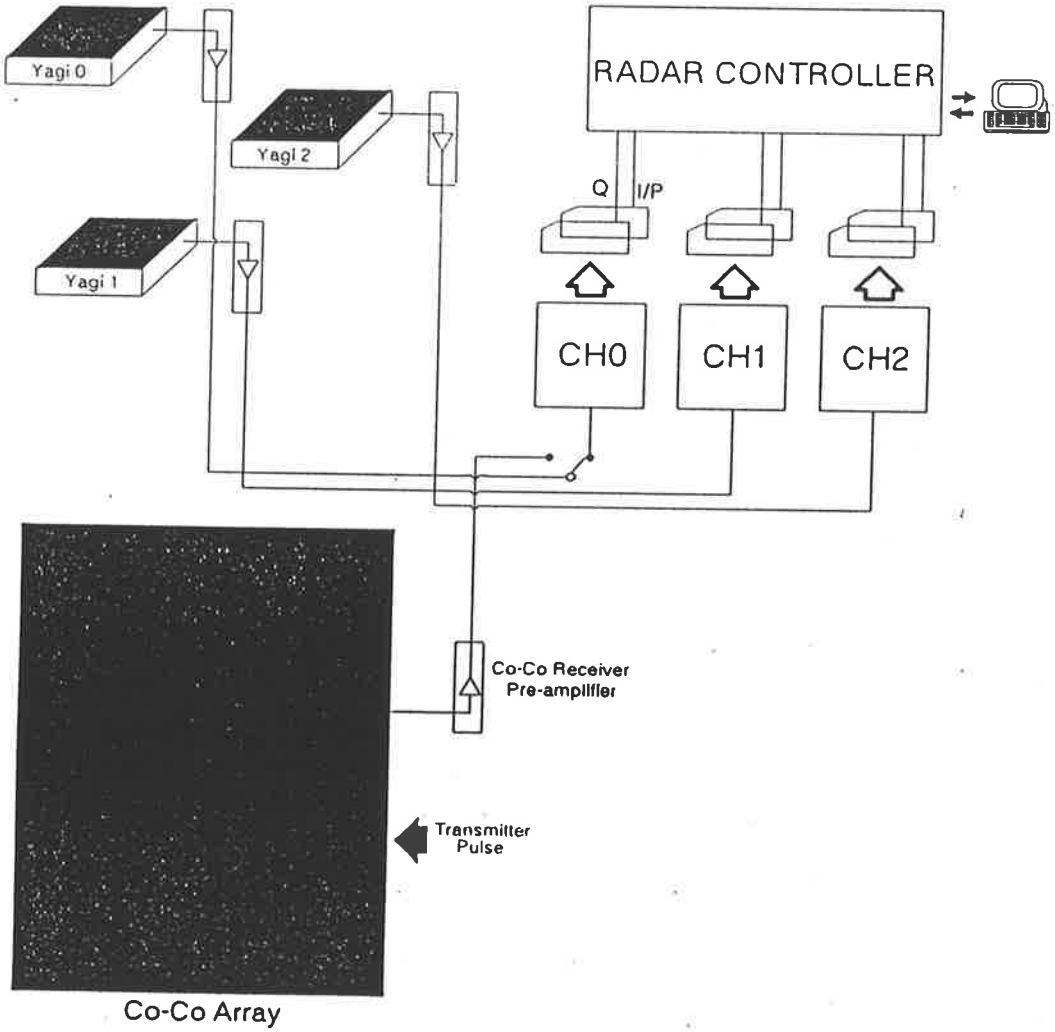

Figure D.1: A diagram of the Adelaide VHF radar installation.

Appendix E

Determining the Transmitter Efficiency, ϵ

The aim is to determine the efficiency of the transmitting antenna, that is, the Co–Co array at Buckland Park, given that maximum efficiency is obtained when all the components are identical and correctly spaced. We also make the assumption that (a) a single Yagi–element is a 100% efficient radiator and (b) noise from the noise–generator set at 0°K and 'unaccountable' noise is approximately the same as when antenna is present and skynoise is 0°K.

By using the radar (Co–Co or yagi) as a radio telescope to collect skynoise $\overline{U_s^2}$ and then to convert this to skynoise temperature (T_s) using the radar calibration values, it is possible (using a Co–Co array, a Yagi array and a Yagi element) to determine the efficiency of the Co–Co array. In the calibration stage, random noise signal of temperature T from a noise–generator was fed into the preamplifier stage (refer to Figure 3.1) and the output signal $\overline{U^2}$ was measured. For increasing T, the ideal case is that of a linear relationship between T and $\overline{U^2}$, in which case it's simply a matter of determining the gradient $m = \overline{U^2}/T$.

Then for a given antenna (array or element) the *absolute* skynoise temperature is given by

$$T_s = \overline{U_s^2}/m - T_{zoff} \qquad \text{(E.1)}$$

where T_{zoff} (the *zero–offset temperature*) is the equivalent temperature of the signal–generator when it is turned off (reference is made here to assumption (b) above). Once all three antennae are used in this way, the next step is to scatter plot the skynoise

temperatures from two different antennae combination, and hence determine their relative efficiency from the slope of the graph.

Finally, if the Yagi array is α% efficient with respect to the Yagi element and the Co–Co array is β% efficient with respect to the Yagi array then, assuming that the Yagi element is 100% efficient as a radiator (and hence 100% efficient as a receiver), we have the Co–Co efficiency ϵ given by the product of α and β, that is

$$\epsilon = \alpha\beta \tag{E.2}$$

Appendix F

Richardson's Criterion for Stability

The assumption for the onset of turbulence, *i.e.*, $Ri = 0.25$, needs to be clarified further. One form of the gradient Richardson number equation which is often used for discussion on the stability of the atmosphere is the following (HINES, 1971):

$$Ri \equiv \frac{\omega_B^2}{(\partial \bar{u}/\partial z)^2} \tag{F.1}$$

where $\bar{u}$ is the horizontal background wind velocity upon which turbulent motions might come to be superimposed, z is the vertical (height) coordinate and ${\omega_B}^2$ is the square of the Brunt Väisälä frequency.

In reference to Equation D.1, the fact that $Ri \leq 1/4$ must be satisfied in order that turbulence may be developed in a horizontally stratified atmosphere, seems to be justified. This is because the Brunt Väisälä frequency is a measure of stability in the atmosphere, while the gradient of the wind speed in the denominator of Equation F.1 is a measure of the wind shear, which causes turbulence in an initially stratified atmosphere (such as the breaking of Kelvin–Helmholtz waves). Therefore, a larger wind shear contribution with a less stable atmosphere would produce the condition for instability as stated by the Richardson criterion. Different authors researching on this subject (for example, MILES, 1961; HOWARD, 1961; MENKES, 1961; CHIMONAS, 1970) have come to the conclusion that Equation F.1 is a necessary condition for the onset of turbulence in a previously laminar flow, though *it is by no means guaranteed as a sufficient condition.*

Richardson's criterion for the onset of turbulence is completely satisfied only when dealing with a (fluid) medium for which the following assumptions are satisfied:

- the medium exhibits horizontal stratification

- the 'background' parameters of the fluid have been taken to vary in the vertical direction only

- the 'background' fluid velocity $\bar{u}$ is horizontally directed

In the real atmosphere, these assumptions are satisfied only approximately at best, and many situations arise in which they are violated completely. It seems unlikely, in consequence, that Equation F.1 can be maintained as a necessary condition for instability in practice.

Appendix G

Pseudocode for NDW Filter

Using interpolated balloon data with a time resolution of 10 seconds does not imply an equally fixed height resolution[1] Δz. A typical range is from approximately 20 metres to 50 metres. For this reason, it would be necessary to calculate Δz for each of the heights analysed.

The array containing the initial data points is stored in A and array H contains the corresponding height values. The size of both arrays equals N:

1. Calculate approximate Δz
2. Set width *hres* for smoothing (e.g., 0.5 km, 1 km, 1.5 km, etc.)
3. $res = \text{Int}(hres/(2\Delta z))$
4. For $res - i \leq i < N - res$ do

   Set $B = A[range]$, where $range = i - res, i + res$ (i.e., consider only points within *range*)

   Reject 5% of lowest and heighest values of B[2]

   Perform NDW filtering
5. Return filtered array F corresponding to original array A

where *Int* is the integer function, that is, it returns the expression converted to integer type. The algorithm for NDW filtering is given below:

[1]This would depend on the condition of the atmosphere and the solar elevation angle.

[2]The rejected data are replaced with some arbitrary value to distinguish them from valid data, this is so that the size of array B is not decreased from its previously set width.

- Set $C = H[range]$
- Normalize array C from -1.5 to $+1.5$ such that the mid point of the array would contain zero. The value $\pm$ 1.5 is the cut–off point for the Gaussian function, which is approximately $\pm$ 3.8 σ, where $\sigma = 1.08444/e$, and the numerical value 1.08444 is used to normalise $f(j)$ to unity at its central maxima.
- Calculate $S_j = \sum_j^n f(j)B(j)w(j)$

where n is the size of the array C, and $f(j)$ and $w(j)$ are given by the following equations:

$$f(j) = \frac{1}{\sqrt{2\pi}\sigma} \exp(-j^2/2\sigma^2)$$

$$W(j) = \begin{cases} H_{j+1} - H_j, & j = 0 \\ H_j - H_{j-1}, & j = n \\ \frac{H_{j+1} - H_{j-1}}{2.0}, & \text{otherwise} \end{cases}$$

where σ is defined above. It is to be noted that the area under the function $f(j)$ is almost unity when integrated from $j = -1.5$ to $j = 1.5$.

Appendix H

Power Splitter Circuit

A power splitter was required to duplicate the original signal received by the radar (but at half the original power) in order that one channel may be attenuated more highly than the other, so that stronger signals can be attenuated down to a level which is within the linear–range of the receiver pre–amplifier gain, and that low level signals can be obtained from the remaining channel[1]. The power splitter is simply a circuit consisting of an inductor and two output terminals, but capacitor(s) may be required to tune the circuit to give the desired phase (Figure H.1). For use with the Buckland Park VHF radar, the requirement is for 50 Ω yerminators and zero phase. Then using a Smith Chart it is possible to calculate the inductance required to satisfy these conditions.

The inductor was simply made using a certain length of wire (of specified diameter), and wound around a cylindrical object to make a coil. The inductor can then be tuned, once in the circuit, by compression or expansion of the coil. The Inductance of air–core

[1]This channel normally has no ***additional*** attenuation, i.e., apart from the initial attenuation of half the original power.

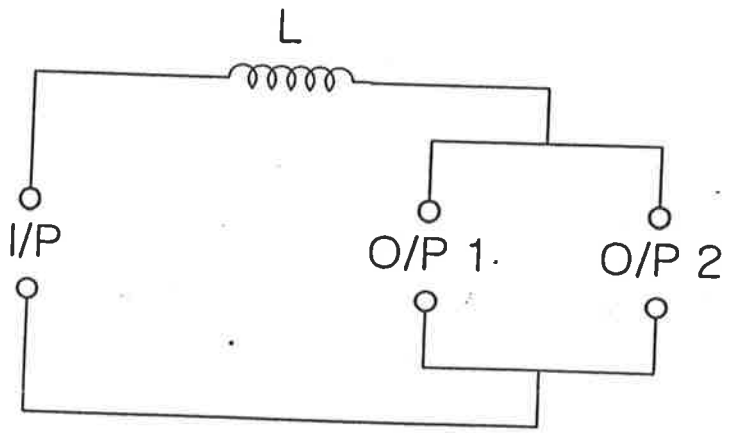

Figure H.1: Circuit diagram for a power splitter.

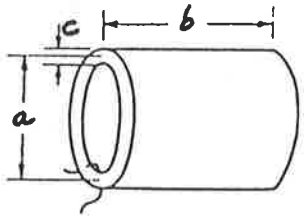

Figure H.2: Coil dimensions used in the inductance formula.

coils was calculated from the following equation (*The radio amateur's handbook*, 1958):

$$L = \frac{0.2a^2n^2}{3a + 9b + 10c} \tag{H.1}$$

where L is the inductance in microhenrys, a the average diameter of coil in inches, b the length of winding in inches, c the radial depth of winding in inches and n the number of turns (see Figure H.2.). The quantity $10c$ in Equation H.1 may be neglected if the coil only has one layer of wire.

Bibliography

[1] Allen C. H. and S. D. Weiner. *Study directed toward optimization of operating parameters of the electromagnetic–acoustic probe for the remote measurement of atmospheric parameters.* Report AF–19(628)–2774, Air Force Cambridge Res. Lab., Cambridge, Mass., 1963.

[2] Andreas E. L. The refractive index structure parameter, C_n^2, for a year over the frozen Beaufort Sea. *Radio Sci.*, 24:667–679, 1989.

[3] Atlas D. *Advanced in Geophysics.* Academic, New York, N.Y., 1964.

[4] Atlas D., K. R. Hardy, and T. G. Konrad. Radar detection of the tropopause and clear air turbulence. In *Proceedings of the 12th Weather Radar Conference*, pages 279–284, Boston, Mass., 1966.

[5] Balsley B. B. and V. L. Peterson. Doppler–Radar measurements of clear air atmospheric turbulence at 1290 MHz. *J. Appl. Meteorol.*, 20:4266–4274, 1981.

[6] Barat J. Some characteristics of clear air turbulence in the middle stratosphere. *J. Atmos. Sci.*, 39:2553–2564, 1982.

[7] Barat J. and F. Bertin. Simultaneous measurements of temperature and velocity fluctuations within clear air turbulent layers: analysis of the estimate of dissipation rate by remote sensing techniques. *J. Atmos. Sci.*, 41:1613–1619, 1984.

[8] Batchelor G. K. *The theory of homogeneous turbulence.* Cambridge University Press, 1953.

[9] Battan L. J. *Radar observations of the atmosphere.* The University of Chicago Press, Chicago, Ill., 1973.

[10] Bean B. R. and E. J. Dutton. *Radio Meteorology.* Dover, New York, 1968.

[11] Booker H. G. and W. E. Gordon. Theory of radar scattering in the troposphere. *Proc. IEEE*, 38:401–412, 1950.

[12] Browning K. A. Meteorological aspects of radar. *Rep. Prog. Phys.*, 41:761–806, 1978.

[13] Bretherton F. P. Waves and turbulence in stably stratified fluids. *Radio Sci.*, 4:1279–1287, 1969.

[14] Chadwick R. B. and K. P. Moran. Long–term measurements of C_n^2 in the boundary layer. *Radio Sci.*, 15:355–361, 1980.

[15] Chu Y. H., J. K. Chao, C. H. Liu, and J. Röttger. Aspect sentivity at tropospheric heights measured with vertically pointed beam of the Chung–Li VHF radar. *Radio Sci.*, 25:539–550, 1990.

[16] Chimonas G. The extension of the Miles–Howard theorem to compressible fluids. *J. Fluid Mech.*, 43:833–836, 1970.

[17] Crane R. K. Measurements of clear air turbulence in the lower stratosphere using the Millstone Hill L–band radar. In *14th Radar Meteorological Conference*, pages 101–106, Boston, Mass., 1970. Preprints.

[18] Crane R. K. *Stratospheric turbulence analysis.* Report AFGL–TR–77–0207 (ADO 47740), Air Force Geophys. Lab., Hanscom Air Force Base, Mass., 1977.

[19] Debye P. *Polar Molecules.* Dover Publ. Co., New York, N.Y., 1957.

[20] Dougherty J. P. The anisotropy of turbulence at the meteor level. *J. Atmos. Terr. Phys.*, 21:210–213, 1961.

[21] Doviak R. J. and D. S. Zrnic. Reflection and scatter formula for anisotropically turbulent air. *Radio Sci.*, 19:325–336, 1984.

[22] Doviak R. J. and D. S. Zrnic. *Doppler Radar and Weather Observations.* Academic, Orlando, Fla., 1984.

[23] Du Castel F. P., A. Spizzichino, and J. Voge. On the role of the process of reflection in radio wave propagation. *J. Res. Natl. Bur. Stnds.*, 66D:273–284, 1962.

[24] Du Castel F. P. *Tropospheric radio wave propagation beyond the horizon.* Pergamon, New York, 1966.

[25] Eagleman J. R. *Meteorology: the atmosphere in action.* Wadsworth Publishing Co., Belmont, California, 1985.

[26] Eastwood E. *Radar Ornithology.* London, Methuen, 1967.

[27] Eaton F. D., W. A. Peterson, J. R. Hines, K. R. Peterman, R. E. Good amd R. R. Beland, and J H Brown. Comparisons of VHF radar, optical, and temperature fluctuation measurements of C_n^2, r_0 and θ_0. *Theor. Appl. Climatol.*, 39:17–29, 1988.

[28] Epstein P. A. Reflection of waves in an inhomogeneous absorbing medium. *Proc. Natl. Acad. Sci.*, 16:627–636, 1930.

[29] Farley D. T. Comments on Fresnel scatter. In *MAP Handb. 9*, pages 71–72, Univ. of Ill., Urbana, 1983.

[30] Friend A. W. Developments in meteorological soundings by radio waves. *J. Aeronaut. Sci.*, 7:347–352, 1940.

[31] Frish A. S. and S. F. Clifford. A study of convection capped by a stable layer using doppler radar and acoustic echo sounders. *J. Atmos. Sci.*, 31:1622–1628, 1974.

[32] Gage K. S. and J. L. Green. Evidence for specular reflection from monostatic VHF radar observations of the stratosphere. *Radio Sci.*, 13:991–1001, 1978.

[33] Gage K. S. and B. B. Balsley. On the scattering and reflection mechanisms contributing to clear air radar echoes from the troposphere, stratosphere, and mesosphere. *Radio Sci.*, 15:243–257, 1980.

[34] Gage K. S., J. L. Green, and T. E. VanZandt. Use of doppler radar for the measurement of atmospheric turbulent parameters from the intensity of clear air echoes. *Radio Sci.*, 15:407–416, 1980.

[35] Gage K. S., W. L. Ecklund, and B. B. Balsley. A modified Fresnel scattering model for the parameterization of Fresnel returns. *Radio Sci.*, 20:1493–1501, 1985.

[36] Glover K. M. and K. R. Hardy. Dot angels: insects and birds. In *Proc. 12th Weather Radar Conf.*, pages 264–468, 1966.

[37] Glover K. M., K. R. Hardy, T. G. Konrad, W. N. Sullivan, and A. S. Michaels. Radar observations of insects in free flight. *Science*, 154:967–972, 1966.

[38] Gossard E. E. and J. H. Richter. The shape of internal waves of finite amplitude from high resolution radar sounding of the lower atmosphere. *J. Atmos. Sci.*, 27:971–973, 1970.

[39] Gossard E. E., D. R. Jensen, and J. H. Richter. Analytical study of tropospheric structure as seen by high–resolution radar. *J. Atmos. Sci.*, 28:794–807, 1971.

[40] Gossard E. E., R. B. Chadwick, K. P. Moran, R. G. Strauch, G. E. Morrison, and W. C. Campbell. Observations of winds in the clear air using FM–CW radar. *Radio Sci.*, 13:285–289, 1978.

[41] Gossard E. E., W. D. Neff, R. J. Zamora, and J. E. Gaynor. The fine structure of elevated refractive layers: implications for over–the–horizon propagation and radar sounding systems. *Radio Sci.*, 19:1523–1533, 1984.

[42] Hardy K. R. and I. Katz. Probing the clear atmosphere with high power, high resolution radars. *Proc. IEEE*, 57:468–480, 1969.

[43] Hinze J. O. *Turbulence, an introduction to its mechanism and theory.* McGraw–Hill Co., New York, N.Y., 1959.

[44] Hinze J. O. *Turbulence.* McGraw–Hill Co., New York, N.Y., 1975.

[45] Hicks J. J. and J. K. Angell. Radar observations of breaking gravitational waves in the visually clear atmosphere. *J. Appl. Meteorol.*, 7:114–121, 1968.

[46] Hildebrand P. H. A radar study of shear enhanced turbulent diffusion. In *Proceedings of the 17th Conference on Radar Meteorology*, pages 330–337, Boston, Mass., 1976.

[47] Hines C. O. Generalisations of the Richardson criterion for the onset of atmospheric turbulence. *Quart. J. R. Met. Soc.*, 97:429–439, 1971.

[48] Hocking W. K. and R. A. Vincent. Comparative observations of D region HF partial reflections at 2 and 6 MHz. *J. Geophys. Res.*, 87:7615–7624, 1982.

[49] Hocking W. K. and J. Röttger. Pulse–length dependence of radar signal strengths for Fresnel backscatter. *Radio Sci.*, 18:1312–1324, 1983.

[50] Hocking W. K. *Absolute calibration of the SOUSY VHF stationary radar.* Internal Report MPAE–W–00–83–14, Max–Planck–Institut Für Aeronomie, Katlenburg–Lindau, 1983.

[51] Hocking W. K. On the extraction of atmospheric turbulence parameters from radar backscatter Doppler Spectra I, Theory. *J. Atmos. Terr. Phys.*, 45:89–102, 1983.

[52] Hocking W. K. Measurement of turbulent energy dissipation rates in the middle atmosphere by radar techniques: a review. *Radio Sci.*, 20:1403–1422, 1985.

[53] Howard L. N. Note on a paper of J. W. Miles. *J. Fluid Mech.*, 10:509–512, 1961.

[54] Holton J. R. *An introduction to dynamic meteorology.* Academic Press, New York, N.Y., 1972.

[55] Houghton J. T. *The physics of atmospheres.* Cambridge University Press, Cambridge [Cambridgeshire] New York, 1986.

[56] James P. K. A review of radar observations of the troposphere in clear air conditions. *Radio Sci.*, 15:151–175, 1980.

[57] Kenneth R. H. and I. Katz. Probing the clear atmosphere with high power, high resolution radars. *Proc. IEEE*, 57:468–480, 1969.

[58] Kolmogorov A. N. *Turbulence, Classic papers on Statistical theory.* Interscience Publishers, Inc., New York, N.Y., 1961. Edited by Friedlander S. K. and L. Topper, 2nd edition.

[59] Kropfli R. A. Simultaneous radar and instrumented aircraft observations in a CAT layer. *J. Appl. Meteor.*, 10:796–802, 1971.

[60] Lilly D. K., D. E. Waco, and S. I. Adelfang. Stratospheric mixing from high–altitude turbulence measurements. *J. Appl. Meteor.*, 13:488–493, 1974.

[61] Lane J. A. and R. W. Meadows. Simultaneous radar and refractometer soundings of the troposphere. *Nature*, 197:35–36, 1963.

[62] Liu C. H. Interpretation of MST radar returns from clear air. In *MAP Handb. 9*, pages 49–56, Univ. of Ill., Urbana, 1983.

[63] Long R. L. Some properties of horizontally homogeneous, statistically steady turbulence in a stratified fluid. *Boundary–Layer Meteorology*, 5:139–157, 1973.

[64] Lumley J. L. The spectrum of nearly inertial range turbulence in a stably stratified fluid. *J. Atmos. Sci.*, 21:99–102, 1964.

[65] Lumley J. L. and H. A. Panofsky. *The structure of atmospheric turbulence.* New York, Wiley, 1964.

[66] Menkes J. On the stability of a heterogeneous shear layer subject to a body force. *J. Fluid Mech.*, 11:284–290, 1961.

[67] Metcalf J. I. and D. Atlas. Microscale ordered motions and atmospheric structure associated with thin echo layers in stable stratified zones. *Boundary Layer Meteorol.*, 4:7–35, 1973.

[68] Miles J. W. On the stability of heterogeneous shear flows. *Ibid.*, 10:496–508, 1961.

[69] Nastrom G. D., K. S. Gage, and W. L. Ecklund. Variability of turbulence, 4–20 km, in Colorado and Alaska from MST radar observations. *J. Geophys. Res. (Atmos.)*, 91:6722–6734, 1986.

[70] Neudegg D. Honour's thesis, The University of Adelaide, 1987.

[71] Obukhov A. M. Structure of the temperature field in a turbulent flow. *Izv. Akad. Nauk SSSR, Ser. Geograf. Geofiz.*, 13:58ff, 1949.

[72] Ottersten H. Atmospheric structure and radar backscattering in clear air. *Radio Sci.*, 4:1179–1193, 1969.

[73] Ottersten H. Mean vertical gradient of potential refractive index in turbulent mixing and radar detection of CAT. *Radio Sci.*, 4:1247–1249, 1969.

[74] Ottersten H. K., R. Hardy, and C. G. Little. Radar and sodar probing of waves and turbulence in statically stable clear–air layers. *Boundary–Layer Meteorology*, 4:47–89, 1973.

[75] Röttger J. and R. A. Vincent. VHF radar studies of tropospheric velocities and irregularities using spaced antenna techniques. *Geophys. Res. Lett.*, 5:917–920, 1978.

[76] Röttger J. and C. H. Liu. Partial reflection and scattering of VHF radar signals from the clear atmosphere. *Geophys. Res. Lett.*, 5:357–360, 1978.

[77] Röttger J. Reflection and scattering of VHF radar signals from atmospheric reflectivity structures. *Radio Sci.*, 15:259–276, 1980.

[78] Sato T. and R. F. Woodman. Fine altitude resolution observations of stratospheric turbulent layers by the Arecibo 430 MHz radar. *J. Atmos. Sci.*, 39:2546–2552, 1982.

[79] Saxton J. A., J. A. Lane, R. W. Meadows, and P. A. Matthews. Layer structure of the troposphere — Simultaneous radar and microwave refractometer investigations. *Proc. IEE*, 111:275–283, 1964.

[80] Schmidt G., R. Rüdiger, and P. Czechowsky. Complementary code and digital filtering for detection of weak VHF radar signals from the mesosphere. *IEEE Trans. Geo. Elec.*, 17:154–161, 1979.

[81] Tatarski V. I. *Wave propagation in a turbulent medium.* New York, McGraw–Hill, 1961.

[82] Tatarski V. I. *The effects of the turbulent atmosphere on wave propagation.* Technical Report TT–68–50464, Nat. Tech. Infor. Service, U.S. Dept. of Commerce, Springfield, Va., 1971.

[83] Tennekes H. Intermittency of the small–scale structure of atmospheric turbulence. *Boundary Layer Meteorol.*, 4:241–250, 1973.

[84] Tennekes H. and J. Lumley. *A first course in turbulence.* MIT Press, Cambridge, Mass., 1961.

[85] Trout D. and H. A. Panofsky. Energy dissipation near the tropopause. *Tellus*, 21:355–358, 1969.

[86] Tsuda T., T. Sato, K. Hirose, S. Fukao, and S. Kato. MU radar observations of the aspect sensitivity of backscattered VHF echo power in the troposphere and lower stratosphere. *Radio Sci.*, 21:971–980, 1986.

[87] VanZandt T. E., J. L. Green, K. S. Gage, and W. L. Clark. Vertical profiles of refractivity turbulence structure constant: comparison of observations by the Sunset radar with a new theoretical model. *Radio Sci.*, 13:819–829, 1978.

[88] Vernin J., M. Crochet, M. Azouit, and O. Ghebrebrhan. SCIDAR/radar simultaneous measurements of atmospheric turbulence. *Radio Sci.*, 25:953–959, 1990.

[89] Vincent R. A., P. T. May, W. K. Hocking, W. G. Elford, B. H. Candy, and B. H. Briggs. First results with the Adelaide VHF radar: spaced antenna studies of tropospheric winds. *J. Atmos. Terr. Phys.*, 49:353–366, 1987.

[90] Wait J. R. *Electromagnetic waves in stratified media.* Pergamon, New York, N.Y., 1962.

[91] Warnock J. M., N. Sengupta, and R. G. Strauch. Comparison between height profiles of C_n^2 measured by the Stapleton UHF clear–air doppler radar and model calculations. In *Eigth Symposium on Turbulence and Diffusion*, Boston, Mass., 1988. Preprint volume.

[92] Weinstock J. On the theory of turbulence in the buoyancy subrange of stably stratified flows. *J. Atmos. Sci.*, 35:634–649, 1978.

[93] Weinstock J. Using radar to estimate dissipation rates in thin layers of turbulence. *Radio Sci.*, 16:1401–1406, 1981.

[94] Woodman R. F. and A. Guillan. Radar observations of winds and turbulence in the stratosphere and mesosphere. *J. Atmos. Sci.*, 31:493–505, 1974.

[95] Yeh K. C. and C. H. Liu. *Theory of ionospheric waves.* Academic, New York, 1972.

[96] *The radio amateur's handbook.* The American Radio Relay League, West Hartford, Conn., USA, 35th edition, 1958. The Rumford Press — Concord, New Hampshire, Conn., USA.

[97] *Draft PC–CORA radiosonde handbook.* Bureau of Publications, May 1991. Version 1.1.

[98] Birnbaum G. and Chatterjee S. K. The dielectric constant of water vapour in the microwave region. *J. App. Phys.*, 32:220-223, 1952.

[99] VanZandt T. E., Gage K. S. and Warnock J. M. An improved model for the calculations of profiles of Cn^2 and ε in the free atmosphere from background profiles of wind, temperature and humidity. Preprint volume, *20th Conference of Radar Meteorology*, Nov. 30--Dec. 3, Boston, MA, 129-135, 1981.

[100] Warnock J. M. and VanZandt T. E. A statistical model to estimate the refractivity turbulence structure constant Cn^2 in the free atmosphere. NOAA TM ERL AL-10, NOAA Environmental Res. Labs., Boulder Co, 175pp 1985.